Exploiting a Multichannel Receiver Array in ISAR Imaging

Concerning Clutter Suppression for Maritime Targets in an Airborne Setup

N.J. de Jong

Technische Universiteit Delft

TU Delft

Exploiting a Multichannel Receiver Array in ISAR Imaging

Concerning Clutter Suppression for Maritime Targets in an Airborne Setup

by

N.J. de Jong

to obtain the degree of Master of Science
at the Delft University of Technology,
to be defended publicly on Friday May 15, 2020 at 10:00 AM.

Student number:	4280121	
Project duration:	September 16, 2019 – May 15, 2020	
Thesis committee:	Prof. Dr. A. Yarovoy,	TU Delft
	Dr. F. Uysal,	TU Delft, supervisor
	Dr. ir. P. Lopez-Dekker,	TU Delft
	Dr. ir. J.J.M. de Wit	TNO

TU Delft

Preface

As I am a huge fan of analogies, I planned to use one in this preface for writing a master thesis. Many ideas had already come to my mind, like blowing dandelions, bungee jumping, surfing or learning to ride a bike. But due to recent circumstances I would like to share a different message. Since the recent escalation of the corona virus, I am forced write my thesis from home. I was pretty bummed out that I lost the last few weeks of my TU Delft career to this epidemic. However, I decided that being pessimistic is not my strong suit. Life is hard, but dwelling on problems is never the solution. I decided to accept the problems as they are and to see the positive aspect of the situation. Less time lost to travelling and less expenses in general are examples of this. Fortunately for me, I did not require anything more than my laptop and time to finish this thesis, which I had plenty. The results I put down in this master thesis are something I am very proud of. And I would very much like to thank all my supervisors, Faruk, Jacco, Alexander, Matern and Miguel for their advice and helpful guidance.

N.J. de Jong
Delft, May 2020

Abstract

ISAR imaging is a well known technique which uses range and Doppler information from a radar to generate an image of a moving target. Research performed on the combination of a large receive array with airborne ISAR is scarce. This thesis is aimed to reach the highest possible image quality for AMBER, a radar with a 24 element receive array which was developed by TNO. Optimizing the image quality was split up in two parts, motion compensation and clutter suppression. A literature study is performed to research the existing methods.

A performance evaluation is performed on different motion compensation techniques based on a simulation which is set up to resemble the radar parameters of AMBER. Based on the results of this evaluation, keystone formatting combined with image contrast maximization is concluded to be the best fitting approach.

For clutter suppression a similar approach is followed with real measured data. Apart from the existing techniques, MVDR, DPCA and ODPCA, a new technique is proposed which filtered a target from clutter based on motion. It is referenced to as the IDPCA. The techniques show better image quality than regular beam forming.

To enhance the image quality more, a method is searched to combine different clutter suppression techniques. This leads to a unique method which is proposed in this thesis. The new technique exploits the circular phase variance of pixels in the range Doppler image between different sub arrays. With this approach, strong clutter can be filtered in the range Doppler domain based on its angle of arrival.

The newly proposed technique is applied as a mask, as it does not contain amplitude information of the target. Combined with the ODPCA method, the final image is generated. The combination of techniques shows clear improvements from the other discussed approaches.

List of abbreviations

AMBER Affordable Multi Beam Radar

BP Backprojection

CC Cross-Correlation

CPI Coherent Processing Interval

CSA Chirp Scaling Algorithm

DBF Digital Beam Forming

DEM Digital Elevation Map

DPCA Displaced Phase Centre Antenna

FFT Fast Fourier Transform

FM Frequency Modulated

FMCW Frequency Modulated Continuous Wave

IDPCA Inverse Displaced Phase Centre Antenna

IFFT Inverse Fast Fourier Transform

ISAR Inverse Synthetic Aperture Radar

LFMCW Linear Frequency Modulated Continuous Wave

LOS Line Of Sight

MVA Minimum Variance Algorithm

MVDR Minimum Variance Distortionless Response

ODPCA Oceanic Displaced Phase Centre Antenna

omega-k Omega-K Algorithm

PBR Peak to Background Ratio

PDF Probability Density Function

PFA Probability False Alarm rate

PPP Prominent Point Processing

PRF Pulse Repetition Frequency

PRT Pulse Repetition Time

PSF Point Spread Function

PTC Peak To Clutter ratio

PTT Peak To Target ratio

RC Range Compression

RCM Range Centroid Method

RCMC Range Cell Migration Correction

RCS Radar Cross Section

RDA Range Doppler Algorithm

RFM Reference Function Multiply

RMC Rotational Motion Compensation

SAR Synthetic Aperture Radar

SAS Static Array Shift

SLAR Side Looking Airborne Radar

SNR Signal to Noise Ratio

SRC Secunary Range Compression

SSC Stacked Subarray Combining

TDIC Time Delayed Image Combining

TMC Translational Motion Compensation

VAS Variable Array Shift

Contents

List of Figures

List of Tables

1 Introduction

Synthetic aperture radar (SAR) is a well known field in the world of radar. SAR is a processing technique which images two dimensional surfaces from an airborne or space-borne vehicle. When imaging is done with a radar, a distinction is made between two image dimensions. The range dimension, i.e. the distance from an object to the target and the cross-range dimension (also called azimuth) which is perpendicular on the range. Earlier techniques as the side looking airborne radar (SLAR)[1], only showed a high resolution in range but not in azimuth. SAR utilizes a processing technique in which the length of the antenna is synthetically increased, which drastically improves the azimuth resolution. SAR makes it possible to image areas in low visibility conditions and exploit different wavelengths to alter the penetration depth in areas, creating the possibility to look at environmental characteristics such as vegetation and soil [2]. These advantages against other imaging systems give SAR a wide range of unique applications.

The direct counterpart of SAR and also the main topic of this thesis is called inverse synthetic aperture radar (ISAR). While SAR is used to map a stationary area while moving the radar, ISAR images a target which is moving with a stationary radar. An example of an application is imaging and classifying airborne vehicles.

This thesis is done in cooperation with TNO. TNO has developed a new affordable multi beam radar (AMBER) [3]. AMBER is an X-band SAR and uses a frequency modulated continuous wave FMCW signal. With this specific radar, digital beam forming can be performed with its 24-channel receive array and a switchable transmit antenna. This new set up gives rise to a whole array of possibilities. AMBER does not yet include any algorithms for ISAR processing. The usage of airborne ISAR gives the possibility to image and classify moving ground and surface targets.

In this project in particular, maritime targets are considered. The usage of ISAR on an airborne vehicle is already less common than ground based ISAR. This is expanded one step further with the special digital beam forming radar. There are few algorithms available to exploit digital beam forming (DBF) in ISAR [4]. The combination with an airborne platform makes the project novel and unique.

The main goal of this thesis project is to find ways to exploit digital beam forming in the creation of an airborne ISAR image. It is important to take into account that during the creation of an ISAR image, a lot of processing power is needed, especially in the case of 24 different receive channels.

A second goal considers the ISAR image quality. For the purpose of classifying vessels at sea, it is effective to have a high range for detection, due to the vast space. Maximizing the range will result in a minimization of the pulse repetition frequency (PRF). As a consequence, the unambiguous Doppler will shrink. The second goal is to minimize or suppress the ambiguities that give rise through this consideration.

To effectively solve the goals stated above, they are put in a question format which can be answered. Also known as the research questions. The main research question is as follows:

- How can digital beam forming with an FMCW radar be exploited in airborne ISAR while maintaining processing limitations?

As this question on its own is to large to answer, it has been split up in several sub questions. Answering these sub questions will eventually lead to an answer on the main question in a systematic way. Each of the sub questions is shortly discussed to point out its relevance to the project.

- What different ISAR algorithms exist and how do they work?
- How can conventional ISAR algorithms be applied to a moving platform?
- How do the different ISAR algorithms perform?
- What are the options of digital beam forming in ISAR?
- What is the added value of multi-channel processing?

Engineering is not about reinventing the wheel. Using past experiences from different researchers is key to establishing the ideal approach for a problem. ISAR is a widely known topic and many different ways are discovered on how it can be applied. The first order of business is to search through literature what the possibilities are and how they are applied.

In most cases ISAR is performed with a stationary radar while observing a moving target. However, in the scenario discussed in this thesis, the radar is mounted on an aerial vehicle. This could result in a reduction of ISAR algorithms that can be applied, or change the effectiveness of some of them. This is an important point to consider. As the final algorithm should be optimized according to the system.

To determine the ideal ISAR imaging method, an evaluation will need to be performed for several options that show potential. Based on the performance of the different algorithms, the ideal solution can be chosen based on performance indicators which are related with the scenario at hand.

A big difference with conventional ISAR processing is the multichannel receiver array of AMBER. Researching the possibilities of digital beam forming in ISAR may yield options that can greatly improve the imaging quality. It will also be considered that beam forming techniques applied in different fields could be effective.

Finally some conclusion will need to be taken from the different digital beam forming options in ISAR. It will be determined if multi-channel processing is a tool that can improve the image quality of ISAR imaging. As the combination of multi-channel with ISAR is relatively rare, this is be the point where some novelty in terms of quality improvements can be generated.

Altogether, the research questions can be divided into two main problems which need to be solved in this thesis. Firstly, ISAR imaging, which will greatly consist of a motion compensation problem. And secondly, multi-channel processing, which will for the most part be a problem of clutter suppression.

The outline of the thesis is set up in such a way that the reader can logically follow the problems that are defined and the solutions that are presented. The chapters display a chronological order to maintain structure. A distinction is made between two parts in the thesis. The first part is the background and the second part the system design.

The background consists of four chapters. These chapters are written to give the reader enough background information about the used methodologies and algorithms. Chapter 2 will give a short overview of FMCW radar. This chapter shortly discusses the signal that will be used for further processing. This is an important discussion point as there is a difference between FMCW radar and pulse radar processing. The next chapter discusses the collection geometry and the signal model. Although the main topic of this thesis is ISAR, data collection of SAR and ISAR are the same in this setup. Creating an insight on how SAR works is

useful to better understand the problems posed in ISAR. Chapter 4 will discuss ISAR. This chapter will compare the differences between SAR and ISAR and will show in what way they are very similar. Furthermore, motion compensation techniques based on range alignment and phase adjustment are discussed. Followed by alternative approaches as backprojection and keystone formatting. The final chapter in the background part will discuss beam forming and clutter suppression techniques. This chapter will show several options on how the multichannel receiver array can be exploited to enhance the imaging quality.

The system design part continues with the theory discussed in the background. This part comprises four different chapters to show the process of designing the optimal algorithm for the discussed problem. Chapter 6 will discuss several of the motion compensation techniques presented in the background. A simulation of the geometric setup is created to generate a realistic model. First several algorithms are discussed based on their imaging quality. Several adaptions are made to suppress artefacts. After each modified algorithm is able to display a target correctly, a performance evaluation is done to determine which algorithm suits best. As motion compensation is the first of two large problems in this thesis, chapter 7 discusses the problem of clutter suppression. First, an alternate approach is proposed which differs from known literature. The proposed inverse displaced phase centre antenna (IDPCA) method suppresses clutter based on its motion. The new approach and several clutter suppression methods which were discussed in chapter 5 are tested and evaluated. The results presented in chapter 7 are already of high quality. Chapter 8 aims to improve the results more by combining the previously presented techniques by exploiting the multichannel receive array. Based on several experiments by splitting the receiver array in different sub arrays, a new technique is found. This newly proposed technique is very effective in discriminating the considered target from clutter from different directions. Based on the circular phase variance of different receiver sub arrays, a mask is made to filter the target from corrupting noise. To summarize the previous chapter in an understandable picture, chapter 9 shows a clear description of the final components and how they fit in the algorithm.

This thesis is concluded with a conclusion which discusses the answers to the research questions. It is supplemented with an overview of the limitations of the proposed algorithm. Finally several recommendations are presented. From the results found in this thesis, two separate conference papers are submitted.

I

Background

2

FMCW Radar Principle

To grasp the algorithms and methods discussed in later chapters, a fundamental understanding of the radar signal principles is required. Radars can be described in two different categories. The pulse radar and the continuous wave radar. For this research AMBER is used, which is a frequency modulated continuous wave (FMCW) radar. This chapter will give an introduction of how an FMCW radar measures range and velocity.

As indicated in the abbreviation, the transmitted signal of an FMCW radar uses a modulation in frequency. A few different types of modulation are commonly used: an upchirp FMCW signal, downchirp FMCW signal and sawtooth FMCW signal. An example of an upchirp FMCW signal is shown in figure 2.1. This figure shows that the transmitted signal changes frequency over time linearly, also known as linear frequency modulated continuous wave (LFMCW). The frequency sweep is limited by how large the bandwidth of the radar is and is centred around the carrier frequency. The pulse repetition time (PRT) indicates how long the chirp takes. To understand how this radar is used, first consider the phase of the transmitted signal.

$$\phi(t) = 2\pi f_c t + \frac{\pi B t^2}{T} + \phi_n(t). \tag{2.1}$$

Here f_c is the carrier frequency, B is the bandwidth over which the chirp is performed, T is the chirp time and ϕ_n is the phase noise. The phase noise will be ignored as it mainly impacts bi-static FMCW radar [5]. The transmitted signal can then be described as.

$$s_t(t) = \cos(\phi(t)). \tag{2.2}$$

This waveform travels through space until it interacts with a target. The target reflects the waveform, causing it to travel back to the radar. The distance dependent time shift can be measured in the receiver. The received

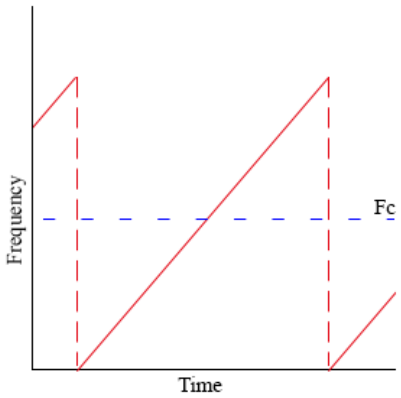

Figure 2.1: FMCW upchirp signal over time

reflected signal from a single scatterer can be described as.

$$s_r(t) = \cos\left(2\pi f_c(t-\tau) + k\pi B(t-\tau)^2\right). \tag{2.3}$$

Here, k is the chirp rate defined as $k = B/T$ and τ is the time delay which is dependent on the range and LoS velocity of the target as.

$$\tau = \frac{2(R+vt)}{c}. \tag{2.4}$$

The received signal is then mixed with the transmitted signal. In this manner, the difference in frequency between the two signals can be measured, also called the beat frequency.

$$s_m(t) = s_t(t)s_r(t). \tag{2.5}$$

This mixing procedure can be calculated by using the following trigonometric formula [6].

$$\cos(\alpha)\cos(\beta) = \frac{\cos(\alpha+\beta)+\cos(\alpha-\beta)}{2}. \tag{2.6}$$

Filling in this equation will yield one component with a very high frequency ($2f_c$) and a differential component. The high frequency component can be filtered out. The differential component is used to determine the range. Filling in equation 2.5 gives and removing the high frequency term gives.

$$s_m(t) = \frac{1}{2}\cos\left(2\pi(f_c\tau + k\tau t - \frac{k\tau^2}{2})\right). \tag{2.7}$$

This equation contains 2 phase components and one frequency component, $k\tau$. This frequency component is also called the beat frequency. To determine the beat frequency spectral estimation techniques such as the fast Fourier transform (FFT) is taken over the duration of the sweep. Resulting in a peak at the corresponding frequency. From this the time delay τ can be determined. Which gives the possibility to compute the range according to equation 2.4.

3

Collection Geometry and Signal Model

Although the focus of this thesis is on ISAR, the data collection is performed the same as in SAR and is therefore helpful to understand the geometry and signal model. The description of SAR in this section will closely follow the theory given in [7]. First, a geometrical representation will be given of the scenario, along with some key terms required to describe SAR. Then a description of the transmitted and received signal will be given. This will be followed by an explanation of how SAR utilizes a 'synthetic aperture' to create higher resolution in azimuth. Several SAR processing techniques are briefly presented in appendix A: Backprojection, RDA, CSA and omega-k.

3.1. Geometry

Before the characteristic SAR processing can be discussed, it is important to define clear variables for the geometry scheme. SAR comprises a moving antenna whilst scanning under an angle, which makes a geometrical example very useful. Although there are multiple forms of SAR, such as strip-map SAR, scanning SAR and spotlight SAR, this section will focus on strip-map SAR. Due to its simplicity it is most effective to create a general understanding of the topic. Figure 3.1 shows the geometrical setup of strip-map SAR. The slant range is defined as the distance between target and antenna. This distance changes over time while the target is illuminated with the beam. The squint angle is measured in the so called 'slant range plane'. The slant range plane is spanned by the slant range vector and the velocity vector of the antenna. The squint angle is defined as the angle between the slant range vector and the zero Doppler plane measured in the current slant range plane. The zero Doppler plane is defined as the plane perpendicular to the velocity vector of the antenna. This plane is called the zero Doppler plane, since no Doppler is measured due to the perpendicularity.

3.2. Range Equation

As typical for all different kinds of radar, range plays the most important role in SAR as well. In SAR a target is illuminated over a longer time period. During this illumination time, the slant range varies. The SAR processing creates an image based on this variation. The range equation can take multiple forms, but generally the hyperbolic form is used.

For satellite based SAR, the curvature of the earth needs to be taken into account. However, for this research, airplane based SAR is considered. In this case the curvature of the earth has a negligible impact on the measurements due to the relative small range from the airplane to the earth compared to satellite based SAR.

The hyperbolic form of the range equation assumes the Earth to be locally flat and the flight path is assumed locally straight. Assume that R_0 is the range at closest approach, v_a is the velocity of the antenna and η is the relative time between the measurement and the measurement at closest approach. Then the time dependent range is given as.

$$R^2(\eta) = R_0^2 + v_a^2\eta^2. \tag{3.1}$$

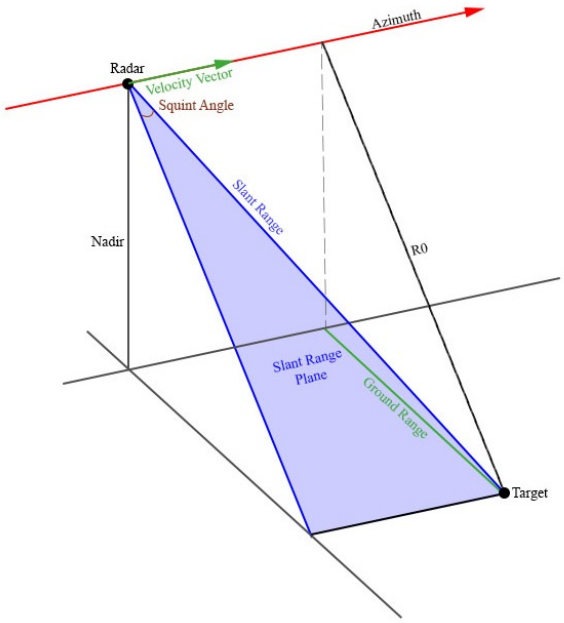

Figure 3.1: A geometrical overview of strip-map SAR

The squint angle can be defined as.

$$\sin\theta_{sq} = -\frac{v_a}{R(\eta)}. \tag{3.2}$$

When a target is still ahead of the radar, the squint angle is defined as a negative. This means that there is a negative time delay for positive squint angles. We can rewrite the squint angle as a cosine as.

$$\cos\theta_{sq} = \sqrt{1-\left(\frac{v_a\eta}{R(\eta)}^2\right)}. \tag{3.3}$$

Which we can use to simplify the range equation.

$$R_0 = \sqrt{R^2(\eta) - v_a^2\eta^2} = R(\eta)\sqrt{1-\left(\frac{v_a\eta}{R(\eta)}\right)^2} = R(\eta)\cos\theta_{sq} \tag{3.4}$$

$$R(\eta) = \frac{R_0}{\cos\theta_{sq}}. \tag{3.5}$$

3.3. Transmission

In transmission a distinction can be made between 2 cases: pulsed radar and continuous wave radar.[8] As this chapter is set up to inform about the basics of SAR, the simpler case, pulsed radar will be discussed for a plain explanation.

The radar transmits a frequency modulated time dependent pulse $s_{pulse}(\tau)$. Usually the pulse has a linear frequency modulated (FM) characteristic as in equation 3.6, although differently modulated pulse types are used as well. This project is focused around FMCW radar, so the FM pulse will be used for convenience.

$$s_{pulse}(\tau) = w_r(\tau)\cos\left(2\pi f_c\tau + \pi K_r\tau^2\right). \tag{3.6}$$

Here w_r is the pulse envelope which is approximated by a rectangular function.

$$w_r(\tau) = rect\left(\frac{\tau}{T_r}\right). \tag{3.7}$$

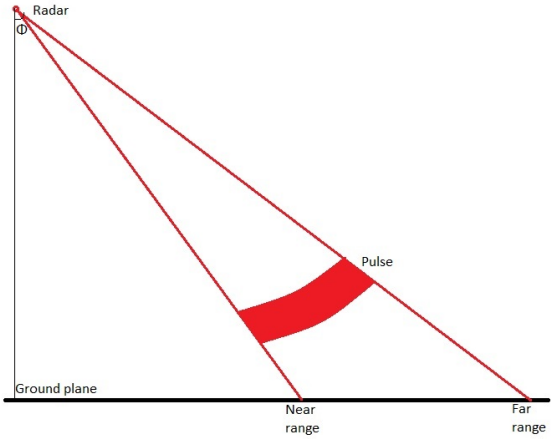

Figure 3.2: Representation of pulse propagation in the 2D plane orthogonal to the direction of motion of the radar

Where T_r is the pulse duration, f_c is the carrier frequency and K_r is the rate of change in frequency over time. Such that the instantaneous frequency for a linear frequency modulated wave is defined as.

$$f_i = f_c + K_r \tau. \tag{3.8}$$

Whether an upchirp as in equation 3.8 is used or a downchirp, does not influence the SAR equations and neither does it have an impact on the results of a measurement.
The duration of the pulse and the steepness of the chirp together indicate the used bandwidth as.

$$B = |K_r| T_r. \tag{3.9}$$

The range resolution is measured as the size of a range-bin in distance. It corresponds to the -3dB peak-width of a range compressed signal. The range resolution is directly linked to the bandwidth and is described as.

$$\delta_r = \frac{c}{2} \frac{0.886 \gamma_w}{|K_r| T_r} \approx \frac{c}{2|K_r| T_r}. \tag{3.10}$$

Here, the factor 0.886 is the -3dB peak width of a compressed pulse and γ_w is a broadening factor due to window weighting. These 2 factors tend to cancel each other and are often left out in the equation for the range resolution.

3.4. Reception

So now that the transmission parameters are defined, the receiving signal can be computed. Consider figure 3.2. The radar transmits a pulse under an angle ϕ, called the *look angle*. For now lets focus on this 2 dimensional setup. The leading edge of the pulse interacts with the near region first and the trailing edge of the pulse interacts with the far region last. A target which the pulse interacts with may induce a phase shift or change the amplitude of the pulse, which can later be used to classify the object.

The received pulse for each individual point scatterer in the illuminated area between near range and far range can be described as.

$$s_r(\tau) = A_r s_{pulse}\left(\tau - \frac{2R_{ps}}{c}\right). \tag{3.11}$$

Where A_r is the amplitude of the pulse, caused by the back-scatter coefficient of the point target and R_{ps} is the range to the point scatterer. When combining equations 3.6 and 3.11, the received signal can be written as.

$$s_r(\tau) = A_r w_r\left(\tau - \frac{2R_{ps}}{c}\right) \cos\left[2\pi f_c\left(\tau - \frac{2R_{ps}}{c}\right) + \pi K_r\left(\tau - \frac{2R_{ps}}{c}\right)^2 + \psi\right]. \tag{3.12}$$

Where ψ is a variable which indicates the phase shift caused by the target.

3.5. Synthetic Aperture

While different targets in the range direction are distinguished by their time delay, different targets in the azimuth direction can be distinguished by Doppler. Targets left of antenna bore sight have a relative negative velocity and show a negative Doppler, and targets right of antenna bore sight have a relative positive velocity, showing a positive Doppler. The change in Doppler over azimuth is linear with the velocity of the antenna. Based on the Doppler and the round trip time delay, the location of a target can be estimated, as is done in the Range Doppler Algorithm (RDA).

The range resolution has been defined in equation 3.10. In the azimuth direction, the resolution is dependent on the beam-width of the radar. When no SAR processing is applied, target points on varying azimuth are indistinguishable for the entire projection of the beam-width on the ground. Such that the azimuth resolution becomes.

$$\delta_a = R(\eta_c)\theta_{bw} = \frac{0.886R(\eta_c)\lambda}{L_a}. \tag{3.13}$$

Where L_a is the antenna length and $R(\eta_c)$ is the range to the beam center. This resolution is the resolution of a real aperture radar. SAR uses a synthetic aperture to increase the resolution. As can be seen in equation 3.13, decreasing the beam-width will improve the resolution. Since the range to the target is not a changeable variable and the wavelength is limited by factors such as propagation loss, the antenna length can be exploited to improve the resolution.

To clearly explain why the resolution improves when the antenna length is increased, and how this can be applied in SAR, it is useful to first consider a phased array. In a phased array, multiple antennas are used to decrease the main lobe beam-width of the radar pattern. When considering the far-field, the radiation pattern can be described as the summation of the antennas.

$$P_a(\theta) = \sum_n \exp\left(-j2\pi \frac{x[n]\theta}{\lambda}\right). \tag{3.14}$$

Where $x[n]$ is the distance of the n^{th} antenna element and θ is the radiation direction in azimuth. This sum corresponds to the discrete Fourier transform of the rectangular function and converges to the following Fourier integral.

$$P_a(\theta) = \int_{-L_a/2}^{L_a/2} \exp\left(-j2\pi \frac{x\theta}{\lambda}\right) dx = L_a \text{sinc}\left(\frac{L_a\theta}{\lambda}\right). \tag{3.15}$$

This equation shows a clear relation between the antenna length and the beam-pattern. Increasing the antenna length will decrease the width of the main lobe of the beam and thus improve the resolution.

To understand how this feature can be exploited in SAR, consider figure 3.3. This figure shows the comparison between SAR and a phased array. These 2 scenarios are very alike. It is important to note that for SAR a 2-way channel is used, giving an extra factor 2 in the range equations. The length of the synthetic aperture can be written as.

$$L_s = \frac{0.886R(\eta_c)\lambda}{L_a}. \tag{3.16}$$

And the new resolution in the azimuth direction can be described as.

$$\delta_a = R(\eta_c)\frac{0.886\lambda}{2L_s}. \tag{3.17}$$

3.6. Data Storage

Although each pulse contains both range and azimuth information, it is still received at the radar as a one dimensional signal of the amplitude of the received voltage versus time. To prepare the data for processing, each consecutive pulse is stored parallel to the previous one, creating an array. In this array, each row represents a single measurement with varying ranges. Such a row is also known as a **range line**, and also referenced to as fast time. For each point in a single column of the array, the value describes a point measured at the same range. These columns are known as **range gates**, and are referenced to as slow time.

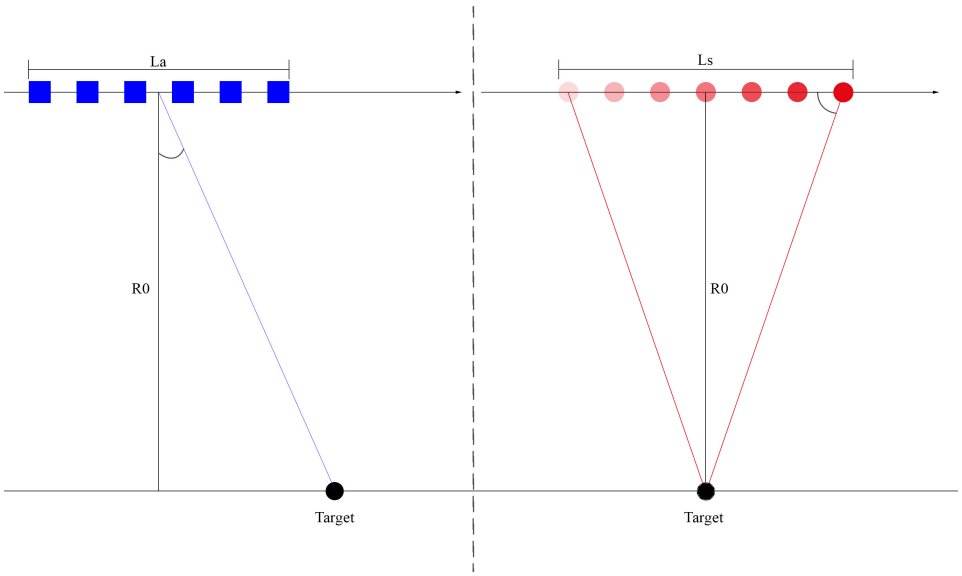

Figure 3.3: Illustration of the similarities between a phased array and SAR

To process the data, first the received signal is demodulated, the radar carrier is removed. This is done by a quadrature demodulation process. The demodulated signal for a single point scatterer written as a function of slow time and fast time is then given as.

$$s_0(\tau,\eta) = A_0\, w_r\left[\tau - \frac{2R(\eta)}{c}\right] w_a[\eta-\eta_c]\exp\left(-j4\pi f_c\frac{R(\eta)}{c}\right)\exp\left(j\pi K_r(\tau-\frac{2R(\eta)}{c})^2\right). \tag{3.18}$$

Where A_0 is a complex constant dependent on the real amplitude coefficient, A_0'

$$A_0 = A_0' e^{j\psi}. \tag{3.19}$$

All types of data processing start with this demodulated base-band signal. Several SAR processing techniques that use this signal can be found in appendix A.

4

ISAR

As the main principles of SAR have been discussed, the main princples of ISAR will be discussed in this chapter. The theory given in [9] is followed closely. The techniques SAR and ISAR are very similar, but have some generic differences. With SAR, the radar platform moves to create a synthetic aperture, while targets in the constructed image are considered stationary. In ISAR, logically enough, the inverse of this procedure happens. The radar platform is stationary, and moving targets are observed. When comparing spotlight SAR with a simple ISAR configuration as given in figure 4.1, it can be seen that both configurations are equall except for a change of reference system.

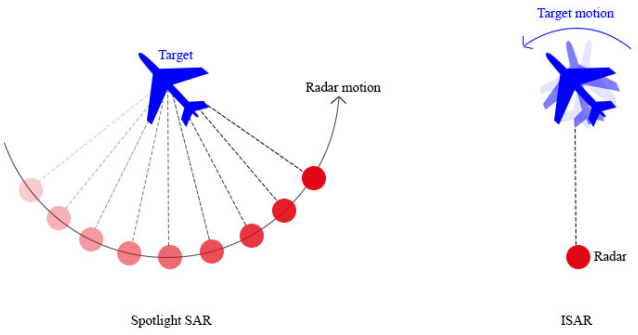

Figure 4.1: Comparison between spotlight SAR and ISAR

Although this is defined as the difference between SAR and ISAR. The most important distance is the matter of target cooperation [9]. Between the two cases, the movement of the radar platform for SAR can be compared to the movement of the target for ISAR, as in figure 4.1. The problem is that for SAR the movement is known of the radar platform, but for ISAR it may be possible that the movements of a target can not be predicted, the target shows noncooperative motion. ISAR processing techniques are aimed to perform motion compensation for the target to acquire sharp images.

4.1. Target Model

Before going into the ISAR algorithms, lets first consider a model for a target in motion. Such a target can be described as a rigid body with six degrees of freedom. Translation movements in the x, y and z directions and the rotational movements roll, pitch and jaw $(\Omega_r, \Omega_p, \Omega_j)$.

Motion can generally be described as a velocity and an acceleration component (v, a). In ISAR the translational motion is then again subdivided into 2 components, the component along the line of sight (LOS) (v_{los}, a_{los}) and the component perpendicular to the LOS $(v_\perp, a_\perp)$. The LOS component determines the Doppler

shift measured at the receiver. The perpendicular component changes the target aspect angle over time, giving a similar effect as the rotational motions.

The rotational motions can be modelled as constant for a short period of time. Different scatterers on the rigid body will cause different Doppler shift, but all scatterers show the same rotational constants. This assumption can only be made for a very short period of time, as non-cooperative motion can change jaw, pitch and roll at any moment.

The round trip delay in ISAR is similar as in SAR. For now, the acceleration term has been left out, since it is negligible in this setup.

$$\tau(t) = 2\frac{|\mathbf{r}(t) - \mathbf{R}_0|}{c - v_r}. \tag{4.1}$$

In this equation, $\mathbf{R}_0$ is the vector from the center of the target to the radar and $\mathbf{r}(t)$ is the time dependent position vector of a scatterer.

$$\mathbf{r}(t) = \mathscr{R}(\theta_r, \theta_p, \theta_y)\mathbf{r}(t_0). \tag{4.2}$$

Where $\mathbf{r}(t_0)$ is the time dependent position vector at t_0 with respect to the target center, $\mathscr{R}$ is the rotation matrix and the roll pitch and yaw angles correspond to.

$$\begin{aligned} \theta_r &= \Omega_r t, \\ \theta_p &= \Omega_p t, \\ \theta_y &= \Omega_y t. \end{aligned} \tag{4.3}$$

Now that the scatterers' range is determined, the next step is to determine the Doppler in this model. First of all, v_{los} is defined as the projection of the velocity vector of the target on the LOS unit vector $\mathbf{i}$(t).

$$v_{los}(t) = \mathbf{v}(t) \cdot \mathbf{i}(t). \tag{4.4}$$

The Doppler frequency is given as.

$$f_d(t) = \frac{2f_c|\mathbf{v}(t) \cdot .\mathbf{i}(t)|}{c} \tag{4.5}$$

Where $v(t)$ can also be rewritten as.

$$\mathbf{v}(t) = \mathbf{\Omega}(t) \times \mathbf{r}. \tag{4.6}$$

In this equation, $\mathbf{r}$ is the distance vector between a scatterer and the target center and $\mathbf{\Omega}(t)$ is the targets rotation vector.

Knowing the basic motion model of a target, lets take a view at the basic ISAR procedure. In general ISAR can be described in 3 simple steps: preprocessing, range processing and cross-range processing.

- **Preprocessing** removes amplitude and phase errors, unwanted artifacts, modulations and interferences from the raw data which occurred during data collection.
- **Range processing** is done to compensate for the translational motion of the target. Also referred to as translation motion compensation (TMC).
- **Cross-range processing** is done to compensate the rotational motion a target may have. Also referred to as rotational motion compensation (RMC).

The general key to creating an ISAR image is to estimate the motion parameters. If all motion parameters can be precisely predicted, then the phase can be compensated and a sharp ISAR image can be created. To do this, there are many different methods. Some will be discussed in the following sections.

4.2. ISAR Imaging

The range Doppler algorithm is the most straightforward algorithm to create an ISAR image [10, 11]. It shapes the foundation on which the other imaging algorithms are formed. The regular RDA does not include any motion compensation but directly forms the image from the retrieved demodulated signal by applying the 2-dimensional Fast Fourier transform. Figure 4.2 shows the simplicity of the model.

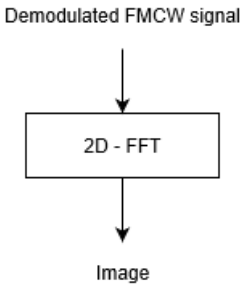

Figure 4.2: Flow diagram of the range Doppler algorithm

However, since the RDA does not take into account any motion of the radar or target, a smear is created in the image. The ISAR image is a capture of the targets range and Doppler, but can not include any time-dependent changes, since it is only 2-dimensional. Since the target has a different range at each sweep, all the different ranges are displayed in the image, creating a smear. An example of such a smear is shown in figure 4.3. This figure shows a smear in Doppler as well due to range Doppler coupling.

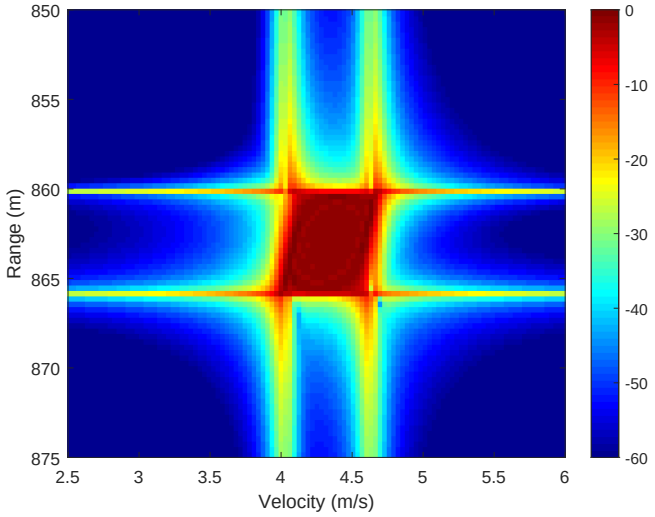

Figure 4.3: Moving point target processed without any motion compensation

To understand where this range Doppler coupling comes from, consider the demodulated signal.

$$S(f,t) = \exp\left(i\frac{4\pi}{c}(f+fc)\left(r + v_{los}t + \frac{a_{los}}{2}t^2\right)\right). \tag{4.7}$$

The coupling is clearly visible in this equation as $f v_{los} t$. The final term, $f\frac{a_{los}}{2}t^2$ contributes as well, although this is generally not the dominant term due to the exponent over the short time interval.

The following sections will describe some algorithms which 'manipulate' the time signal such that the target appears to be in the same range bin at all times, solving the smearing problem. Within this process, a distinction is made between range- and Doppler-smearing. Range alignment and phase adjustment are applied respectively. During the discussions on these algorithms the theory in [9] is followed.

4.3. Translational Motion Compensation

In a scenario where the target, the radar or both are moving, it is necessary to apply translational motion compensation to generate an image. The reason for this compensation is the movement of scatterers through range profiles in the image. The TMC can be split up in two procedures. First, 'range alignment' is applied to force a single scatterer to remain in the same range bin. Hereafter, phase adjustment is necessary to remove

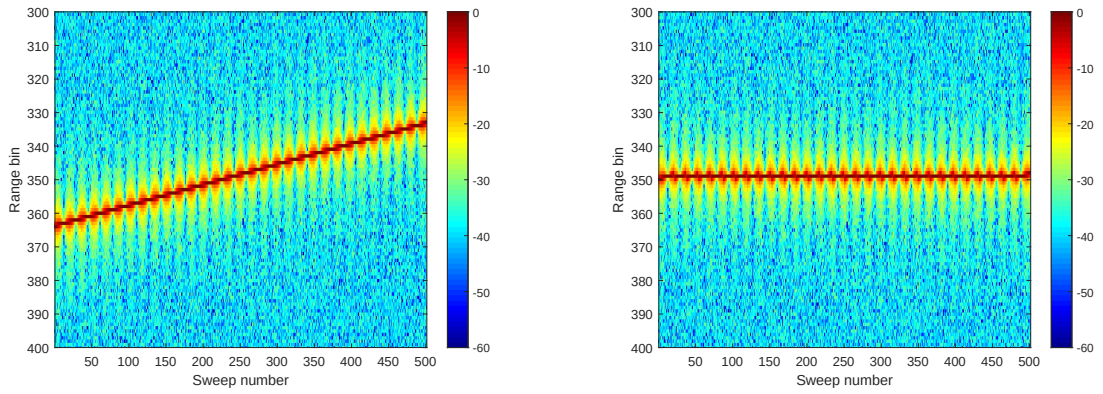

(a) Scatterer showing range cell mirgration over time

(b) Scatterer after range alignment

Figure 4.4: Range-time domain image of a single scatterer before and after range alignment

phase errors. There are several different techniques that are used for TMC. The following common techniques will be discussed in this chapter.

Range alignment techniques

- Range centroid
- Cross-correlation
- Minimum entropy

Phase adjustment techniques

- Doppler centroid
- Phase Gradient
- Minimum variance
- Entropy

4.3.1. Range Alignment

Cross-correlation method (CC) The cross-correlation method is a means of range alignment. Although the method itself is very straightforward, the implementation is often different and at times it is combined with different algorithms [12–14].

The cross-correlation method is applied in the range-time domain. As a scatterer changes range bins over time, range alignment is necessary to force the scatterer to remain in the same range bin. An example where range alignment is applied is shown in figure 4.4.

For each pulse, the cross-correlation is taken between the range vector of that pulse and a reference pulse. This will yield a maximum at the bin number which indicates the displacement of the scatterer with respect to the reference pulse. The range vector is circularly shifted according to this bin-displacement and this procedure is repeated for all range vectors.

Since calculating the cross-correlation is computationally expensive, this operation is done in the Fourier domain. As the cross-correlation is equal to a multiplication in the Fourier domain, this procedure increases the computational speed significantly. A flow chart of the cross-correlation method is shown in figure 4.5.

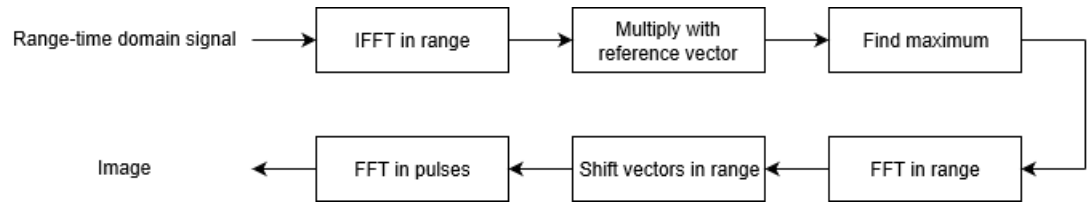

Figure 4.5: Flow chart of the cross-correlation method

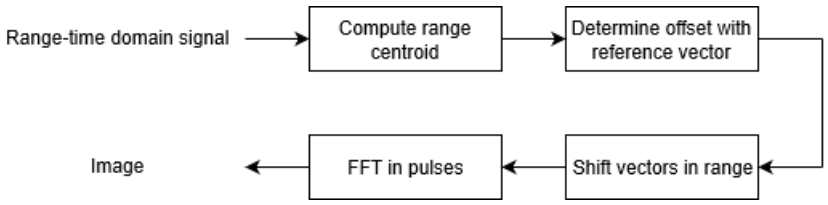

Figure 4.6: Flow chart of the range centroid method

Range centroid method (RCM) The range centroid method is a different method to determine the required range cell migration. This method does not require a comparison between range-vectors as the cross-correlation method, but considers each range-vector individually.

In this method, the required shift is determined by the center of mass in each range-vector. This center of mass, or 'centroid' can be calculated for a discrete signal $S = [s_1, s_2, ..., s_K]$ as.

$$Centroid = \frac{\sum_{k=1}^{K} k \cdot s_k}{\sum_{k=1}^{K} s_k}. \tag{4.8}$$

Although this method is faster than the cross-correlation method, it is also sensitive to noise. A flow chart of the range centroid method is shown in figure 4.6.

Entropy minimization Another method which is used for TMC is entropy minimization. Entropy itself is not an algorithm, but a function and thus has this method many forms of implementations [15],[16]. Entropy minimization is widely used, but relatively slow due to the exhaustive searching procedure it uses [17]. This is a statistical method where entropy stands for a measure of unpredictability. Consider the discrete random variable $S = [s_1, s_2, ..., s_K]$ which has a probability density function of $p(s_k) \geq 0$. The expected value is then $E(S) = \sum_{k=1}^{K} s_k p(s_k)$ and the Shannon entropy is defined by [18].

$$H(S) = -\sum_{k=1}^{K} p(s_k) \log p(s_k). \tag{4.9}$$

This equation is a quantification of the unevenness from the probability density function. This method uses the entropy to evaluate the range cell alignment. The entropy is small when $p(s_k)$ is high i.e. there is a dominant scatterer. When summing over the ranges, the peak at the scatterer should be largest when range cell alignment is applied correctly, which gives a minimum entropy. The minimum entropy can be found by rewriting the Shannon entropy function as.

$$H(S_n, S_{n+1}) = -\sum_{c=1}^{C} p(m,c) \log p(m,c). \tag{4.10}$$

Where C is the number of range cells in a profile. The probability density function (PDF) is then defined as;

$$p(m,c) = \frac{|S_n(c)| + |S_{n+1}(c-m)|}{\sum_{c=0}^{C-1} (|S_n(c)| + |S_{n+1}(c-m)|)}. \tag{4.11}$$

The required range bin shift, m, can then be determined by finding the value of m for which the entropy function is minimum.

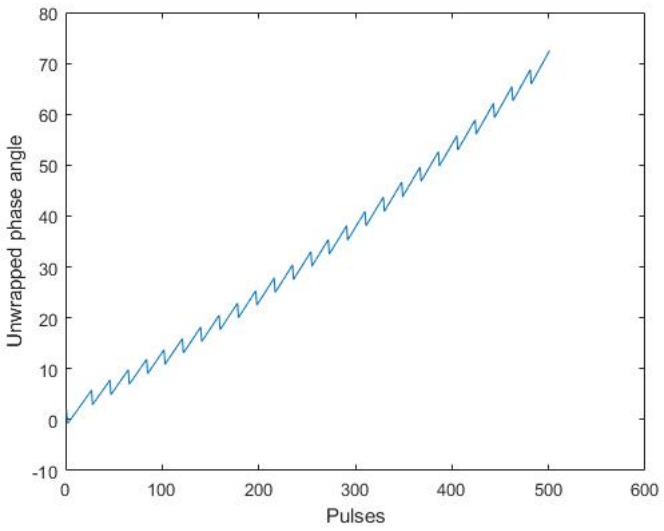

Figure 4.7: Unwrapped phase angle of a point scatterer after range alignment

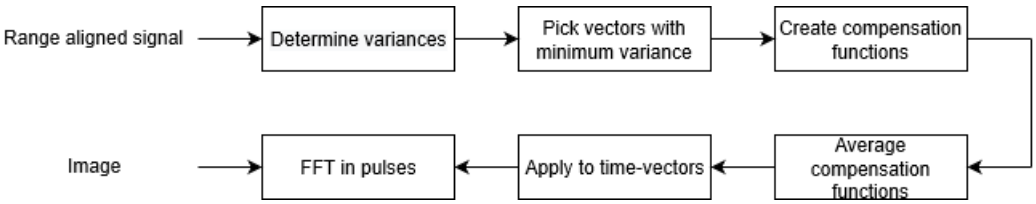

Figure 4.8: Flow chart of the minimum variance algorithm

4.3.2. Phase Adjustment

As the range alignment is performed by shifting range-vectors to create a stationary target in range, phase errors originate from this very shift apart from the smear in Doppler that was already apparent. Consider figure 4.7. This figure shows the unwrapped phase of the point scatterer after range alignment is applied. Clearly, the phase has become non-linear due to the range correction. This will result in replicas of the target in the image. This effect is unwanted, such that phase adjustment needs to be applied. Several methods to apply phase adjustment are discussed in this section.

Minimum variance algorithm (MVA) The minimum variance algorithm is used to linearise the phases of the scatterers. This method consists of 2 main steps;

- The variance of all time-vectors is determined and a small number of vectors (e.g. 3) with the minimum variances are picked. These picked vectors are generally scatterers.
- For each of the scatterers, a phase compensation function is created to linearise the phase. The average of the phase functions is taken and applied to all the time-vectors.

The algorithm is quite simple and fast. However, since the phase change is different for each scatterer, it is not possible to linearise the phases of all the scatterers. A flow chart of the minimum variance algorithm is shown in figure 4.8.

Doppler centroid The procedure for applying Doppler centroid for phase compensation is very similar as the range centroid method. First, the Doppler spectrum is created to show the different Doppler components over time. Then, the Doppler centroid is determined by calculating the center of mass as in equation 4.8. The Doppler vectors are then shifted according to a reference vector. From this new adjusted data-set, the image is created and the smears in Doppler are solved as the point scatterers are set to a stationary velocity by this method.

Entropy minimization Applying entropy minimization for phase adjustment is a so called parametric method. This means that before this method can be applied, an estimation needs to be done for the velocity and acceleration of the target. One effective way to determine these parameters is by prominent point processing (PPP). When the estimated motion parameters are not optimal, a smear still exists in the range Doppler image. A 2-D entropy minimization method is applied to find the 2 optimal parameters. This follows the same procedure as for range alignment. When the velocity and acceleration are determined, the required phase shift can be calculated as.

$$\phi(t) = vt + \frac{1}{2}at^2. \tag{4.12}$$

This phase is added to the range compensated signal in the range time domain. Just as in the other methods, an FFT is then taken to generate the focussed range Doppler image.

4.4. Rotational Motion Compensation

After the translational motion compensation is applied, the target can be seen as fixed at a position in space. However, the target may still display rotational behaviour about its own axis. When considering maritime vessels as in this thesis, this rotational motion is mostly caused by the displacement of the radar with respect to the target. To counter this, rotational motion compensation needs to be applied. Some methods that are commonly used are polar reformatting, entropy minimization, phase gradient autofocusing and image contrast maximization.

4.4.1. Image Contrast Maximization

Compensating the valid acceleration parameter of a target will change the image quality considerably. To understand how this acceleration parameter can be found, a better look needs to be taken at the relation between the acceleration error and the image contrast. The image contrast function is an image quality measure and is defined as [19].

$$IC = \frac{\sqrt{A\left((|I| - A(|I|))^2\right)}}{A(|I|)}. \tag{4.13}$$

Where $A(\cdot)$ is the mean and I is the complex image after compensating for the acceleration by the acceleration term.

$$\phi_a(f,t) = -i\frac{4\pi}{c}(f+f_c)\alpha_{est}\left(\frac{f_c t}{f+f_c}\right)^2. \tag{4.14}$$

Where α_{est} is an estimation of the acceleration. A parameter sweep on the acceleration estimate is performed to find the highest resulting image contrast. The complex image can be described as.

$$I = \mathfrak{F}_2(S_c(f,t)\exp(\phi_a(f,t))). \tag{4.15}$$

Where $S_c(f,t)$ is the demodulated signal after fold-over correction and $\mathfrak{F}_2$ indicates the 2-dimensional Fourier transform.

4.4.2. Prominent Point Processing

The polar formatting algorithm [20] is an imaging technique that does require information about the angular velocity of the target. Due to this prerequisite, this algorithm is combined with a technique to estimate the rotation parameters. This is usually done by prominent point processing.

Prominent point processing selects one or multiple prominent scatterer and follows them to extract motion parameters of the target. In the stage of RMC, it is assumed that the translational motion compensation is already done and the center of the target is known. The range to a point on the target can then be described as.

$$R_P(t) = R_0 + r_P\cos\left(\theta_0 + \theta_P + \Omega t + \frac{1}{2}\gamma t^2\right). \tag{4.16}$$

Where θ_0 is the original aspect angle of the target, r_P and θ_P are the polar coordinates of the point scatterer, Ω is the angular velocity and γ is the angular acceleration. The angular acceleration is considered negligible at this stage. Then the velocity and the acceleration of a scatterer are described as.

$$v_P(t) = \frac{d}{dt}R_P(t) = -\Omega r_P\sin\left(\theta_0 + \theta_P + \Omega t + \frac{1}{2}\gamma t^2\right). \tag{4.17}$$

$$a_P(t) = \frac{d^2}{dt^2} R_P(t) = -\Omega^2 r_P \cos\left(\theta_0 + \theta_P + \Omega t + \frac{1}{2}\gamma t^2\right). \tag{4.18}$$

To determine the angular velocity of the target, a prominent point which is located at zero Doppler (or zero velocity) is chosen (preferably far away from the target center) and the range is taken from the center of the target. This gives.

$$v_P = -\Omega r_P \sin\hat{\theta}_P = 0. \tag{4.19}$$

Where $\hat{\theta}_P$ is the average rotation angle during the CPI. The range and acceleration in this interval can be written as;

$$R_P = r_P. \tag{4.20}$$

$$a_P = -\Omega^2 r_P. \tag{4.21}$$

From which the angular velocity can be derived as.

$$\Omega = \left(\frac{a_P}{R_P}\right)^{1/2}. \tag{4.22}$$

A similar procedure can be done to determine the acceleration parameter by picking a prominent point which has the same range as the target center, but a different velocity.

4.5. Range Doppler Backprojection

Not all algorithms are based on the principle of range alignment and phase adjustment. The Range Doppler Backprojection algorithm was inspired by the time domain backprojection algorithm used in SAR imaging [21]. The idea of this function is to estimate the target's range and velocity by 'trying' different velocities and adding the contribution of each velocity to the corresponding range bins. This algorithm is applied in the range time domain. Consider the time delay induced by the target's range and potential velocity as.

$$\tau_i(v_p) = 2\frac{R_0 - i\, v_p T_f}{c}. \tag{4.23}$$

In this equation v_p is a potential target velocity, R_0 the initial range, T_f is the fast time and i is the pulse index. According to this time delay estimate, motion compensation and phase correction can be applied to the range time domain signal y.

$$z_i(t, v_p) = y_i(t + \tau_i(v_p)) e^{j2\pi f_c \tau_i(v_p)}. \tag{4.24}$$

After the motion compensation and phase correction are applied, a summation is done over the pulses to determine the contribution of each selected velocity;

$$d(r, v_p) = \sum_i z_i(t = 2r/c, v_p). \tag{4.25}$$

Where r contains the considered range vector ($R_{min} < r < R_{max}$) and v_p contains the considered velocity vector. It is important to note that it is possible to choose these vectors according to prior knowledge of the target. This way, only the relevant ranges and velocities are considered, reducing the computational resources necessary for this algorithm.

Although this variant of backprojection is quite different as time domain backprojection in SAR, time domain backprojection can also be applied in ISAR with a few adaptions. Appendix B shows a simulation of how time domain backprojection can be applied. However, this form of the method can not be applied with airborne ISAR, as the rotation angle caused by the translational motion is too small.

4.6. Keystone Transform

Just as the Range Doppler Backprojection algorithm, keystone formatting does not rely on the typical range alignment and phase adjustment procedures. The keystone algorithm directly applies an interpolation filter on the demodulated signal [22]. This filter is shaped as a keystone, whereas the name originates. Let's directly consider the demodulated signal for N targets.

$$S(f, t) = P(f) \sum_{n=1}^{N} A_n \exp\left(i\frac{4\pi}{c}(f + f_c)\left(r_n + \dot{r}_n t + \frac{\ddot{r}_n}{2} t^2 + ...\right)\right). \tag{4.26}$$

In the demodulated signal, the range is expressed as a Taylor series expansion defined as follows.

$$R_n(t) = r_n + \dot{r}_n t + \frac{\ddot{r}_n}{2} t^2 + ... \tag{4.27}$$

Where each individual term can also be written as.

$$r_n = \sqrt{(x_p - x_t)^2 + (y_p - y_t)^2 + (z_p - z_t)^2}. \tag{4.28}$$

$$\dot{r}_n = \frac{x\dot{x} + y\dot{y} + z\dot{z}}{\sqrt{x^2 + y^2 + z^2}}. \tag{4.29}$$

$$\ddot{r}_n = (\dot{x}^2 + \dot{y}^2 + \dot{z}^2 + x\ddot{x} + y\ddot{y} + z\ddot{z}) - \frac{(x\dot{x} + y\dot{y} + z\dot{z})^2}{x^2 + y^2 + z^2}. \tag{4.30}$$

Where $x = x_p - x_t$, $y = y_p - y_t$ and $z = z_p - z_t$. Note that the first and second order terms in equation 4.27 represent velocity and acceleration. The higher order terms in the range expansion are generally negligible. Consider equation 4.26, each of the terms in this equation contributes to the final range Doppler image after applying the 2-dimensional Fourier transform. To get a clear idea of how the image is formed, it is useful to consider what impact each individual term has on the created image. Table 4.1 gives an overview [23].

Event	Phase term
Range position	$f r_n$
Range walk	$f \dot{r}_n t$
Range curvature	$f \ddot{r}_n t^2/2$
Azimuth phase	$f_c r_n$
Azimuth translation	$f_c \dot{r}_n t$
Azimuth smear	$f_c \ddot{r}_n t^2/2$

Table 4.1: Phase terms and their consequences of the received demodulated signal

Table 4.1 shows that the coupling between time and frequency results in range walks and range curvatures in the imaging domain. The first order keystone compensates the range walk by applying an interpolation filter which cancels the time-frequency dependency. The time scaling for this interpolation filter is.

$$t_k = t \frac{f_c}{f_c + f}. \tag{4.31}$$

Such that the signal after the keystone transform becomes.

$$S(f, t_k) = P(f) \sum_{n=1}^{N} A_n \exp\left(i \frac{4\pi}{c} \left(\dot{r}_n f_c t_k + (f + f_c) \left(r_n + \frac{\ddot{r}_n}{2} \left(\frac{f_c t_k}{f + f_c} \right)^2 + \frac{\dddot{r}_n}{3} \left(\frac{f_c t_k}{f + f_c} \right)^3 \right) \right) \right). \tag{4.32}$$

This shows that the term causing range walk is compensated, sharpening the image.
An important thing to consider is that the keystone transform is bound to the ambiguous velocity of the target with respect to the radar. If a target exceeds this threshold, it will remain blurred. However, this can be compensated as long as the number of fold-overs in ambiguity is known.
When f_m is the measured frequency and F is the fold-over number, the real frequency f_r can be written as.

$$f_r = f_m + \frac{F}{T}. \tag{4.33}$$

Where T is the pulse duration. The fold-over can then be compensated as.

$$S_c(f, t_k) = S(f, t_k) \exp(i 2\pi t \frac{F}{T}). \tag{4.34}$$

After compensating this term, the image may still be unsharp due to the second order time-frequency coupling. Another phase compensation term considering the acceleration can be applied to sharpen the image. This term is expressed as.

$$\phi_a(f, t_k) = -i \frac{4\pi}{c} (f + f_c) \alpha_{est} \left(\frac{f_c t_k}{f + f_c} \right)^2. \tag{4.35}$$

To correctly compensate for the acceleration, α_{est}, an estimation of this term is required. This can be done by techniques as prominent point processing or image contrast maximization.
A different option which does not include the necessity for prior knowledge on the acceleration of the target is the second order keystone transform [23]. As the name implies, this method compensates for the second order term in the demodulated signal given in equation 4.26. Which simply gives an interpolation filter as follows.

$$t_k = t\left(\frac{f_c}{f_c + f}\right)^{1/2}. \tag{4.36}$$

After interpolation of the demodulated signal according to the second order keystone transform, the resulting signal is written as.

$$S(f, t_k) = P(f) \sum_{n=1}^{N} A_n \exp\left(i\frac{4\pi}{c}\left((f + f_c)r_n + \dot{r}_n t_k f_c^{1/2}(f_c + f)^{1/2} + \frac{\ddot{r}_n f_c}{2} t_k^2\right)\right). \tag{4.37}$$

This shows that the time-frequency coupling which resulted in range curvature is solved. However, the time-frequency coupling responsible for the range walk is still present. In this case, it can be compensated by a term which is dependent on velocity.

$$\phi_v(f, t_k) = -i\frac{4\pi}{c} v_{est} t_k f_c^{1/2}(f_c + f)^{1/2}. \tag{4.38}$$

Since applying a 2-dimensional interpolation filter on a large data set is computationally expensive, methods have been devised to accelerate the processing speed. By using the chirp-scaling principle, the keystone transform can also be performed by only applying multiplications and Fourier transforms [24].

5

Beam Forming and Clutter Suppression Techniques

The property that differs in AMBER from other airborne ISAR imaging systems is its multichannel receive array. With 24 receivers, there are a lot of options to use beam forming techniques for an increased performance of the ISAR image. Some of those are discussed in this chapter.

5.1. Digital Beam Forming

Once the location (i.e. range and angle of arrival) of a target is known, the data in the receiver array can be manipulated to form a 'digital' beam towards the target. In this manner, all reflections coming from a chosen angle form constructive interference. While different angles do not, or suffer from destructive interference.

Consider an ideal isotropic transmitter. When forming an array of such transmitters, the radiation pattern is named the array factor (AF) [25]. The array factor is dependent on the electric length between the transmitters, kd, and the induced phase shift β. The array factor of an N-element linear array with a progressive phase shift can be described as.

$$AF = \sum_{n=1}^{N} \exp i(n-1)(kd\cos\theta + \beta). \tag{5.1}$$

Which can also be written as.

$$AF = \left[\frac{\sin\psi\frac{N}{2}}{\sin\frac{\psi}{2}}\right]\exp i\left(\frac{N-1}{2}\right)\psi. \tag{5.2}$$

Where ψ is the phase shift between adjacent transmitters, $\psi = kd\cos\theta + \beta$. Note that for each induced phase β there exists a θ at which all transmitters sum up coherently, which is the fundamental for beam-forming. Given as $\beta = -kd\cos\theta$.
In case of DBF, the procedure is exactly the same. The progressive phase shift is not added to the transmitted signal, but to the received signal, yielding the same antenna patterns. Figure 5.1 shows an example of the array factor in 2 different scenarios. One where no phase shift is induced, and one where the beam is steered 20 degrees towards the front end of the antenna array. It is important to note that in this case θ is defined as the angle along the antenna array.
Just as the antenna has maxima where there is constructive interference, it also has nulls where there is destructive interference. These nulls can be found by setting the numerator in equation 5.2 to zero.

$$\sin\psi\frac{N}{2} = 0. \tag{5.3}$$

$$\theta_n = \arccos\left(\frac{1}{kd}\left(-\beta \pm \frac{2n}{N}\pi\right)\right), n = 1,2,3,... \tag{5.4}$$

In a similar manner, the secondary maxima of the array factor can be found by maximizing the numerator in equation 5.2.

$$\sin\psi\frac{N}{2} = \pm 1. \tag{5.5}$$

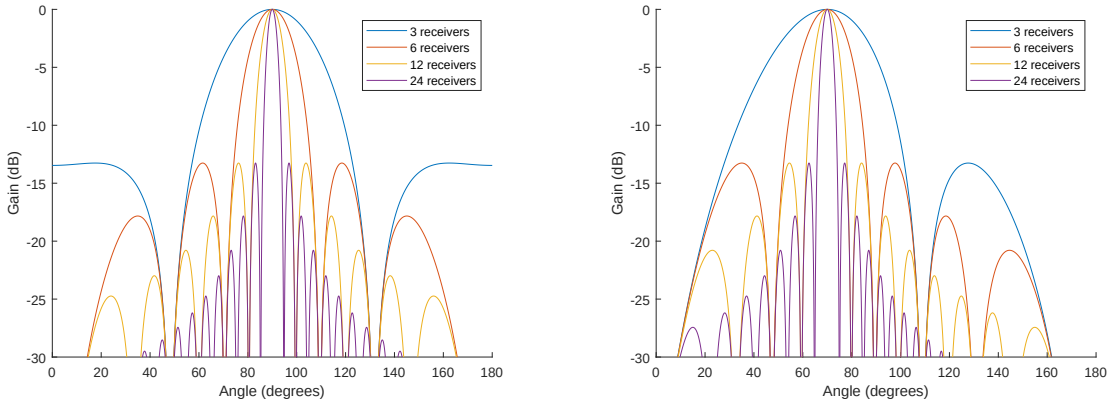

(a) 0 degrees from normal on array

(b) 20 degrees from normal on array

Figure 5.1: Array factor for different normal angles on the array with varying number of receivers

$$\theta_m = \arccos\left(\frac{1}{kd}\left(-\beta \pm \frac{2s+1}{N}\pi\right)\right), s = 1,2,3,... \tag{5.6}$$

To give an idea of how wide the beam of the 24 receive array is, consider the half power beam-width (HPBW).

$$AF^2 = 0.5. \tag{5.7}$$

Which can be approximated as.

$$\frac{N}{2}(kd\cos\theta_h + \beta) = \pm 1.391. \tag{5.8}$$

Such that,

$$\theta_h = \arccos\left(\frac{1}{kd}\left(-\beta \pm \frac{2.782}{N}\right)\right). \tag{5.9}$$

Note that the HPBW changes for different θ. If we define D as the cross-range distance covered by the HPBW, this can be found as.

$$D = 2R\sin(\theta - \theta_h). \tag{5.10}$$

5.2. MVDR

Another application of DBF is suppressing clutter, a secondary target or a jammer. This can either be done by the minimum variance distortionless response (MVDR) or any null-steering technique if the location of the jammer is known. MVDR changes the weight vector such that the output power is minimized while the power in the look direction remains the same [26]. The equation for the MVDR weighting vector is,

$$w = \frac{R^{-1}a(\theta)}{a^H(\theta)R^{-1}a(\theta)}. \tag{5.11}$$

Where $a(\theta)$ is the steering vector and R is the covariance matrix of sensors versus cropped fast time.

5.3. DPCA

The displaced phase centre antenna technique is performed with two or more sub arrays. The first sub array measures from location x at t_0 and as the platform moves, the second sub array reaches location x, measuring at t_1. Subtracting the two sub arrays from each other will remove all the stationary components in the image, as their reflection did not change over time.

For this technique to work, the two sub arrays need to be exactly aligned: their locations should be the same before subtracting each other. As this is generally not the case, an additional alignment step needs to be performed, which will be elaborated on later.

Consider a radar platform of 24 receivers which moves at a velocity of v_{radar}. The best sub array size depends on the radar velocity, the length of the array and the distance between the elements. Figure 5.2 shows an

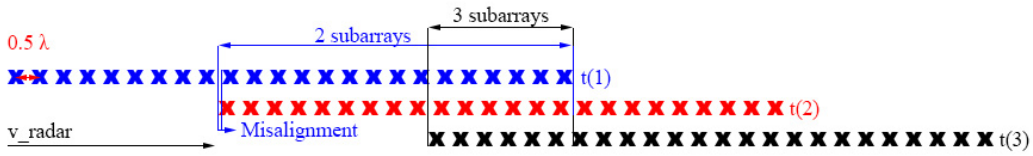

Figure 5.2: Example of DPCA for 3 time indices with 2 or 3 sub arrays

example of a radar consisting of 24 receivers at 3 different time indices. It shows that either two sub arrays of 15 or three sub arrays of 6 can be made. The sub array size can be written as.

$$s_a = L - \frac{v_{radar} nT}{d}. \tag{5.12}$$

Where L is the array size, n the amount of sub arrays, T the PRT and d is the interelement spacing. Equation 5.12 does not yield an integer for receiver elements. This misalignment disturbs the DPCA procedure. This is solved by interpolating the data of the receive channels of one array such that both are aligned. Note that more than s_a receiver channels in the sub array are used, the interpolation will fail. Using less is possible but this will increase the beam-width and thus increase clutter.
The channels can be combined after beam forming and misalignment interpolation as follows.

$$S_{DPCA2}(f, t_p) = S_{1a}(f, t_p) - S_2(f, t_p). \tag{5.13}$$

For 3 sub arrays this equation becomes,

$$S_{DPCA3}(f, t_p) = -S_{1a}(f, t_p) + 2S_2(f, t_p) - S_{2a}(f, t_p). \tag{5.14}$$

Where S_a indicates that this sub array is aligned with spatial interpolation.

5.4. ODPCA

As DPCA filters the stationary clutter, it is not very effective at the moving sea surface. Oceanic displaced phase centre antenna (ODPCA) [27] was developed to filter a Doppler frequency which is more apparent in the sea-Doppler distribution. A phase shift is applied to one of the sub arrays to shift the filtered frequency as.

$$S_{DPCA2}(f, t_p) = S_{1a}(f, t_p) - S_2(f, t_p) \exp(-j\theta). \tag{5.15}$$

For 3 sub arrays this equation becomes.

$$S_{DPCA3}(f, t_p) = -S_{1a}(f, t_p) + 2S_2(f, t_p) \exp(-j\theta) - S_{2a}(f, t_p). \tag{5.16}$$

Where θ is the added phase shift, if this is set to 0, regular DPCA is applied. Instead of estimating the local phase shift around the ship according to the sea state, image contrast maximization can be applied to find the optimal θ.

II

System Design

6

Motion Compensation

As the theoretical background necessary to develop an ISAR algorithm for multi channel SAR systems such as AMBER has been discussed, the optimal form of implementation can be researched. This chapter will compare the different motion compensation techniques and evaluate them based on several performance indicators. According to the results of this evaluation, while also considering previous research on ISAR algorithms in literature, a choice is made on how to implement motion compensation.

6.1. Simulation Setup

To get a good view on how the different algorithms perform and which are best suited to apply in AMBER, a simulation is set up for a performance analysis. During the setup of the simulation a distinction can be made between radar parameters, simulation parameters and motion parameters These will all be discussed briefly.

6.1.1. Parameters

Radar parameters The radar parameters are set to match AMBER to create a realistic scenario of how targets can be perceived. The used parameters are shown in table 6.1. For now, advanced effects such as nonlinearities, phase noise and idle-time are neglected.

Simulation parameters To generate an image which can create useful feedback on the motion compensation algorithms, simulation parameters are set such that imaging effects as smearing are clearly visible. This will give a better overview of the impact from changing motion parameters and motion compensation techniques. To achieve this, the radar will be simulated relatively close to the target.

While the simulation is performed in 3 dimensions, the target is simulated as a 2-D rectangle consistent of point scatterers. With 1 additional scatterer at the origin. An indication of how the point targets are spaced is shown in figure 6.1.

Some other important simulation parameters are listed in table 6.2. For now, white Gaussian noise is added to the demodulated signal to show the impact of noise on the signal.

Motion parameters The features of each individual simulated scatterer is derived from an available data-set. The data-set entails the motion parameters of a ship which is moving in a certain direction relative to the

Radar Parameters	
Fc	9.5 GHz
B	500 MHz
PRF	1 kHz
Fs	20 MHz

Table 6.1: AMBER simulation parameters

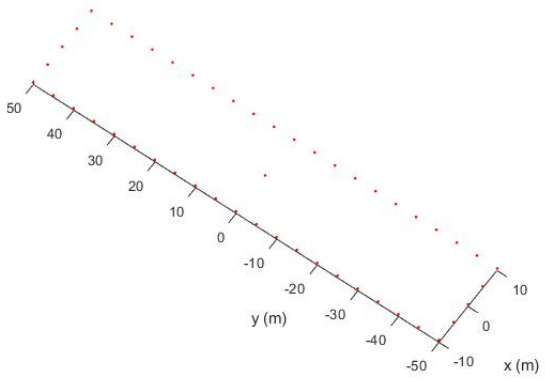

Figure 6.1: Point targets of the simulated 2-D rectangle

Simulation Parameters	
Target location	(0,0,0)m
Target velocity	10.28 m/s $\hat{y}$
Radar location	(500,-500,500)m
Radar velocity	-25 m/s $\hat{x}$
Simulation time	0.5 s
SNR	-5 dB

Table 6.2: Simulation parameters

sea-waves at a certain speed and sea state. This gives a realistic estimation of the motion from the scatterers. The set parameters for the simulation are given in table 6.3. The ship motion is set to be parallel to the sea motion, which results in a higher pitch and a lower yaw and roll. The sea state '5' on the Douglas sea state scale indicates a rough sea with waves between 2.5 and 4 m height.

6.1.2. Simulation Details

This section will provide a step-by-step overview of how the simulation is performed.

- Initialization of all parameters.
- The ship motion is loaded and interpolated to match the PRF of AMBER radar system.
- The ship center point is taken as (0,0,0) and remains at the center point of the axis in this simulation. The scatterer locations with respect to the center point are calculated over time dependent on the yaw, pitch and roll.
- The time dependent locations of the radar are calculated dependent on the radar starting location, motion of the radar and the motion of the ship. This means that the translational motion of the ship, along with the surge, sway and heave are incorporated in the translational motion of the radar.
- The time dependent ranges between the radar and each individual point scatterer are calculated.

Motion parameters	
Wave direction	$\hat{x}$
Ship direction	$\hat{y}$
Sea state	5

Table 6.3: Motion parameters

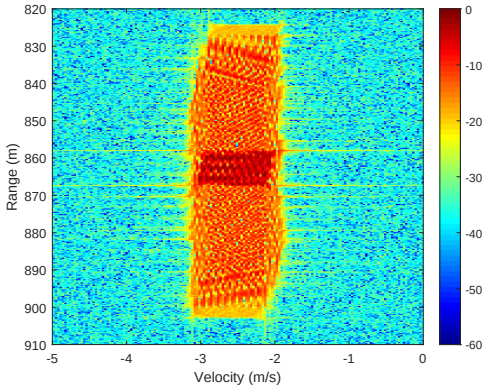

Figure 6.2: Range Doppler image after applying the RDA

- The retrieved demodulated signal is computed from the time-delays induced by the ranges. This also involves the radar cross section (RCS) of the point scatterers. Which are set to 1, except for the centre point scatterer which has an RCS of 5, which changes the final output power of each scatterer.

- An FFT is taken in range to convert to the range-time domain. The ranges containing the motion of the target are cut out of the complete image to save memory.

- Several range alignment and phase compensation methods were applied. These will be discussed in the next section.

6.2. Results

In this section several range alignment and phase compensation methods are discussed. It is followed by a small conclusion on the performance of the algorithms. But before ranking the algorithms, lets first consider why they are necessary by simply applying the RDA to the simulation setup as described in section 6.1. This results in the image as given in figure 6.2. This figure does not resemble the created target but looks more like a smear on its location. This is because each individual point scatterer is smeared in both range and Doppler as shown in figure 4.3. The small parallelogram with a higher SNR in the middle of the image comes from the single scatter at the center of the target which has an higher RCS than the others. Another interesting sight is that the target is located at a velocity of -2.5 m/s. This is due to the ambiguous velocity. Since the targets velocity with respect to the radar is higher than the unambiguous velocity, it is shifted through the spectrum.

6.2.1. Range Centroid

The range centroid method is applied as explained in section 4.3.1. The centroid for each vector is determined and with this the required bin shift for range alignment is performed. Figure 6.3 shows the computed range centroid bin location and the required bin shift. For the bin shift a Hampel filter is applied to remove outliers [28]. The figure shows that the linear displacement of the scatterer is clearly visible and can be retrieved.

To get an idea of the impact of the noise on this method, a second simulation is done with an SNR of -15dB. The results are shown in figure 6.4. It is clear that the range centroid method has difficulty in determining the center of the scatter cloud in a higher noise level. Although the general motion can theoretically still be retrieved by fitting the bin shifts on a linear line, the additional translational motions sway, heave and surge are lost.

After the vectors are shifted with the required bin shifts, an FFT can be taken in pulses to create an image in the range Doppler domain. The resulting image for the two different noise levels are shown in figure 6.5. The figures show that the smear in range is solved. But there still is a copy of the image as well as a smear in the Doppler domain. Both of these artefacts can in theory be solved by applying phase adjustment.

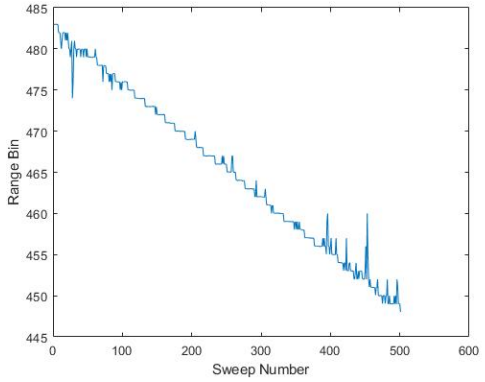

(a) Range centroid bin location

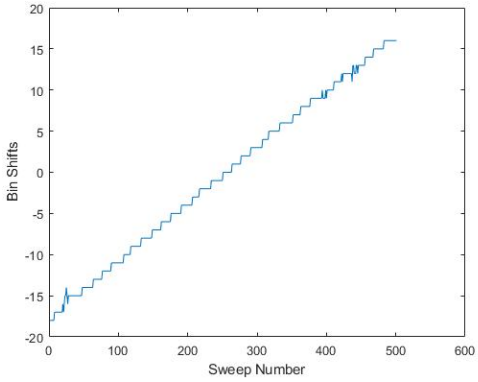

(b) Bin shifts performed per sweep

Figure 6.3: Range centroid method applied for an SNR of -5dB

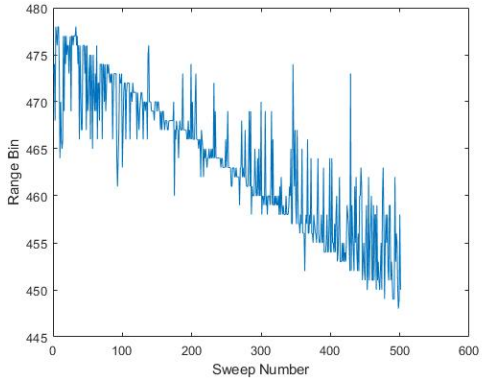

(a) Range centroid bin location

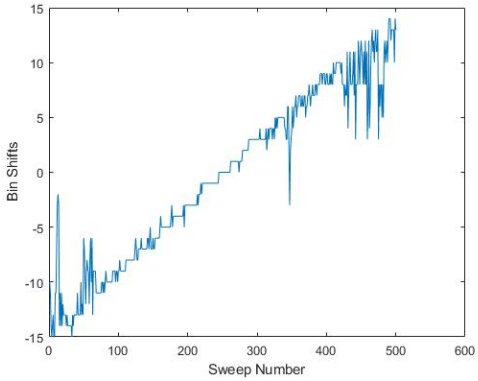

(b) Bin shifts performed per sweep

Figure 6.4: Range centroid method applied for an SNR of -15dB

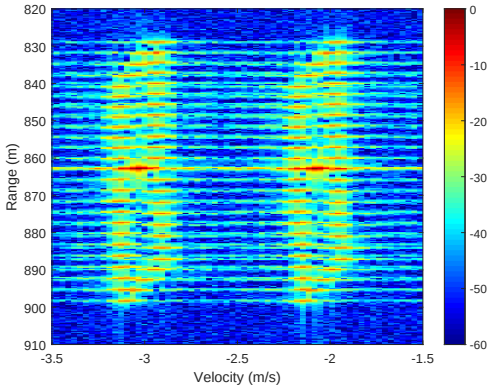

(a) SNR -5dB

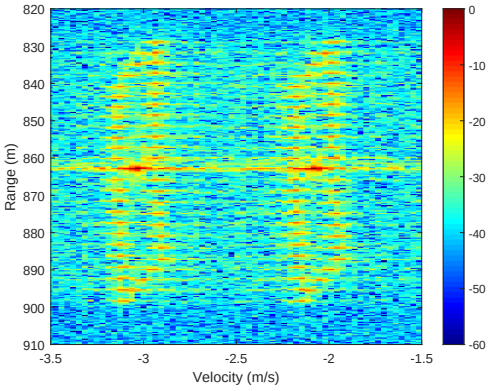

(b) SNR -15dB

Figure 6.5: Range Doppler images with the Range centroid method at an SNR of -5dB and -15dB

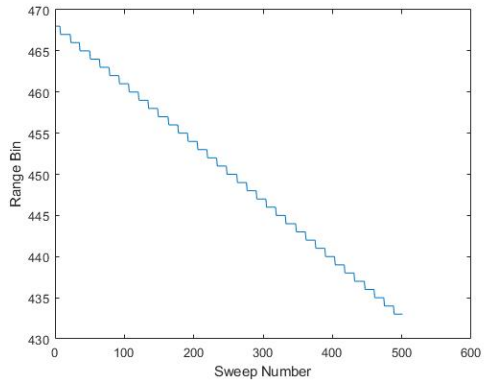

(a) Maximum bin per sweep at an SNR of -5dB

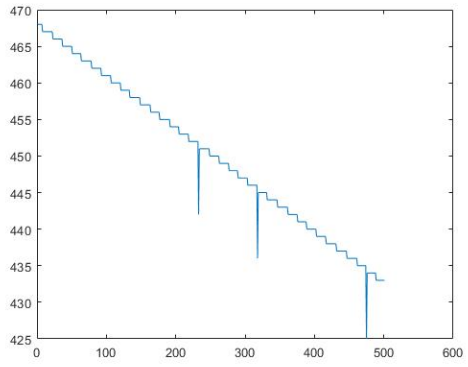

(b) Maximum bin per sweep at an SNR of -15dB

Figure 6.6: Determination of the required bin shifts for the cross-correlation method at SNR's of -5dB and -15dB

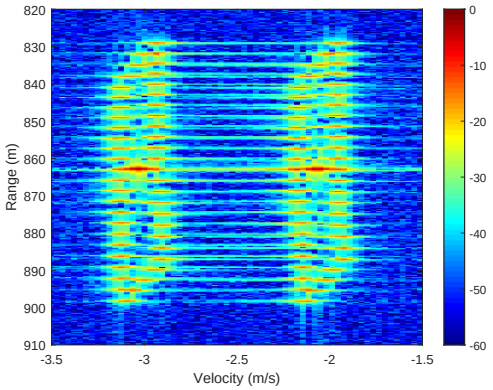

(a) SNR -5dB

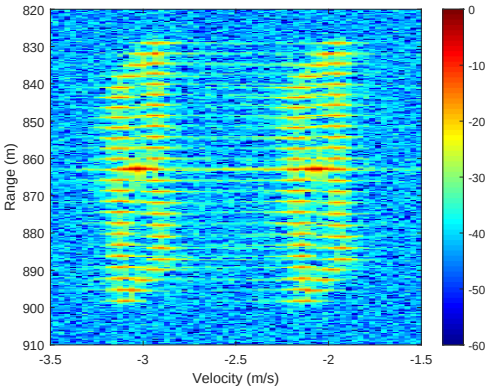

(b) SNR -15dB

Figure 6.7: Range Doppler images with the cross-correlation method at an SNR of -5dB and -15dB

6.2.2. Cross-Correlation Method

The Cross-correlation method is applied as explained in section 4.3.1. Here, the required range cell shift is determined with the cross-correlation. Just as for the range centroid method, figure 6.6 shows the estimated bin numbers for the -5dB SNR and -15dB SNR cases respectively. During the computation of the estimated bin shifts, a Hampel filter is applied in this case as well. Although for the cross-correlation method with these SNRs, the shift can almost be perfectly found and the filter is nearly unnecessary.

When considering the range Doppler image for both the SNR cases, the same replica of the target as in figure 6.5 is still apparent. However, due to the improved accuracy of estimating the bin shifts, the range Doppler image generated with the cross correlation method is better focussed. This is displayed in figure 6.7.

6.2.3. Minimum Variance Algorithm

The minimum variance algorithm can be applied on a range-time image where range alignment has already been applied. The range-time image produced by the cross correlation method is used since this yields better results.

In this setup, only a single minimum variance scatterer is used to create the phase compensation function. The minimum variance scatterer is found by determining the minimum variance over the normalized range-vectors. Figure 6.8 shows the unwrapped phase angle of the scatterer and the compensation function required to linearise the phase. The phase compensation function is then applied to all the range-vectors and an FFT in pulses is taken to create the range Doppler image.

The resulting range-Doppler image is shown in figure 6.9. The figure shows that the smears in Doppler are

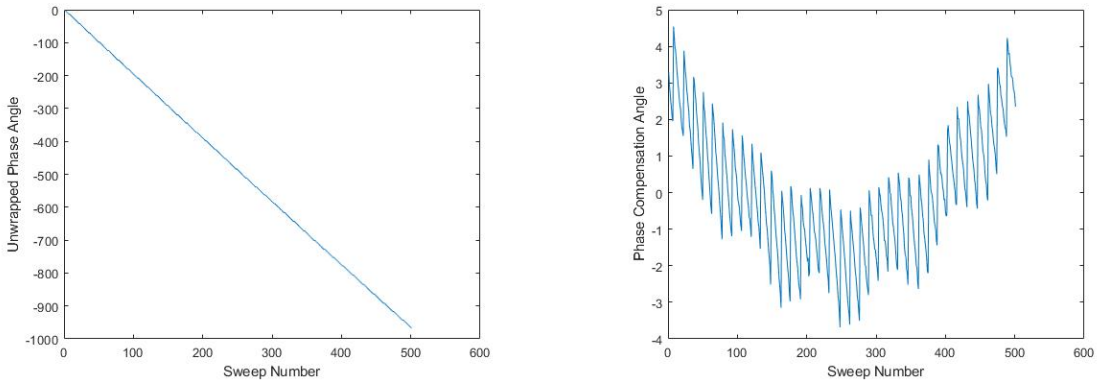

(a) Unwrapped phase angles

(b) Phase compensation function

Figure 6.8: Phases of the minimum variance scatterer before applying the MVA

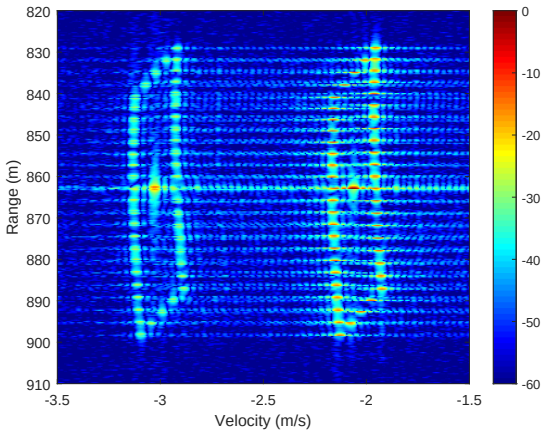

Figure 6.9: Range Doppler image after applying the MVA at an SNR of -5dB

solved nicely. However, the process has created an extra replica image of the target. Although the amplitudes of the replicas are lower than the actual target, more processing techniques need to be applied to resolve these copies.

6.2.4. Additional Approach

As the previous mentioned methods appear to work, but not ideally, some additional techniques are applied to improve the image quality. These techniques are based on the issue where the non-linear phase causes duplicates in the image. This non-linearity comes from the change in bin-shift. Two ideas to restore the linear phase change are proposed and evaluated in this section;

- Upsampling in time domain: As each point scatterer is located in a single range bin, upsampling in the time domain will spread the point scatterers over more bins. After the range adjustment, discontinuities only exist at the sides of the scatterer.
- Interpolation: An interpolation operation is applied to resolve the hard-cut in bins performed by the range alignment. This interpolation is applied after the upsampling procedure [11].

The techniques are applied and the results are shown in figure 6.10. The duplicates that showed in the previous sections have been completely removed and the resolution is improved significantly for both scenarios. Although the interpolated addition shows improvement in the smoothness of phases and amplitudes, this does not show any visible changes in the quality of the range Doppler image. The SNR increase that the interpolated addition gives on the upsampled signal is negligible when comparing it with the additional computational time this operation needs.

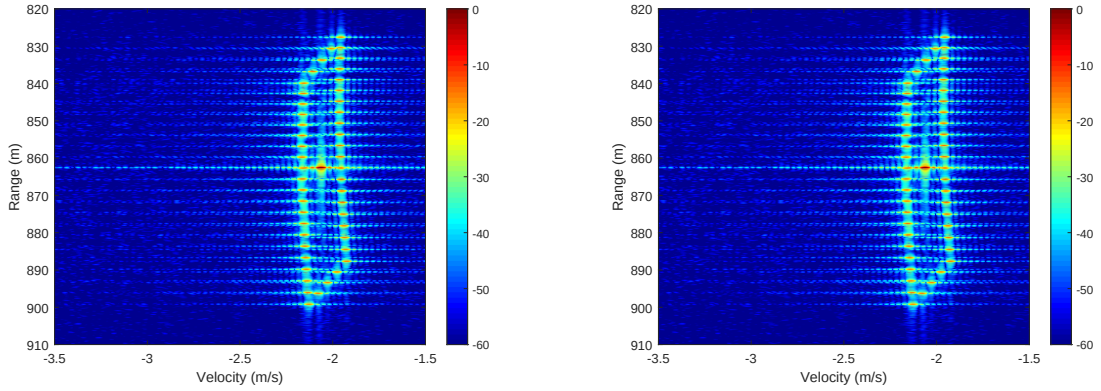

(a) Range Doppler image with upsampling, MVA and CC

(b) Range Doppler image with upsampling, interpolation, MVA and CC

Figure 6.10: Range-Doppler images after applying additional processing

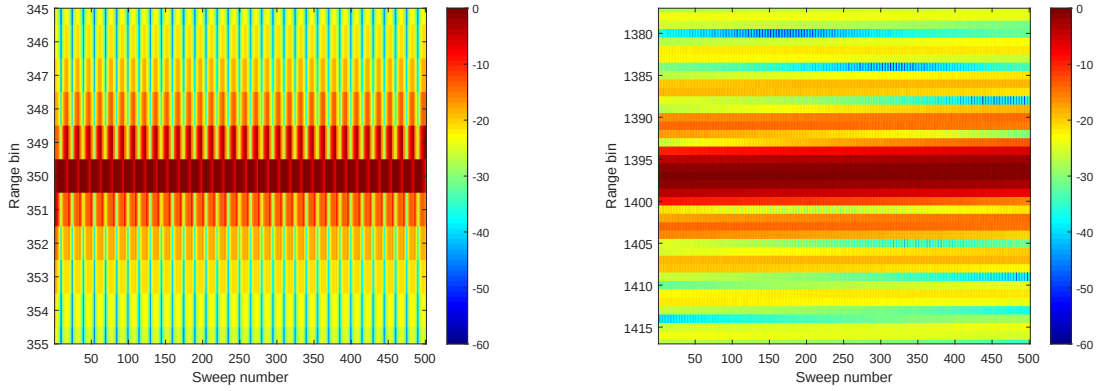

(a) The regular range-time signal

(b) Range-time signal after upsampling

Figure 6.11: Discontinuities are solved after applying upsampling to the time domain signal

To create a better understanding why these images do not have duplicates figure 6.11 shows a comparison between the regular signal and the upsampled signal. This figure shows that without upsampling there are discontinuities due to the bin shifts, which are resolved after the upsampling procedure.

6.3. Evaluation

Although all the mentioned techniques are capable of imaging the target of point scatterers effectively, there are some differences in terms of performance. To decide which algorithm is best suited to further build on, a performance analysis is performed on the different algorithms. Apart from the discussed methods above, two techniques which do not rely on range alignment and phase adjustment separately are also evaluated, backprojection and keystone formatting.

There are many known performance evaluation metrics, so it is important to choose an effective method for analysis [29]. For the evaluation of the different methods, three different parameters are considered:

- Point spread function (PSF)
- Peak to background ratio (PBR)
- Computation time.

6.3.1. Point Spread Function

The point spread function is widely used in radar and optical images for evaluating the response of a single point scatterer. For evaluating the PSF, two different scenarios are taken into account.

1 The target shows constant motion directly towards the radar

2 The target shows constant motion towards and tangential to the radar.

First, scenario 1 is considered. Figure 6.12 shows the PSF for 8 different scenarios. Each sub-figure is limited to the same range and velocity variance. Some interesting things about these spectra are noted and discussed below.

General observations One glance at figure 6.12 shows that there seems to be a displacement of the point scatterer in terms of range and velocity between the different algorithms. Within one coherent processing interval (CPI), the target occupies different ranges and velocities as seen in figure 6.12a. When this is converted to a single range and velocity, it can be anywhere within these boundaries as long as the relative location remains equal for different measurements, which is the case for all considered algorithms. Furthermore, when comparing the methods based on range alignment and phase adjustment with keystone formatting and backprojection, there is no difference in resolution.

Cross correlation and range centroid combined with minmium variance algorithm After applying the MVA, it can be seen that the replica of the point scatterer image is distorted. Since the range vector at exactly the point scatterers range is compensated for the phase, the replica is dissolved at this range. However, the side-lobes of the scatterer are not compensated and thus their replicas are still visible.

Zero padded and interpolated For both these functions the typical sinc function caused by the transform to the Fourier domain is clearly visible. There does not seem to be a difference between the two methods.

Keystone The keystone function is very well focussed, the target is visible in the exact center of the range Doppler response due to the 'keystone' like shape that the interpolation filter has.

Range Doppler backprojection The PSF of the backprojection does not show the typical sinc fall off from the point scatterer. The main reason is that there is that only in one dimension the FFT is applied.

Lets now consider the second scenario, this shows changes for keystone formatting and backprojection. Consider the RDA response in figure 6.13. Since the target has a tangential velocity component, the change in range is not linear, the target has an accelerating motion with respect to the radar. Since in both keystone as in backprojection it is assumed that the Doppler is coupled linearly with range, the point spread function is smeared in Doppler. For both these functions, this smear can be compensated if the acceleration parameter is known. Which is shown in the figure as well for the keystone transform. Here IC maximization is applied to estimate the relative acceleration parameter of the target.

6.3.2. Computational Time

A second important performance measurement is done on the computational time. Table 6.4 shows the computational time for the different algorithms for generating the range Doppler image. Note that this measurement is not performed on the final hardware, and is only a comparative method to determine the difference in speed of the different algorithms.

The table shows a typical relation, more accuracy requires more computational resources. Keystone formatting and backprojection both appear to be relatively slow compared to the other algorithms. Note that at this stage the regular keystone transform is applied. Different methods on how to improve the processing speed of this algorithm are known and will be mentioned later.

6.3.3. Peak to Background Ratio

For the final evaluation metric the peak to background ratio is used. In figure 6.14 the different TMC methods are plotted based on their peak to background ratio versus the SNR. White Gaussian noise is added to the time domain signal to test the performance of the algorithms under more noise. The peak to background ratio which is used is defined as,

$$PBR = \frac{\max|\mathbf{S}|}{|\bar{\mathbf{S}}|}. \tag{6.1}$$

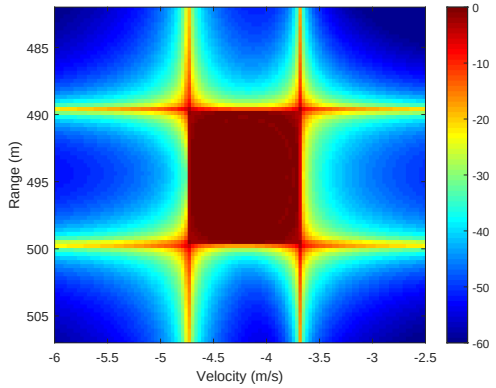

(a) Range Doppler algorithm

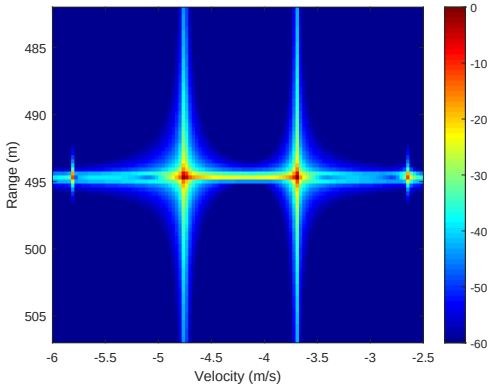

(b) Cross-correlation

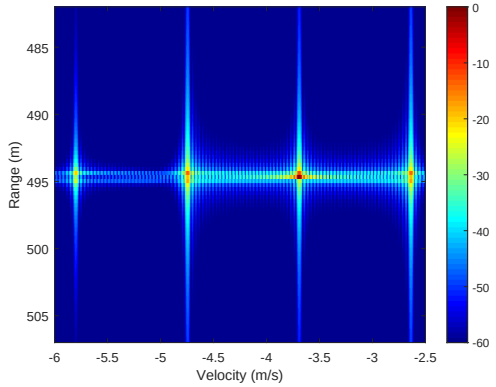

(c) Cross-correlation with minimum variance

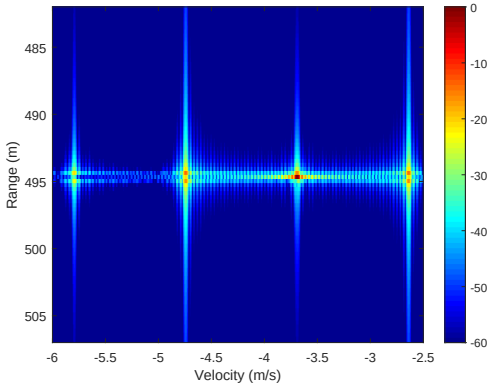

(d) Range centroid with minimum variance

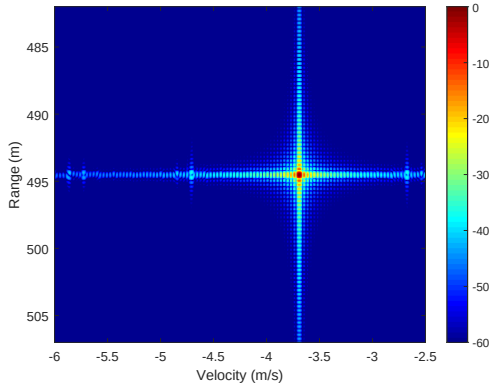

(e) Zero padded

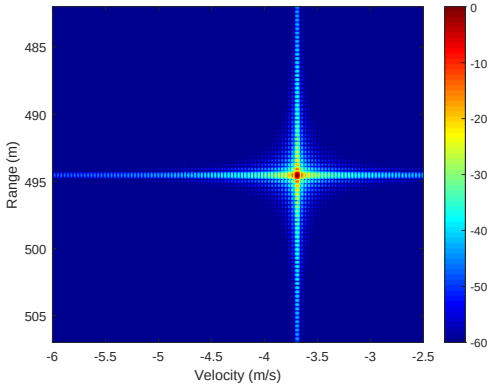

(f) Interpolated

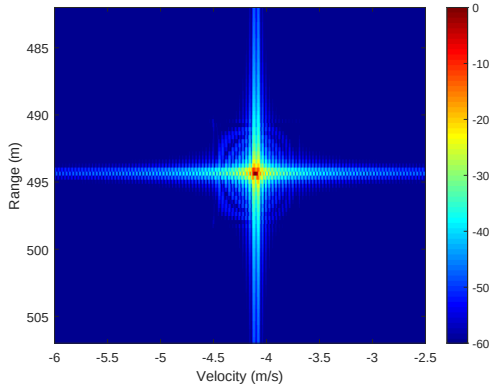

(g) Keystone

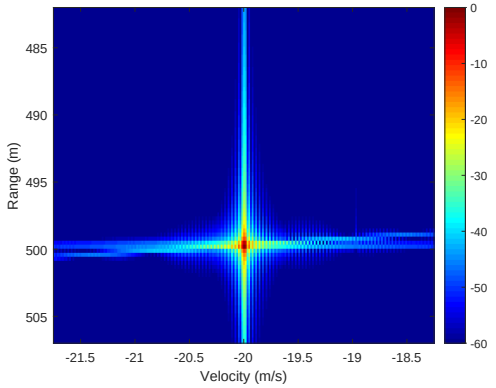

(h) Backprojection

Figure 6.12: Point spread functions without tangential velocity component

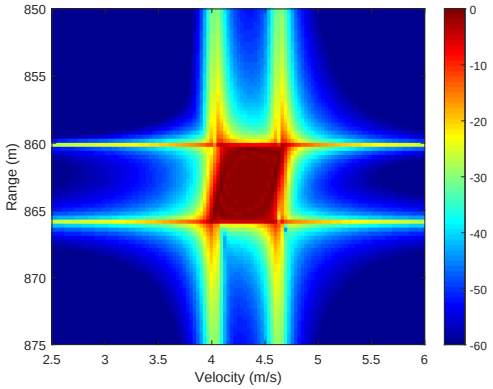

(a) Range Doppler algorithm

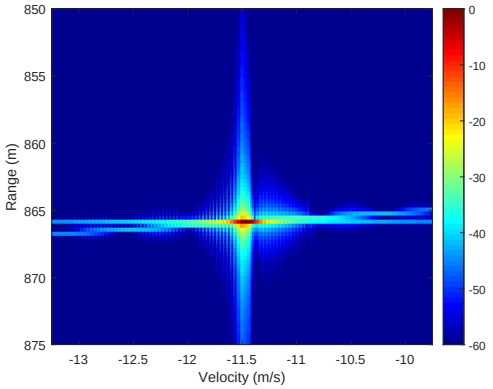

(b) Backprojection

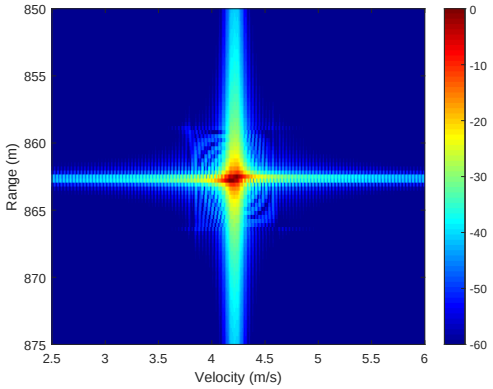

(c) Keystone

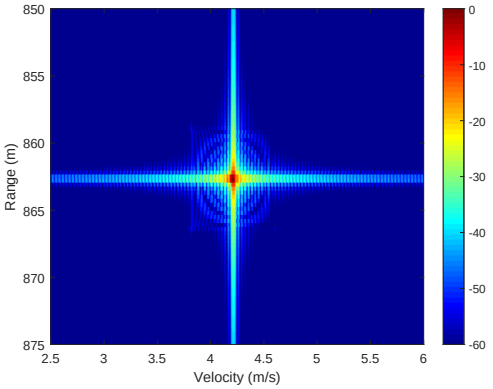

(d) Keystone with image contrast maximization

Figure 6.13: Point spread functions with tangential velocity component

Algorithm	Computational time
RD	0.018s
CC	1.19s
RC	0.602s
RC MVA	0.932
CC MVA	1.466s
CC MVA upsampled	3.550s
CC MVA upsampled and interpolated	3.7160s
Keystone	15.39s
Backprojection	36.56s

Table 6.4: Computational times for different TMC algorithms

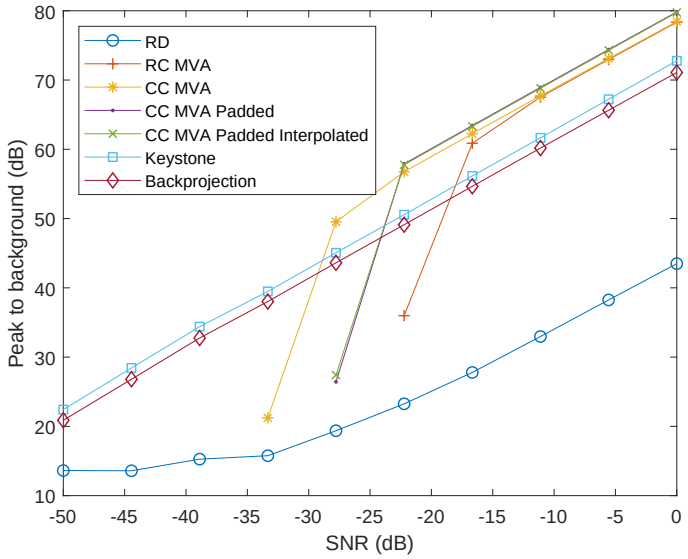

Figure 6.14: Peak to background ratio's for different methods

	Computational time	PBR	PSF
CC MVA Padded	++	++	++
Keystone	+-	+	++
Backprojection	-	+	++

Table 6.5: Performance indication of different TMC algorithms for measurements without tangential velocity components

Where **S** is the matrix under consideration. Figure 6.14 shows that the methods based on separate range alignment and phase adjustment (RC and CC) have a higher accuracy, but tend to fail when more noise is applied. Still they give a higher peak to background ratio then the Range-Doppler algorithm at higher noise. This happens since the MVA forces a range vector to a linear phase. Which will always create a bright spot in the range-Doppler spectrum, since this range-vector will have only 1 velocity component. However, the location of this response is wrong and the algorithms are unable to distinguish multiple targets.

The range Doppler algorithm also fails at the -35dB SNR mark. At this point and below, the Peak to background ratio is just an indication of the variance of the noise in the image.

Both keystone formatting as backprojection appear to work at extreme high levels of noise. Where keystone has a slightly higher peak to background ratio as backprojection.

6.4. Conclusion

Since only 1 algorithm can be implemented, this section summarizes the performance evaluation and decides what the best algorithm is to move forward with. The range Doppler algorithm and range centroid method are left out of this evaluation since they clearly performed worse than the others. The 3 remaining algorithms are CC with MVA and zero padding, keystone formatting and backprojection. Table 6.5 generalizes the findings on these algorithms in the previous sections.

If this table were conclusive it would be clear that applying the first method is best. However, due to two important discussion points, keystone formatting with IC maximization is chosen as the best approach.

- The keystone transform takes a lot more time to compute than the first method. This is due to the interpolation that is done on the complete image. This interpolation can however be done in a different manner after applying a Fourier transform, which will significantly improve the speed of the algorithm [30]. Another approach is to apply the keystone transform over a range-cropped part of the data.
- How the keystone transform is applied does not depend on the received signal itself as with the other

methods, but is an adjustment based on the properties of the transmitted signal. This is also the reason that it still performs accurately while under severe noise. Which is a very important feature when measuring targets at large distances which suffer from high propagation losses.

7

Clutter Suppression

As discussed in the previous chapter, keystone formatting combined with image contrast maximization is the best method for motion compensation in this particular implementation. This chapter discusses some additional options for exploiting the multichannel receive array, apart from the methods discussed in the chapter 5. Evaluating these beam forming techniques is done with real measured data. A snapshot of the measurement location with the targets is shown in appendix G. As the exact location of targets in the measured data was unknown, several pre-processing steps were taken before the imaging procedures. These can be found in appendix C. Furthermore, an overview of the advantage of effectively applying motion compensation and adding more receivers with regular beam forming can be found in appendix E.

7.1. Multichannel Assets

The use of multiple receivers in an ISAR imaging system is advantageous regardless of the higher computational load that it gives. This section discusses some ideas of how DBF can be used as an advantage to create sharper images.

7.1.1. Dual Array DBF

Due to the 24-channel receive array, the received beam is narrowly focussed to only several degrees. However, preferably the side-lobes would be at a lower level, since a different target could reside in one of them. The side-lobes can be lowered by windowing or weighting functions such as the Dolph-Tchebyschev distribution [31].

In this section an alternative method is proposed. The 24-channel receive array is used to steer 2 different beams, both containing the 24 receivers, close to the θ which contains a target, such that the nulls of first beam will cancel the peaks of the second, and vice versa. Consider the first null right to the first beam and the first secondary peak left to the second beam;

$$\theta_{n1} = \arccos\left(\frac{1}{kd}\left(-\beta_1 - \frac{2}{N}\pi\right)\right), \tag{7.1}$$

$$\theta_{m1} = \arccos\left(\frac{1}{kd}\left(-\beta_2 + \frac{3}{N}\pi\right)\right). \tag{7.2}$$

Now consider $\theta_{n1} = \theta_{m1}$, such that;

$$-\beta_1 - \frac{2}{N}\pi = -\beta_2 + \frac{3}{N}\pi. \tag{7.3}$$

Where $\beta_1 = \beta + \beta_s$ and $\beta_2 = \beta - \beta_s$. This yields;

$$\beta_s = \frac{\pi}{2N}. \tag{7.4}$$

The results of applying peak-null cancellation for a dual array are shown in figure 7.1. It evidently shows that the side-lobes are suppressed at the cost of a small widening of the main beam. Whether this approach is effective is strongly correlated with the location and power of interfering signals.

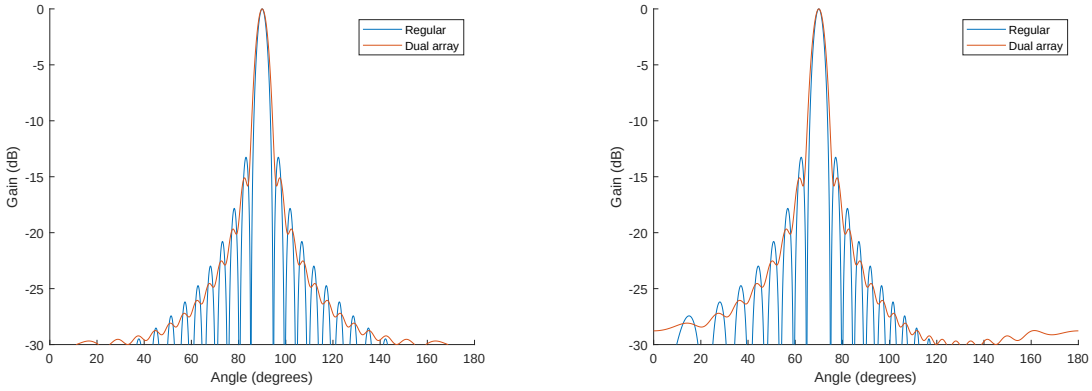

(a) 0 degrees from normal on antenna receiver array

(b) 20 degrees from normal on antenna receiver array

Figure 7.1: Beam-forming with peak-null cancellation applied for the 24-channel receive channel for different incident angles

7.1.2. IDPCA

This section proposes an alternative on the known DPCA methods, the inverse displaced phase centre antenna (IDPCA) method. The general idea can be described by the following steps;

- The array is split up in 2 or more sub arrays
- The sub arrays are aligned by spatial interpolation in the sensor direction such that their measurement-locations coincide.
- DBF and motion compensation are applied on each individual sub array.
- The strongest scatterer is determined in the range - slow time domain. The phase difference between the sub array of the concerned scatterer bin is calculated.
- The calculated phase shift is added to one of the sub arrays.
- As of now both sub arrays show the target in the same location and phase, they are summed.

Apart from the theoretical positive prospects of suppressing clutter, this theory has some drawbacks. First of all, imaging is done with a sub array, decreasing the angular resolution and thereby decreasing clutter suppression. Second is the increase in computational load of the algorithm. Whether the suppression of clutter will be higher than the rising of clutter will be determined in practice in section 7.2.

7.1.3. Sparse Target Tracking

Using successive measurements to increase the image quality is another method which can rely on DBF. Using the sparse measurements combined with the AOA technique, the course of targets can be tracked over time. Considering that the platform motion is known, this technique can retrieve the ship motion in terms of direction, velocity and acceleration. These parameters can be used to make a good initial estimate for finding the optimal acceleration parameter, cutting down the computational load. This technique mimics spotlight data collection in SAR by using DBF.

7.2. Evaluation

This section discusses the impact of applying OCPDA, IDPCA and MVDR to the imaging procedure. Each of these techniques will be applied on real measured data. In the evaluation two targets in appendix G are considered, target A and target C. Target A is isolated and is only disturbed by sea clutter, while target C is very close to target D, disturbing the image.

7.2.1. ODPCA

A sweep on the phase shift θ is performed from $-\pi$ to π. The relation between θ and the image contrast is shown in figure 7.2. The figure shows that there is an optimal point in terms of phase shift to place the DPCA clutter suppression. The minimum in the figure shows with which phase shift a null is placed on the target

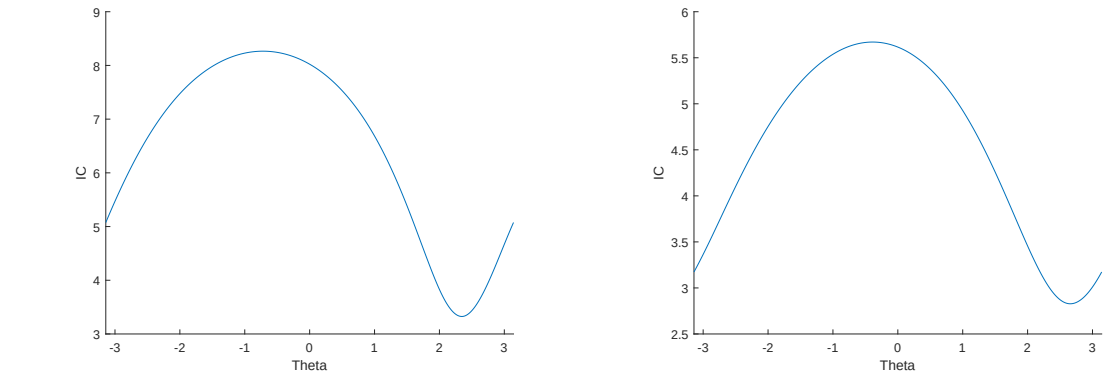

(a) Target A, two sub arrays

(b) Target A, three sub arrays

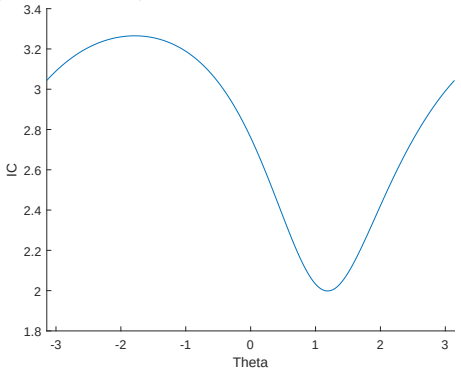

(c) Target C, two sub arrays

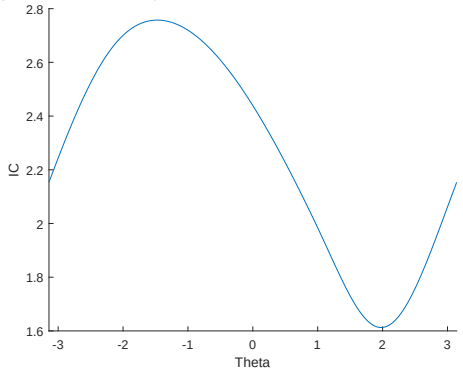

(d) Target C, three sub arrays

Figure 7.2: Image contrast function versus ODPCA angle for different sub array sizes and targets

itself.
That the peak for the two sub arrays does not align with the peak of three sub arrays, is possibly due to the wider beam created by the 6 channels, giving the possibility for different clutter components. However, why the minima of of the different sub arrays do not align is uncertain.
Furthermore, it is noted that the IC measured with three sub arrays in considerably lower than the IC where two sub arrays are used. This may be caused by the fact that with three sub arrays of 6 overlapping receivers, there is a total of 6 antenna elements that are never used since they do not fall within the sub array slot (three elements left and three elements right of the sub array considered in t(2) in figure 5.2). The resulting ISAR images generated by the ODPCA method are shown in figure 7.3

7.2.2. IDPCA

In stead of subtracting sub arrays from each other which removes objects that are stationary, a new technique is proposed where the opposite is performed. Since motion compensation is done before the combining of sub arrays, the target can be seen as a stationary object. Now the sub arrays are added instead of subtracted. Which is in some way similar to coherent summation. Note that some assumptions are made within this process.

- The targets motion between sweeps is assumed to be similar for all its scatterers.
- The sea surface is expected to show different motion between sweeps.

Consider the two different sub arrays after motion compensation. Their range - slow time plots for the first target are shown in figure 7.4. As both the target and the radar move over time, the phase of the strongest scatterer of both these range - slow time figures are not the same.

When considering the scatterer which shows the minimum variance over sweeps, the phase angle for both the sub arrays is measured. As figure 7.5 shows, the phase angle for both sub arrays is different, as expected.

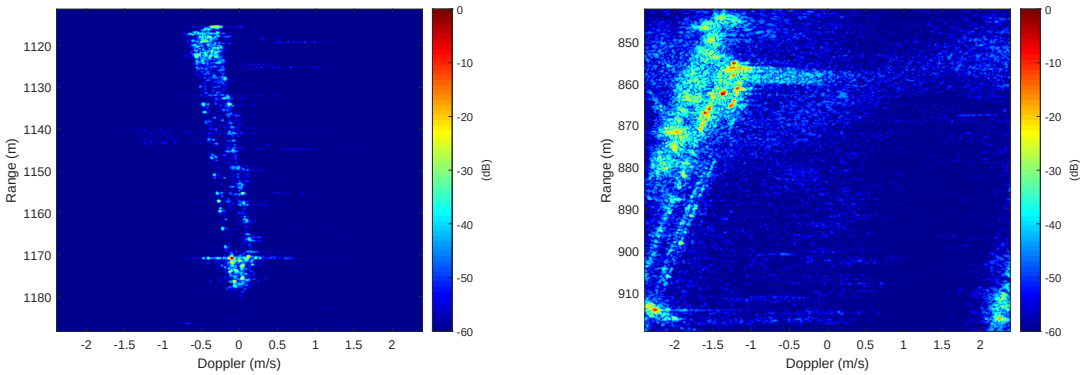

(a) Target A

(b) Target C

Figure 7.3: Range Doppler images of the two considered targets after applying ODPCA

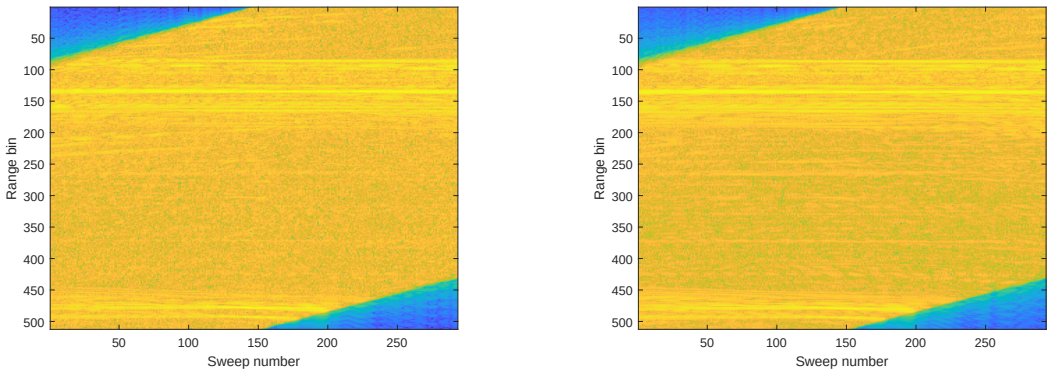

(a) Sub array 1

(b) Sub array 2

Figure 7.4: Range - slow time plots for two different sub arrays in IDPCA after motion compensation

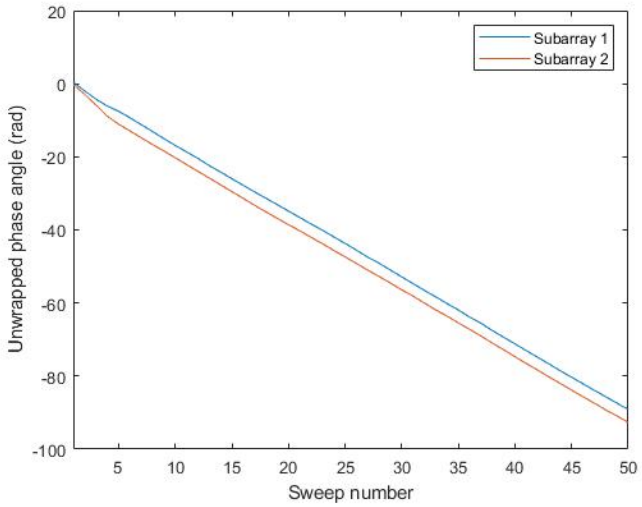

Figure 7.5: Unwrapped phase angle for the scatterer with minimum variance in both sub arrays of IDPCA

The phase angle between the two sub arrays is described as;

$$\phi_c = \angle(S_1[t_{n-min}, t_p]) - \angle(S_2[t_{n-min}, t_p]). \tag{7.5}$$

Where S_1 and S_2 are the range - slow time data for both the sub arrays and t_{n-min} is the range bin which shows the minimum variance. In practice, this phase shift ϕ_c is smoothed to remove outliers, which must be errors since the ship's motion approximately continuous. This phase difference is applied to S_2 to match its phase to S_1 as;

$$S_m(t_f, t_p) = S_2(t_f, t_p)\exp(i\phi_c). \tag{7.6}$$

Which is then as a final step added to the first sub array.

$$S_{IDPCA}(t_f, t_p) = S_m(t_f, t_p) + S_1(t_f, t_p). \tag{7.7}$$

Adding an additional phase to one of the sub arrays as done in ODPCA is useless, since this phase will be corrected in the phase alignment stage, yielding the exact same results. Applying IDPCA on two sub arrays gives results on the IC as;

$$IC_A = 8.2864.$$

$$IC_C = 3.5311.$$

Which is for both cases slightly above the optimal case in ODPCA. The images generated by this process are shown in figure 7.6

7.2.3. MVDR

The MVDR averages the output power of all directions that are not the AOA. This very idea is contradictory with the IC. As this function favours high peaks and nulls. The calculated IC for both targets while applying MVDR is;

$$IC_A = 3.7361.$$

$$IC_C = 2.7497.$$

Which is especially a significant drop for target A. To get a different perspective of what is going on, the range Doppler images of both MVDR processed targets are compared to the regular processed images (as also seen in figure E.5), which is shown in figure 7.7.
The image shows that the MVDR processing removes strong secundary scatterers from different directions at the cost of a higher overall background power. This is exceptionally visible in the case of target C. Here, a second ship appears in the same range bins as the target, but on a different AOA. The MVDR minimizes the variance over all angles that are not the AOA of the target, thereby attenuating the power of the clutter.

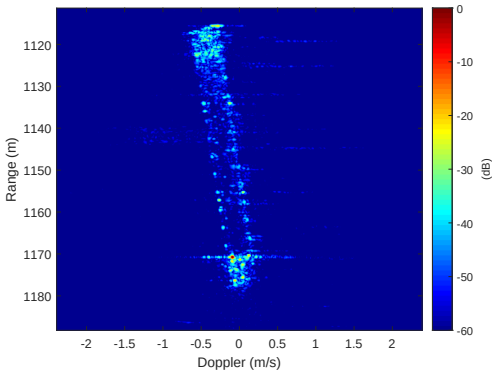

(a) Target A

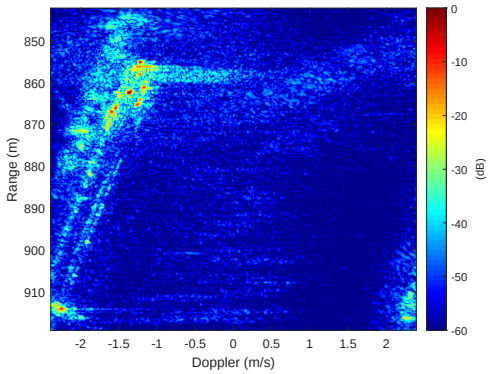

(b) Target C

Figure 7.6: Range Doppler images of the two considered targets after applying IDPCA

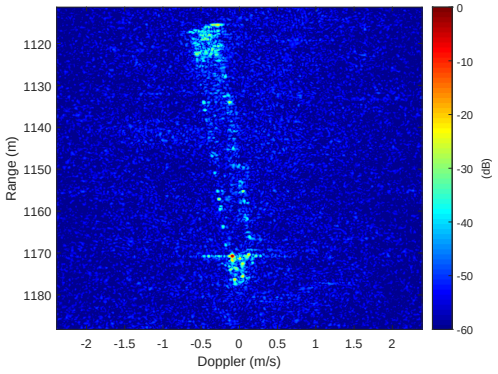

(a) Target A, MVDR

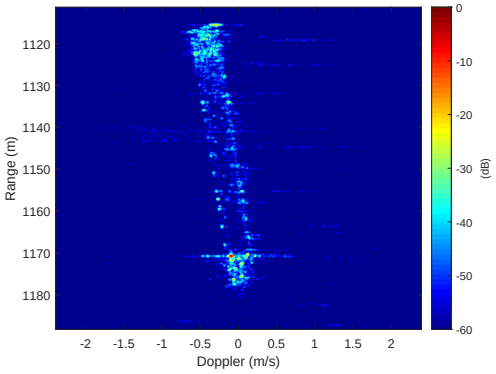

(b) Target A, regular DBF

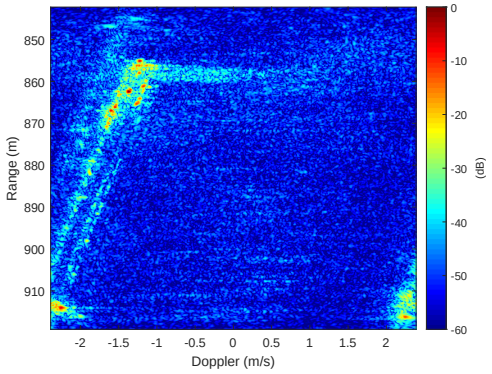

(c) Target C, MVDR

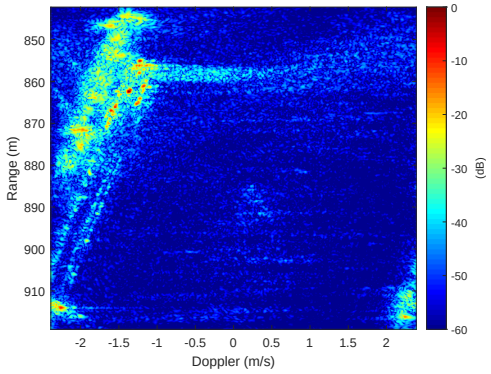

(d) Target C, regular DBF

Figure 7.7: Comparison for the two targets of imaging with MVDR versus imaging with regular DBF

7.3. Conclusion

This chapter discusses the performance of several known methods which suppress clutter. An alternative method which suppresses clutter based on the motion of the target is proposed and is referenced to as IDPCA. The evaluation is performed on real measured data. The ODPCA and IDPCA show improved results compared to regular beam forming according to the image contrast of images. The MVDR shows good imaging results, but its image contrast decreases. In the next chapter, the DPCA methods will be researched for possible extensions and improvements. It should be determined if and how these methods can be combined with the MVDR. Based on the research done so far, a consideration of different possible design methods for the final algorithm was performed. The considerations and conclusions of the different design methods are presented in appendix D.

8

System Optimization

As the different clutter suppression methods, ODPCA and MVDR both show advantages in different areas, some type of optimization is required. In this chapter an attempt is made to find the optimal way in how to combine the methods with each other, based on newly defined performance indicators. Based on this research, a new, innovative method is proposed on how clutter can be suppressed.

8.1. Performance Indicators

PTC The peak to clutter (PTC) ratio will give a clear indication of the difference in suppression of clutter between different clutter suppression methods. The PTC is calculated as the maximum value divided by the mean of the clutter region;

$$PTC = \frac{\max|S|}{\langle|S(C)|\rangle}. \tag{8.1}$$

PTB As previously shown the signal power contained in the background appeared to rise when applying the MVDR. Thus is measuring the peak to background (PTB) ratio a very good performance indicator for clutter suppression methods. The PTB is calculated in a similar way as the PTC, but only on a background region in stead of a clutter region.

$$PTB = \frac{\max|S|}{\langle|S(B)|\rangle}. \tag{8.2}$$

PTT Some of the techniques which are used may apply procedures which alter the overall quality of the target. The target may still be focussed at one singular point, but could be attenuated at a different location. For this issue the peak to target (PTT) indicator is introduced. Where the difference in power between the maxima and a different area on the target is measured. The PTT is defined as,

$$PTT = \frac{\max|S|}{\langle|S(T)|\rangle}. \tag{8.3}$$

The performance evaluation will be performed on a range Doppler image which clearly contains clutter in an unfortunate location. The clutter, background and target region are manually selected and remain the same for each different evaluation. The different regions considered in the range Doppler image are shown in figure 8.1.

The performance progress achieved so far according to the used algorithms can be found in table 8.1.

	PTC	PTB	PTT
1 receiver	13.49	27.88	16.15
8 receivers	13.25	35.88	14.04
16 receivers	13.76	37.56	13.27
24 receivers	15.00	37.82	14.37
Foldover correction	27.48	49.00	17.35
Keystone	28.43	48.67	17.20
Acceleration compensation	38.21	60.93	21.53
MVDR	47.01	56.22	20.85
ODPCA 2 subarays	40.16	61.20	22.10
ODPCA 3 sub arrays	25.29	56.30	27.04
IDPCA	40.54	61.36	22.02

Table 8.1: Performance improvements of the ISAR image for different subcomponents of the imaging procedure concerning a singular target, for PTC and PTB higher values show an increased performance. For PTT, a higher value shows a decrease in performance.

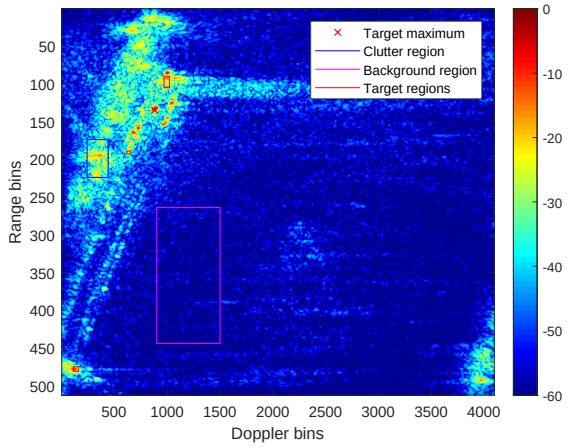

Figure 8.1: Indicated the used measurement regions to compute performance indicators PTC, PTB and PTT

8.2. Sub Array Division Methods

As IDPCA is a method which can be applied when there are multiple range Doppler images available, there are quite some possibilities on where to apply this algorithm. In this section possible combinations and adaptations of ODPCA and IDPCA are discussed.

8.2.1. Stacked Sub Array Combining (SSC)

In section 5.3 was discussed that dependent on the receiver array size and radar velocity, different sub array sizes can be chosen for DPCA. In the example image in particular, either 2 sub arrays of 15 receivers are used or 3 sub arrays of 6 receivers. These two options both have a good image quality. Stacked sub array combining is aimed to combine the 2 results, to increase the quality even more. The procedure on how to combine the results is the same as in IDPCA. In this particular case, only 2 different sub array sizes can be combined. However, if the radar moves with a lower velocity, more variations are possible. The combination of the sub arrays can be done with or without adding the single sub array with MVDR, a flow chart of the process is shown in figure 8.2.

8.2.2. Variable Array Shift (VAS)

The combining of sub arrays in DPCA and ODPCA is limited as both sub arrays need to be of equall size. However, for IDPCA it is not necessarily obligated to use arrays with similar sizes. This approach could be extra beneficial when nulls and secondary maxima of the different sub arrays align. The technique can be applied to any number of different sub arrays possible within the amount of receivers. An overview of how this method can be applied in practice with the maximum number of sub arrays used is displayed in figure 8.3.

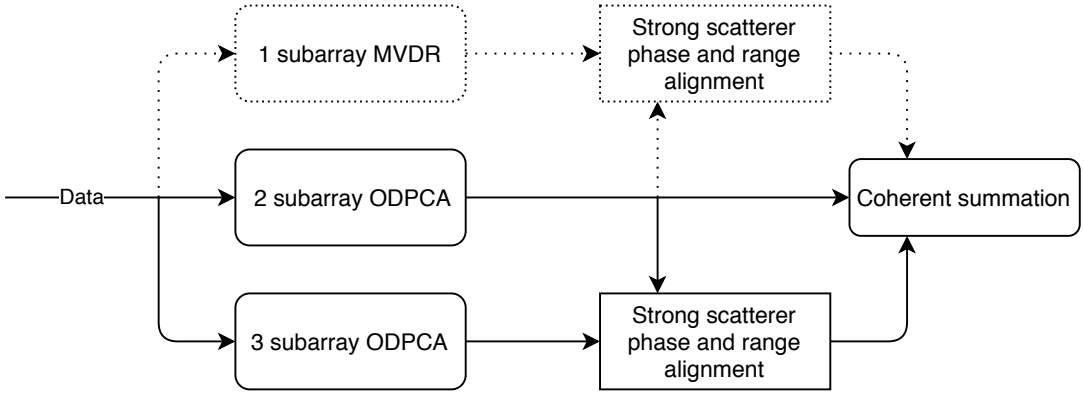

Figure 8.2: Flow chart of stacked sub array combining

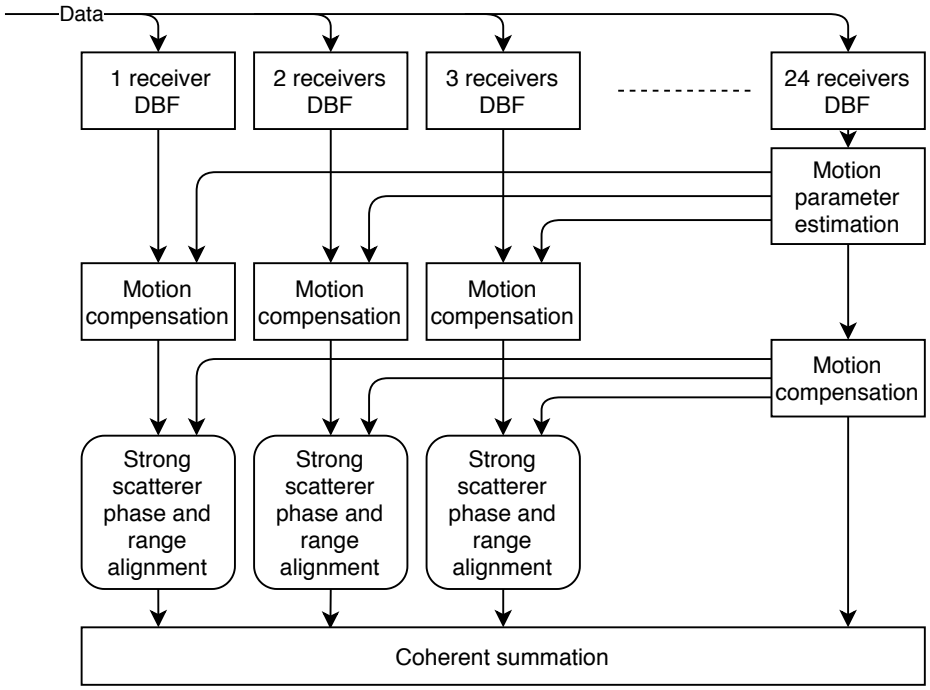

Figure 8.3: Flow chart of variable array shift

Note that this technique is applied within one sweep of the measured data. The motion parameter estimation is done with the data which contains the maximum amount of receivers. This ensures the highest accuracy of motion parameters. The compensation of all the different sub arrays is done based on the same estimated parameters.

8.2.3. Static Array Shift (SAS)

Instead of combining sub arrays of different sizes, all sub arrays of the same size can be combined in al possible sizes. Just as in variable sub array combining, this technique is applied within one sweep of the measured data. An example for a receiver array of 12 receivers with a sub array size of 7 is shown in figure 8.4.

8.2.4. Time Delayed Image Combining (TDIC)

The previous methods depend on variations which are created within one or two sweeps. This method was devised with the intent to create a larger variation of the target motion between the different measurements. The comparison in this case is made between different slow-time delayed versions of the image.
As an example, consider a measurement consisting of 400 sweeps. The 400 sweeps are split up in different signals being: sweep 1:300, sweep 50:350 and sweep 100:400. Each of these signals is then processed, range

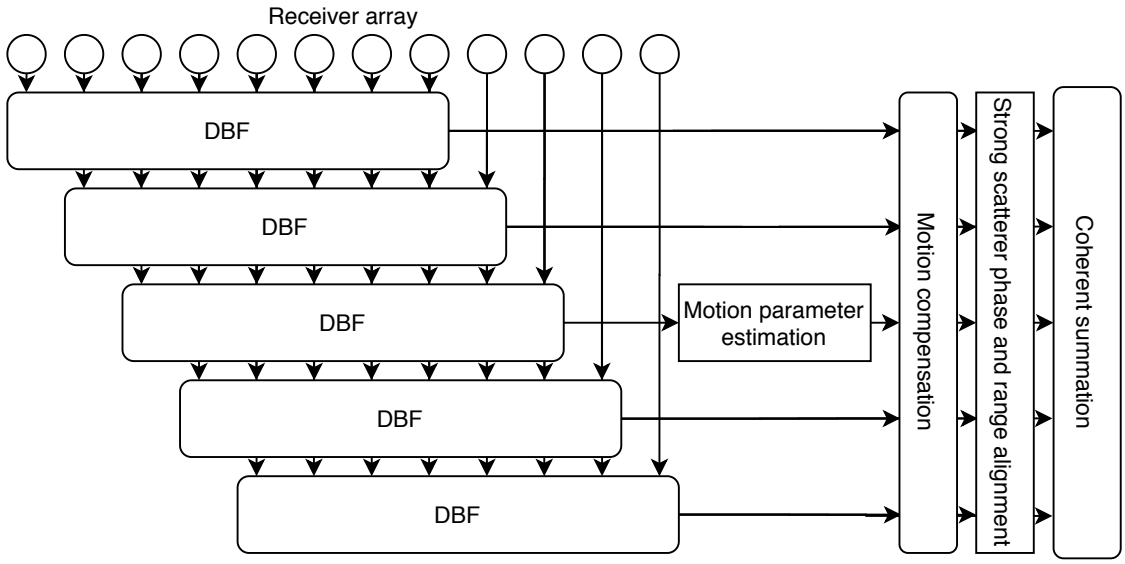

Figure 8.4: Flow chart of static array shift

and phase aligned and finally summed coherently.

8.3. Exploiting Coherent Summation

Coherent summation is an effective method to amplify the signal strength of the target. However, the maximum gain is limited. Suppressing clutter which exceeds the target in power for several decibels is impossible with regularly applied coherent summation.

8.3.1. Adaptive Coherent Summation

As the range Doppler images are summed coherently and shown in absolute values some important information is lost. Due to the appliance of IDPCA, the phases of a motion compensated target in the range Doppler domain, have become similar for the different generated and range aligned images. Coherent summation exploits this, but it is possible to let the phase differences have a bigger impact. The new proposed coherent summation scheme which will be used in the following sections can be described in a few steps.

- According to the clutter suppression method, a number of range - slow time arrays are aligned in range and phase according to the strongest scatterer
- On each range - slow time array a Fourier transform is applied to convert it to the range Doppler domain.
- The phases of all components in the new 3D data matrix are computed.
- The circular variance of the phases is calculated for each individual pixel in the range Doppler image.
- A 2-dimensional moving average filter is applied to the variance-matrix to smooth the images and filter errors caused by overlapping clutter and multipath.
- The minimum is subtracted of the matrix to set the minimum to zero and keep coherence between different clutter suppression techniques.
- The new variance-matrix is used to adjust the ISAR image output according to a filter.

A simple flowchart of the scheme is shown in figure 8.5. To compare the different clutter suppression methods discussed in this section, a test-filter is set fixed. The optimization of the filter will be done based

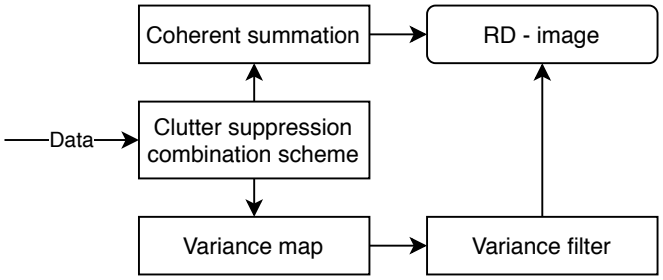

Figure 8.5: Flowchart of the adaptive coherent summation scheme

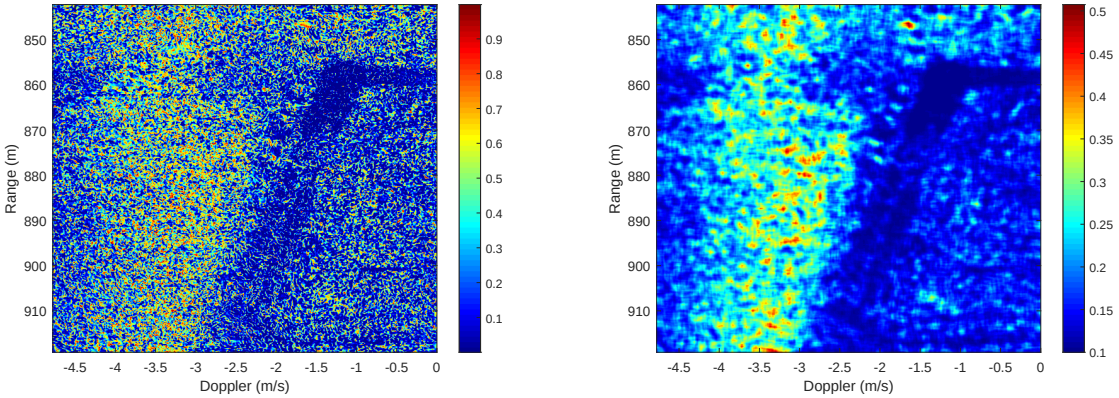

(a) Variance of all pixels in the range Doppler image of a target

(b) Variance filter, denominator in equation 8.4

Figure 8.6: Variance map of a target before and after moving average procedure

on which clutter suppression method proves to be most effective. The ISAR image generated in the following sections will be computed as,

$$\boldsymbol{S_I}(R, f_d) = \frac{\sum_{n=1}^{N} \boldsymbol{S_n}(R, f_d)}{N(\beta + \mathrm{Var}_c(\angle \boldsymbol{S}(R, f_d))^2)}. \tag{8.4}$$

Where S is a 3D matrix containing N range Doppler images. The $+\beta$ in the denominator is necessary to avoid division by zero and is set to $\beta = 0.1$ in the test filter. An example of the variance filter is shown in figure 8.6. It is not possible to compute the regular variance over the phases, as phases are discontinuous. Thus the circular variance is applied in this case. [32] Given a set of K vectors, the circular variance is defined as,

$$\mathrm{Var}_c = 1 - \left| \frac{1}{K} \sum_{k=1}^{K} \frac{\boldsymbol{v}_k}{|\boldsymbol{v}|} \right|. \tag{8.5}$$

Note that the name 'circular variance' can be confusing. The result this equation gives is a value of how different the angles of vectors are on a scale from zero to one. Where at zero the angles are all exactly the same and at one all angles are uniformly distributed on the unit circle.

8.3.2. Proof of Concept

To prove the validity of adaptive coherent summation, the performance of the different clutter suppression methods stated in section 8.2 is tested. For this proof of concept the testing filter of equation 8.4 has been applied. Each different method is evaluated by the given performance indicators for regular coherent summation, adaptive coherent summation for regular beam forming and adaptive coherent summation with the MVDR.

The results for stacked sub array combining and the variable array shift are shown in table 8.2. For the static array shift, the evaluation is performed for each possible sub array size. These results are displayed in figure 8.7. For each of these methods, the variance-filter-map and the corresponding range Doppler image are shown in figures 8.8, 8.9 and 8.10. Where for SAS the optimum point, the MVDR with sub array size of 16 was used. Ideally, the secondary target, left of the tanker, should be completely removed. From these figures some conclusions can be drawn;

	PTC	PTB	PTT
SSC	33.02	58.93	22.08
SSC VarMap	35.81	62.73	22.65
VAS MVDR	37.76	57.81	21.42
VAS DBF	34.53	61.78	21.88
VAS MVDR VarMap	44.42	70.00	21.57
VAS DBF VarMap	38.39	71.42	22.02

Table 8.2: Performance table for different clutter suppression combination techniques with a test filter

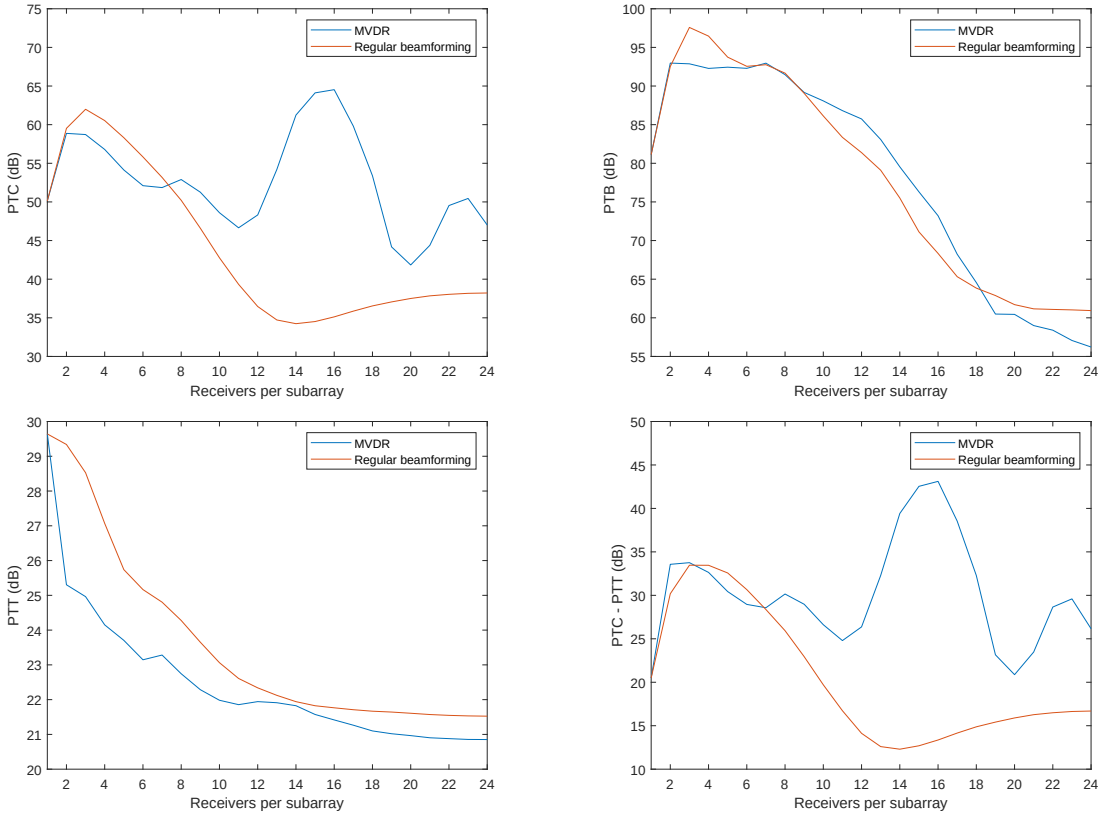

Figure 8.7: Performance indicators for different array sizes in static array shift, PTC-PTT indicates the target to clutter ratio

- The adaptive coherent summation method works.
- Table 8.2 and figure 8.7 show that SAS with MVDR and 16 receivers per sub array is the most effective in this scenario.
- The optimum at 16 receivers with MVDR is caused by the location of the secondary clutter (with 16 receivers the main-lobe is small enough to put a null at the secondary clutter) and is thus scenario dependent.
- The testing filter can be adjusted to filter out more clutter.

For the time delayed image combining, the results look useless. The variance-map of a setup where the time-shift has been kept to a minimum is shown in figure 8.11. The figure clearly shows that the target is lost. This is most likely due to difference in motion of the different components on the target itself. Only the strongest scatterer remains visible.

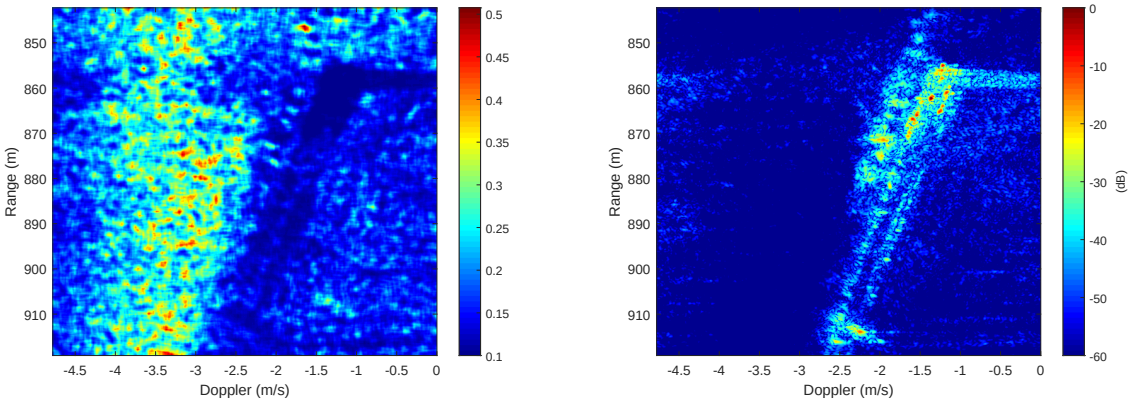

(a) Variance filter, denominator in equation 8.4

(b) Range Doppler image with regular DBF and test filter

Figure 8.8: Performance of stacked sub array combining where the test filter has been applied

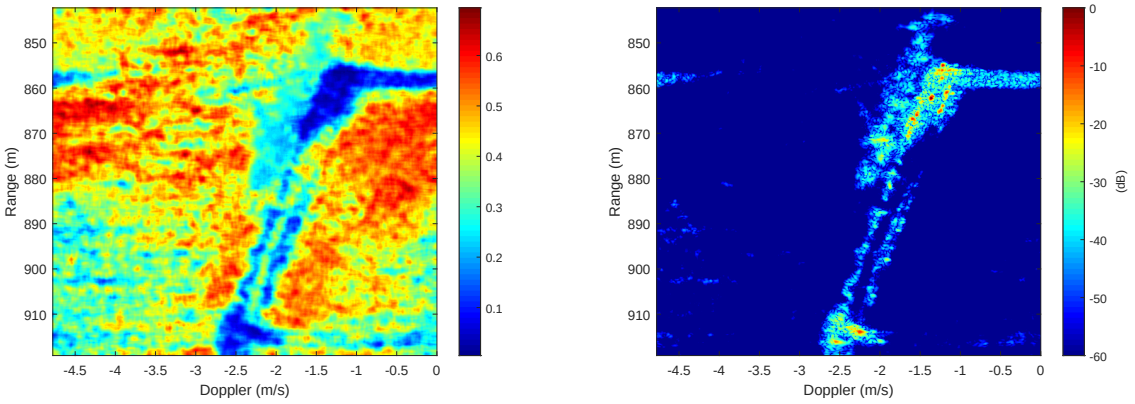

(a) Variance filter, denominator in equation 8.4

(b) Range Doppler image with regular DBF and test filter

Figure 8.9: Performance of variable array shift where the test filter has been applied

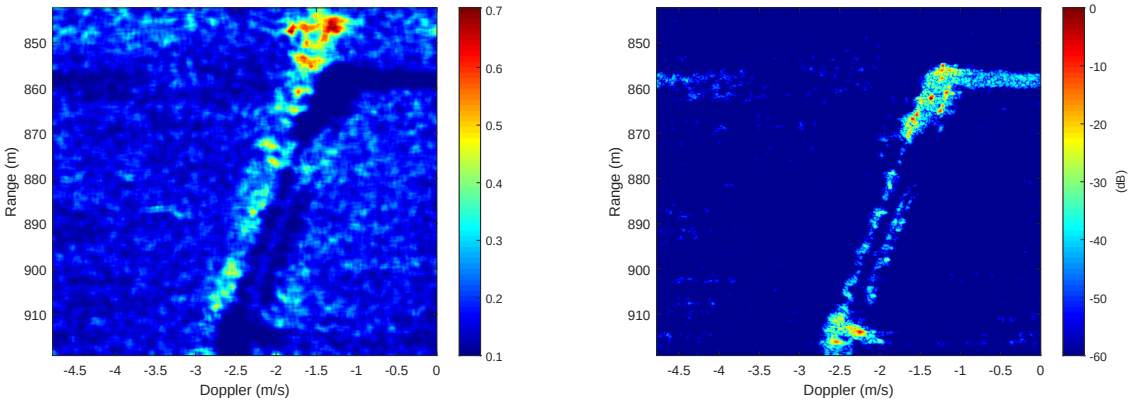

(a) Variance filter, denominator in equation 8.4

(b) Range Doppler image with regular DBF and test filter

Figure 8.10: Performance of static array shift with 21 overlapping sub arrays of 4 receivers where the test filter has been applied

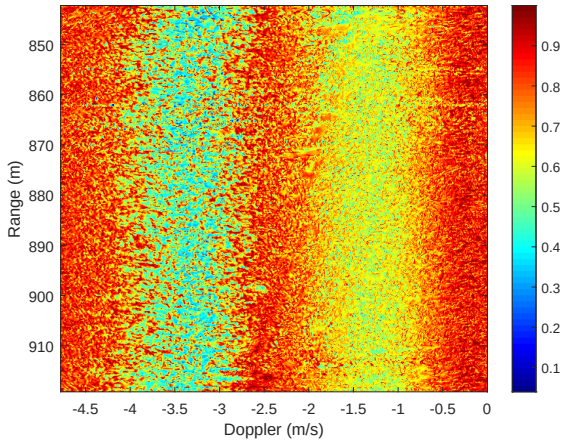

Figure 8.11: Circular phase variance map for time delayed image combining

8.3.3. Mathematical Substantiation

Lets examine why this altered coherent summation approach works for the methods where coherent summation is performed within one sweep. Consider a simple setup with four receivers with an interelement spacing of a half wavelength. A target is located at some range r_t and some angle θ_t. The steeringvector to steer the beam towards the target is then defined as:

$$\boldsymbol{s}_m = \exp(-i(m-1)\pi \sin\theta_t). \tag{8.6}$$

Where m is the mth receiver element. The received demodulated signal for the target after beam steering is shown in equation 8.7. The third order term has been left out as its impact is negligible. Note that this assumption will not have impact on the adjustments done in the equations below.

$$\boldsymbol{S}_m(f,t) = P(f)A_t \exp\left(i\frac{4\pi}{c}(f+f_c)\left(\boldsymbol{r}_{tm} + \dot{\boldsymbol{r}}_{tm}t + \frac{\ddot{\boldsymbol{r}}_{tm}}{2}t^2\right)\right)\boldsymbol{s}_m. \tag{8.7}$$

Where $\boldsymbol{r}_{tm}$ is the range from the target to element m;

$$\boldsymbol{r}_{tm} = r_{t1} + \frac{1}{2}(m-1)\sin\theta_t\frac{\lambda}{2}. \tag{8.8}$$

Where r_{t1} indicates the range between the target and the first receiver. Note that the range difference should only bet counted once, as the transmitter remains on the same position. The factor $\frac{1}{2}$ is added to this equation to cancel the multiplication which is performed in the demodulated signal for the round trip delay. The additional phase is not doubled since it does not occur at the transmitter side.
Before substituting equation 8.8 in equation 8.7 two assumptions are made.

- The signal is in narrowband, f is small compared to f_c.
- The changes in velocity and acceleration between the different receiver elements are negligible due to the target being in far-field.

Combining the two equations yields;

$$\begin{aligned}\boldsymbol{S}_m(f,t) = P(f)A_t \exp\Bigg(&i\frac{4\pi}{c}(f+f_c)\left(r_{t1} + \dot{r}_{t1}t + \frac{\ddot{r}_{t1}}{2}t^2\right)\\ &+\left(if_c\frac{4\pi}{c}\frac{1}{2}(m-1)\sin\theta_t\frac{\lambda}{2} - i(m-1)\pi\sin\theta_t\right)\Bigg).\end{aligned} \tag{8.9}$$

Where the term in the second line of equation 8.9 is cancelled out, such that,

$$S_1(f,t) = S_2(f,t)... = S_M(f,t). \tag{8.10}$$

Which means that all these signals will keep the same phase for the target scatterer and can be summed coherently with any form of how the different elements are combined before and after motion compensation.

Now consider some clutter which has the same range $r_{c1} = r_{t1}$, but has a different AOA, θ_c. The steeringvector will remain the same, but the range to each individual element becomes;

$$\boldsymbol{r}_{ce} = r_{c1} + \frac{1}{2}(m-1)\sin\theta_c \frac{\lambda}{2}. \tag{8.11}$$

In this case, combining equations 8.7 and 8.11 yields,

$$\begin{aligned}\boldsymbol{S}_m(f,t) = P(f)A_t \exp\Bigg(i\frac{4\pi}{c}(f+f_c)\left(r_{t1} + \dot{r}_{c1}t + \frac{\ddot{r}_{c1}}{2}t^2\right) \\ + \left(if_c\frac{4\pi}{c}\frac{1}{2}(m-1)\sin\theta_c\frac{\lambda}{2} - i(m-1)\pi\sin\theta_t\right)\Bigg).\end{aligned} \tag{8.12}$$

To simplify the equations the demodulated signal of the clutter is abbreviated as the term $\boldsymbol{D}_c(f,t)$ is introduced and equation 8.12 is rewritten as,

$$\boldsymbol{S}_m(f,t) = \boldsymbol{D}_c(f,t)\exp\left(i(m-1)\pi(\sin\theta_c - \sin\theta_t)\right). \tag{8.13}$$

Lets now consider the 4 receiver elements. When applying SAS with an array size of 2, three different sub arrays are formed,

$$\boldsymbol{S}_{A12}(f,t) = \boldsymbol{D}_c(f,t)\Big(1 + \exp\left(i\pi(\sin\theta_c - \sin\theta_t)\right)\Big) \tag{8.14}$$

$$\boldsymbol{S}_{A23}(f,t) = \boldsymbol{D}_c(f,t)\Big(\exp\left(i\pi(\sin\theta_c - \sin\theta_t)\right) + \exp\left(i2\pi(\sin\theta_c - \sin\theta_t)\right)\Big) \tag{8.15}$$

$$\boldsymbol{S}_{A34}(f,t) = \boldsymbol{D}_c(f,t)\Big(\exp\left(i2\pi(\sin\theta_c - \sin\theta_t)\right) + \exp\left(i3\pi(\sin\theta_c - \sin\theta_t)\right)\Big). \tag{8.16}$$

Note that the demodulated clutter signal is now multiplied by a scalar, which will cause a change in phase of the signal. The equations are simplified as,

$$\boldsymbol{S}_{A12}(f,t) = \boldsymbol{D}_c(f,t)p_1, \tag{8.17}$$

$$\boldsymbol{S}_{A23}(f,t) = \boldsymbol{D}_c(f,t)p_2, \tag{8.18}$$

$$\boldsymbol{S}_{A34}(f,t) = \boldsymbol{D}_c(f,t)p_3. \tag{8.19}$$

Which can be written in vector notation as,

$$\boldsymbol{S}_{Aa}(f,t) = \boldsymbol{D}_c(f,t)\boldsymbol{p}_a. \tag{8.20}$$

Such that a indicates the sub array number. The next step in the imaging scheme is to apply the keystone transform. As the keystone transform is a time-rescaling operation, it does not influence $\boldsymbol{p}_a$ and only alters $\boldsymbol{D}_c(f,t)$. Next are the fold over correction, acceleration compensation and third order motion compensation. All these operations are multiplications which add a time-dependent phase to the demodulated signal. Although the clutter is not motion compensated, smearing it in range and Doppler, the differences between the sub arrays remain dependent only on $\boldsymbol{p}_a$. The final operation is the two-dimensional Fourier transform. This operation is also independent of the multiplication with a scalar.
This means that the variance in phase between the different sub arrays is caused by the phase differences of $\boldsymbol{p}_a$. Independent on how the different elements are combined within a sub array, as long as the steeringvector is applied correctly. This results in;

$$\mathrm{Var}(\angle\boldsymbol{S}(R,f_d)) = \mathrm{Var}(\angle\boldsymbol{p}_a). \tag{8.21}$$

As equations 8.14, 8.15 and 8.16 show, $\boldsymbol{p}_a$ is only dependent on the AOA of the clutter. And thus will the variance also dependent on the AOA of the clutter. The 2 different methods of combining range Doppler images within one sweep are simulated for variance with clutter from different AOA. The result of this simulation is shown in figure 8.12.

The figure shows that SAS improves when the number of receivers per sub array is reduced. SAS also has a higher variance than VAS and is thus less sensitive to noise. There is a clear dip in variance for clutter which has the same AOA as the target, as the beam is focussed on this clutter as well.

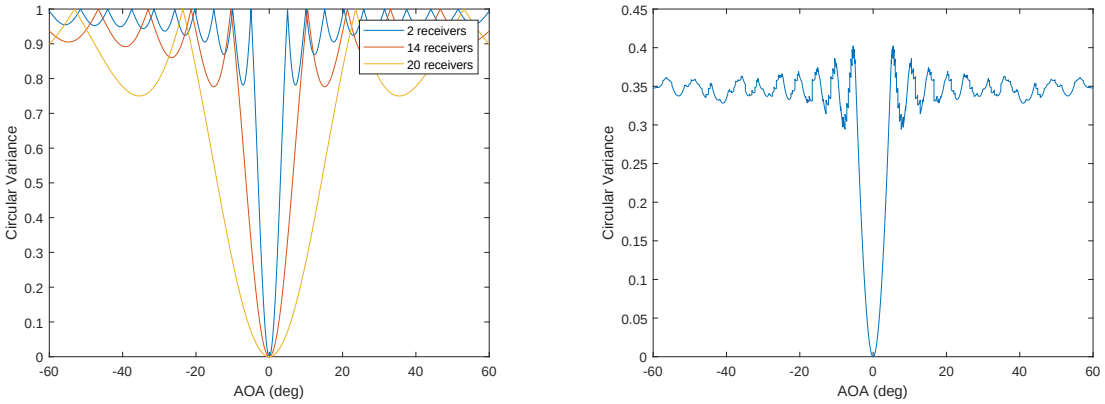

(a) Static array shift

(b) Variable array shift

Figure 8.12: Variance from clutter at a certain angle for different combination techniques while the radar is focussed at 0 degrees

8.4. Optimization

As previously only a test-filter was used, optimization is required. Based on the results of section 8.3.2, there are some important items to consider before optimizing the filter.

- The quality of the variance-maps rises when the sub arrays are smaller. But the quality of the image from coherent summation drops when the sub arrays are smaller.
- Due to overlapping sub arrays, not all elements are used an equal amount of times. Which may give rise to more noise.
- The moving average filter may remove important features of the target.

As SAS proved to be better than VAS, only SAS will be considered in this section. Lets begin by redefining the proposed adaptive coherent summation scheme according to the items above.

- The range Doppler image in SAS is created by coherent summation of the sub arrays. Herafter the variance-map is applied onto this image. However, smaller sub arrays may yield a better variance-map while having a poor range Doppler image. Thus as a new approach, the range Doppler image will be created by regular DBF, MVDR or ODPCA, as the variance-map-filter is only an operation on the amplitudes of the final range Doppler image.
- Overlapping sub arrays are avoided, given a receiver array of 24, this results in 7 possible sizes of sub arrays: 1, 2, 3, 4, 6, 8 and 12.
- The moving average filter is removed.
- Strong target scatterers are very unlikely to have a higher variance, while strong clutter scatterers may reside in these areas. According to this statement, the best filter is a simple rectangular window with a threshold at a certain circular variance.

To find the distribution of the target and noise, first a gap between range-slots is considered which only contains sea-clutter and no targets. For each of the different sizes of sub arrays, the circular variance histogram is compared to a circular variance histogram of uniformly distributed random phase noise for each of the sub arrays. The results are shown in figure 8.13. The figure shows that the sea clutter behaviour is very similar to random noise.
This scenario can be compared to a scenario were a target is present in the sea clutter. The results of this situation are shown in figure 8.14. The target is clearly visible at the left of the histograms, as its phases remain similar for the different range Doppler images and thus has a low circular variance.
More sub arrays lead to more variance in the noise and thus less noise on the target. However, more sub arrays do also lead to a less sharp beam for each sub array and thus more noise on the target. This phenomenon is also visible in the histograms of the real data. When more sub arrays are used, the peak at 0 variance indicating the target decreases and is spread out.

For each of the 7 options, a detection threshold is set on a probability of false alarm (PFA) of 0.05. Where it is considered that the noise behaves as the random phases as in figure 8.13. This yields the following thresholds;

$$\begin{aligned} T_1 &= 0.6485, \\ T_2 &= 0.5056, \\ T_3 &= 0.3973, \\ T_4 &= 0.3103, \\ T_6 &= 0.1543, \\ T_8 &= 0.0593, \\ T_{12} &= 0.0031. \end{aligned} \tag{8.22}$$

According to these thresholds a rectangular filter is applied, yielding the black/white images of figure 8.15. Where the white area indicates the target. It appears that the differences between the different setups are rather small. However, when the amount of sub arrays is smaller, the distinction between target and noise is harder to make. As was expected following the histograms of figure 8.14. A decision for the optimal number of sub arrays is made to be 8 for the following two reasons:

- With more sub arrays the circular variance of sea-clutter overlaps less with the target distribution than with less sub arrays.
- When setting the threshold higher, which is required for more sub arrays to cover the target, the probability of also detecting a second target rises. As the circular variance is coupled with AOA, secondary targets close to the target may avoid this filtering scheme if the number of sub arrays is high.

8.5. AOA Estimation by Phase Variance

With the theory discussed in the previous section, it is possible to distinguish clutter from a target based on its AOA. As figure 8.12 showed, clutter has a defined circular variance based on its AOA. Note that this figure shows the relation of AOA versus circular variance for overlapping arrays. In appendix F a more detailed evaluation on AOA estimation by phase variance for non-overlapping arrays is given. This appendix discusses the possibilities of estimating the AOA by the phase variance.

8.6. Results

To show how the newly proposed technique performs, this section displays several imaging results for different targets. The final imaging scheme consists of two parts.

- Firstly, an ISAR image is created by maximizing the image contrast for the ODPCA techniques, where a sweep on θ is performed.
- Secondly, a mask is created according to the theory as discussed in this chapter.

The mask is then applied on the ODPCA generated image, yielding the final range Doppler image of the algorithm. An image of the measurement site is shown in appendix G. Note that this snapshot is not taken at the exact same time index as the radar measurement. The relative location of the vessels as well as the orientation angle of the piers is different. Each target is indicated with a letter such that it can be compared with the generated results.
For each of the targets three different images are generated. The range Doppler image generated with IC maximization in ODPCA, the mask generated with the phase variance map and finally the combined image of the two. The results from all targets indicated are shown in figures 8.16, 8.17, 8.18, 8.19 and 8.20. Some interesting phenomena and artefacts about these images are discussed.

In figure 8.16e, a large red spot can be found at 1170 m in range. This spot corresponds to a strong scatterer of figure 8.16a which has been unfocussed and is now disturbing the image. Figure 8.16f shows that the red spot has been filtered out by the phase variance mask.

A very good example of how the phase variance mask is intended is shown in figure 8.17. The two targets displayed in this figure are in proximity of each other and their range Doppler images suffer from this. The

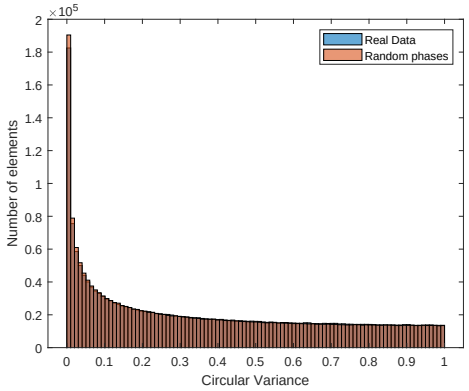

(a) 2 sub arrays

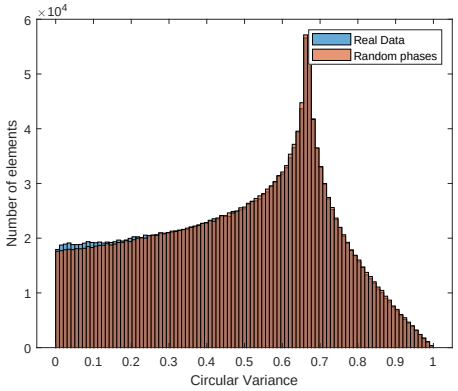

(b) 3 sub arrays

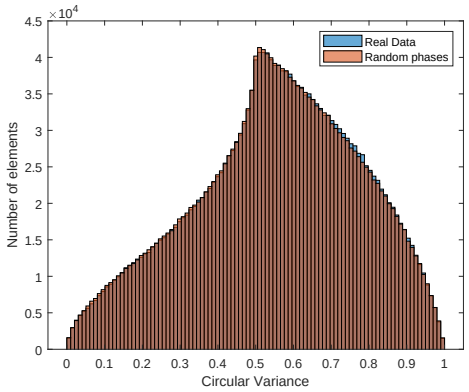

(c) 4 sub arrays

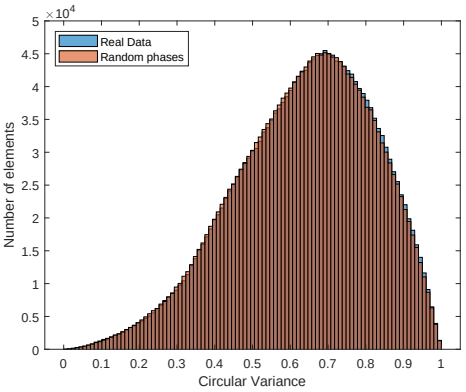

(d) 6 sub arrays

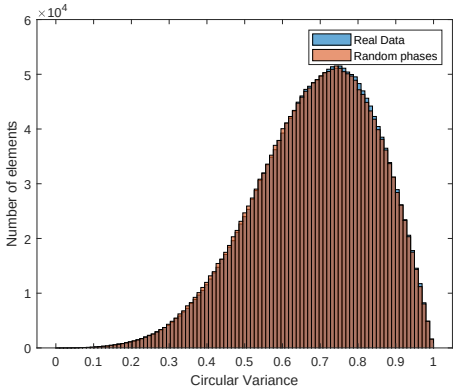

(e) 8 sub arrays

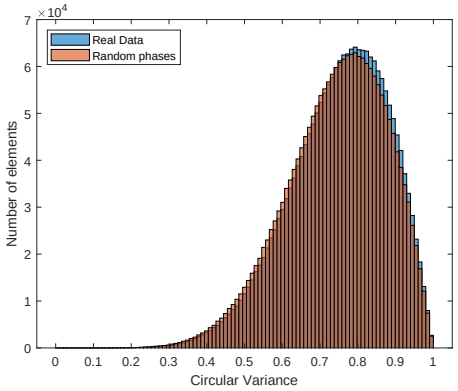

(f) 12 sub arrays

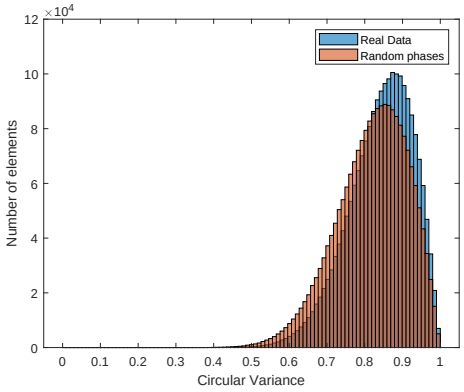

(g) 24 sub arrays

Figure 8.13: Probability density function of circular variance in the range Doppler image. Real data measurement performed in an empty part of the measurement area. The predicted probability density function shows the circular variance of uniformly distributed phases. Blue shows the real data while red shows the estimator

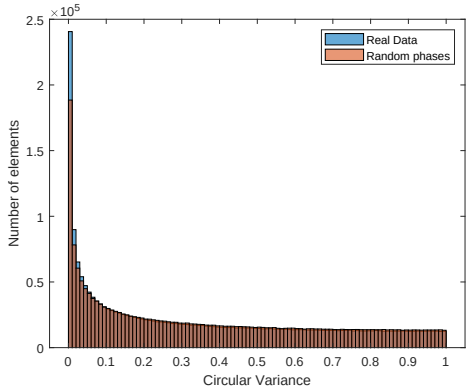

(a) 2 sub arrays

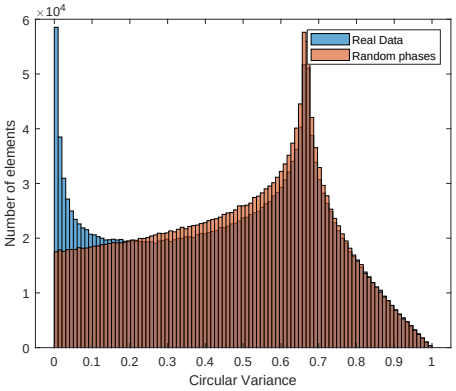

(b) 3 sub arrays

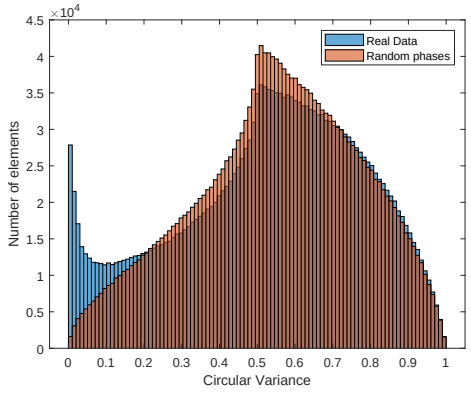

(c) 4 sub arrays

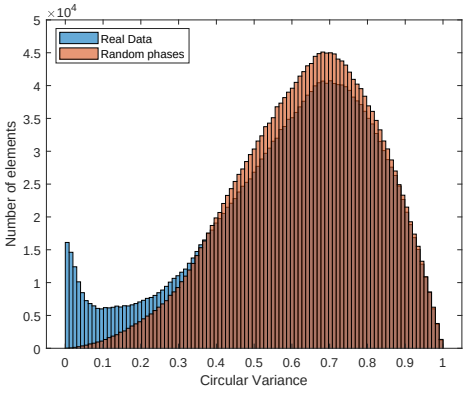

(d) 6 sub arrays

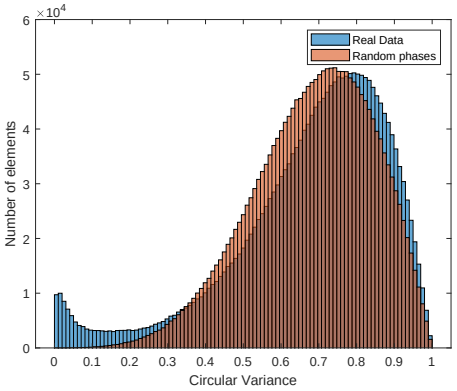

(e) 8 sub arrays

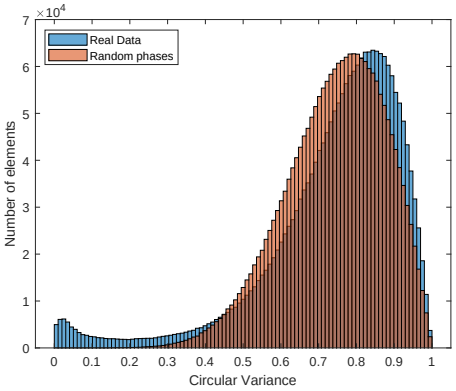

(f) 12 sub arrays

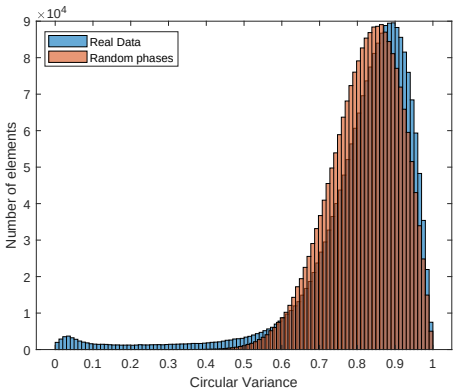

(g) 24 sub arrays

Figure 8.14: Probability density function of circular variance in the Range-Doppler image. Real data measurement performed in a part the of measurement area containing a ship. The predicted probability density function shows the circular variance of uniformly distributed phases. Blue shows the real data while red shows the estimator

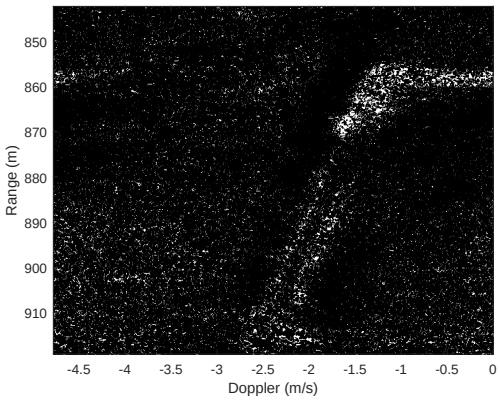

(a) 2 sub arrays

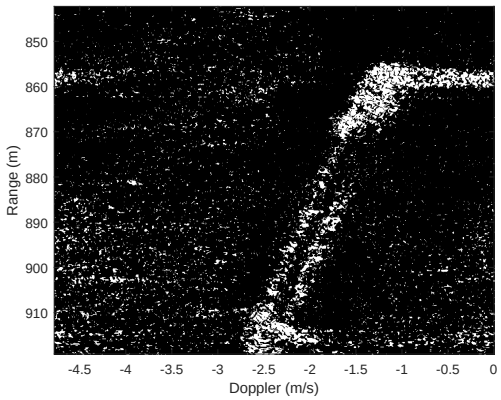

(b) 3 sub arrays

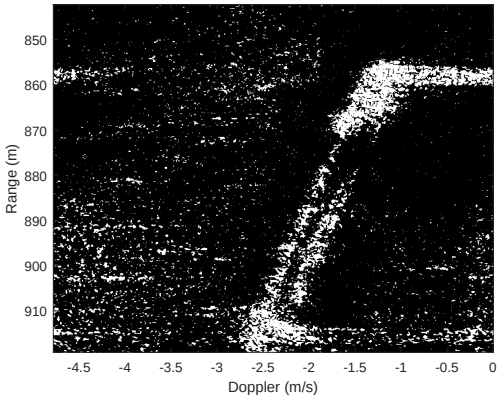

(c) 4 sub arrays

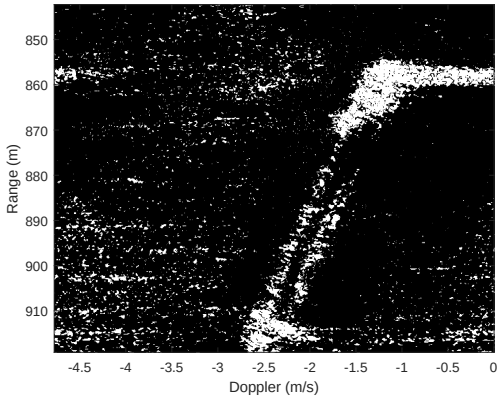

(d) 6 sub arrays

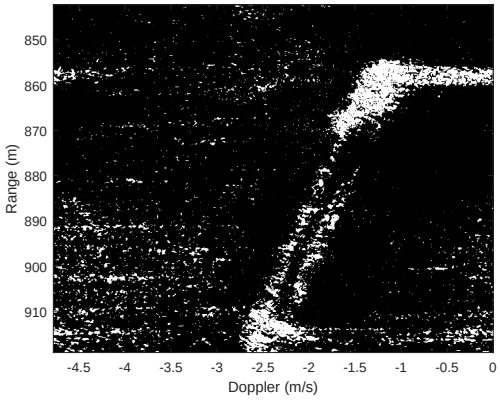

(e) 8 sub arrays

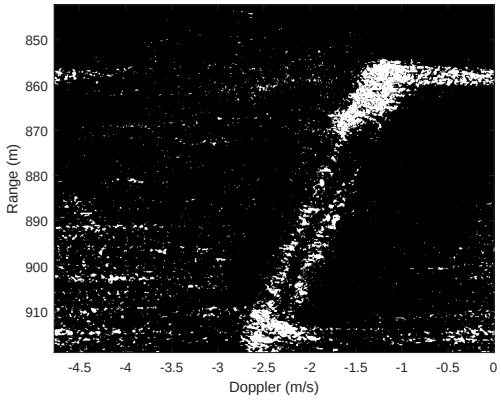

(f) 12 sub arrays

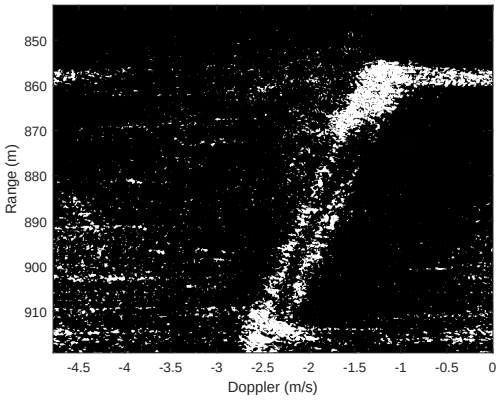

(g) 24 sub arrays

Figure 8.15: Mask for the different sub array sizes based on the thresholds indicated in equation 8.22

pier displayed in figure 8.18a is also in the same range gate as these two targets. Nevertheless, the originated clutter is effectively filtered by the ODPCA and phase variance mask.

From figure 8.18 two observations are made. The pier spans multiple AOA degrees due to the combination of close range and large size of the pier. As the targets contains multiple AOA degrees, the phase variance over the target changes dependent on its location. Due to the sheer size of the pier, its phase variance does not completely remain under the threshold. Resulting in the removal of only a part of the pier by the mask. A second observation that can be made is related to the two ships laying side by side as in figure 8.18d. The ships are not focussed very well and also after applying the phase variance mask, a part of the ship is deleted. An explanation for this phenomenom is the AOA that the two ships occupy. The 38 degrees at which the ship is located is outside the main beam of the patch antenna transmitter.

Figure 8.19a shows a lot of smears in Doppler which is visible in both the ODPCA result as in the phase variance map. The fact that these smears are visible in the phase variance map means that they are caused by something in the same AOA as the target, either the target itself or waves nearby. The actual reason for this phenomenon is unknown.

The limitations of the low PRF used in AMBER are visible in figure 8.20a. Due to the orientation, range and size of the target, it covers a multitude of the required fold over correction. Since no extra processing is done to resolve this issue, part of the target remains unfocussed. Several intriguing repeating lines in range are visible in figure 8.20d. They appear at the same Doppler and at equall spacing of about 9 m in range. Due to their location in terms of AOA and range, these lines are either regular waves or wake waves of target G which moved perpendicular to the radar and where therefore spotted.

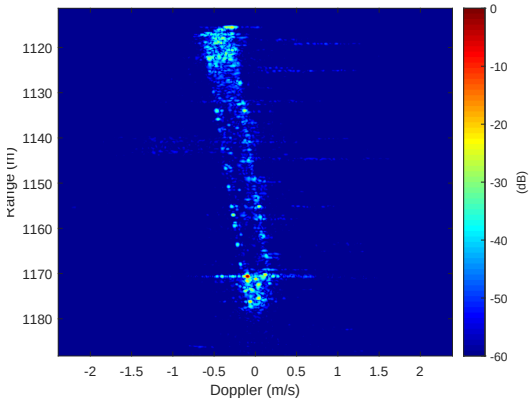

(a) IC maximization in ODPCA for target A

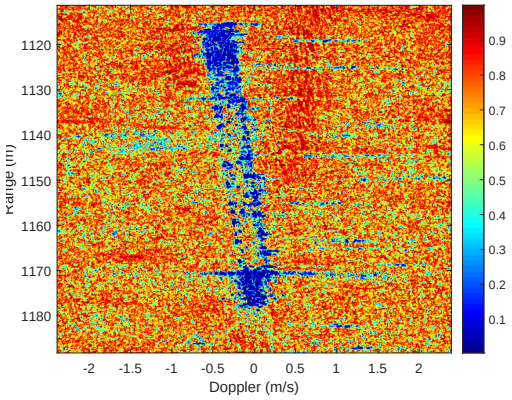

(b) Phase variance map for target A

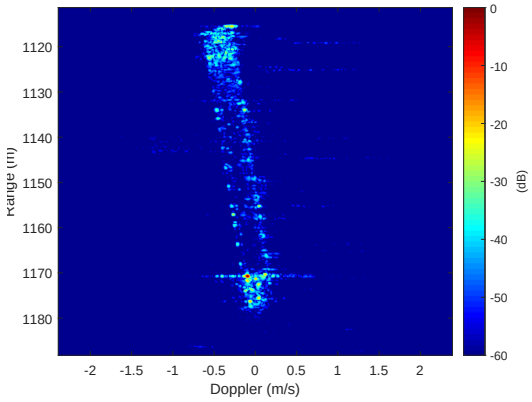

(c) Final range Doppler image of target A

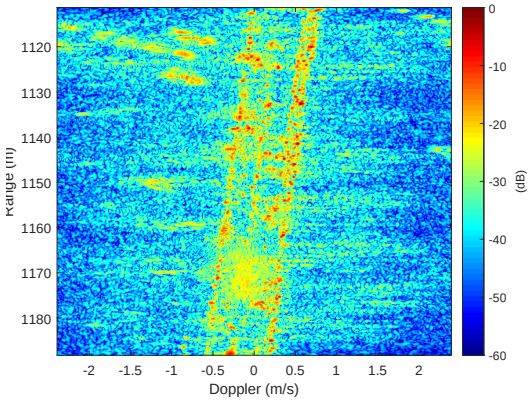

(d) IC maximization in ODPCA for target B

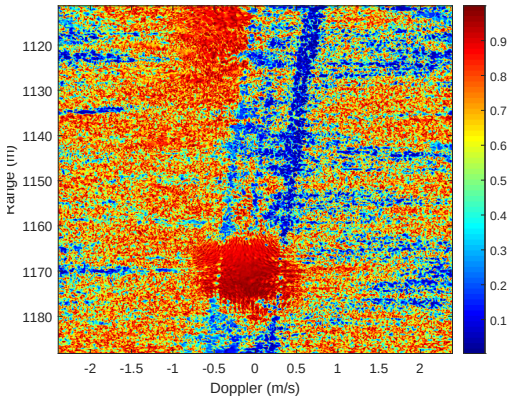

(e) Phase variance map for target B

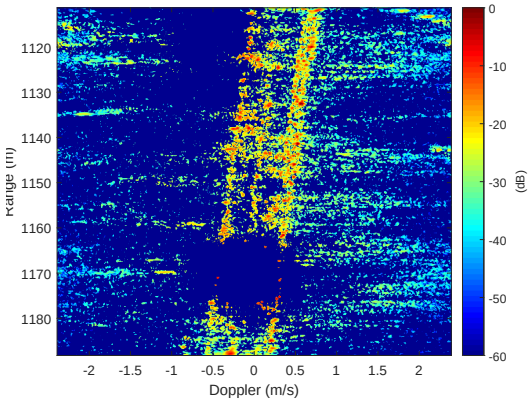

(f) Final range Doppler image of target B

Figure 8.16: Resulting ODPCA image, phase variance map and final range Doppler image of target A and B

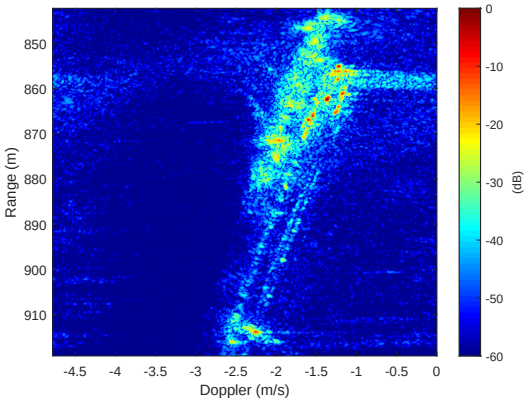

(a) IC maximization in ODPCA for target C

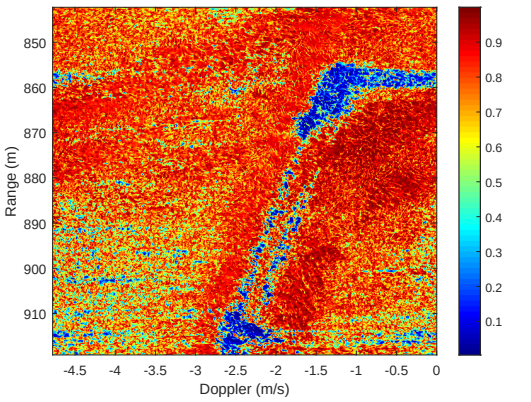

(b) Phase variance map for target C

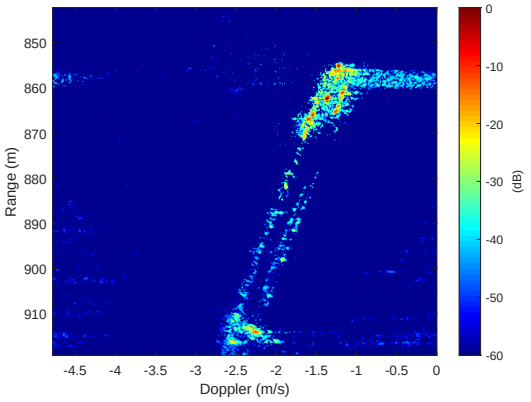

(c) Final range Doppler image of target C

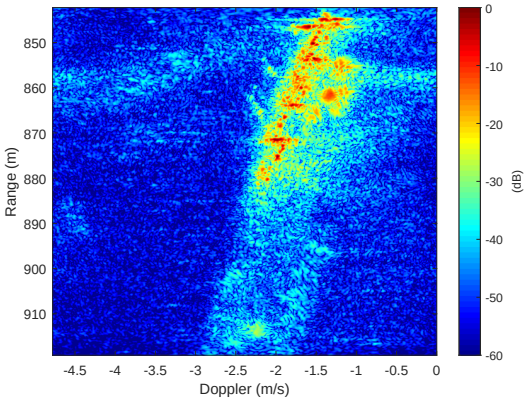

(d) IC maximization in ODPCA for target D

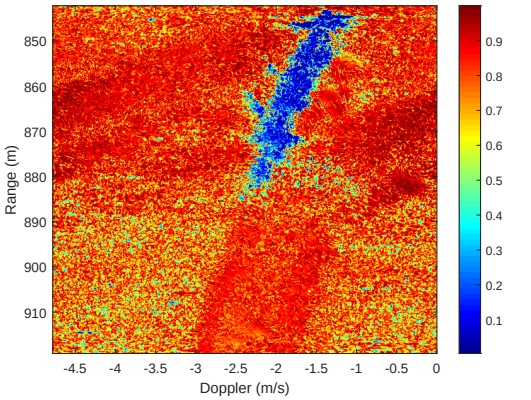

(e) Phase variance map for target D

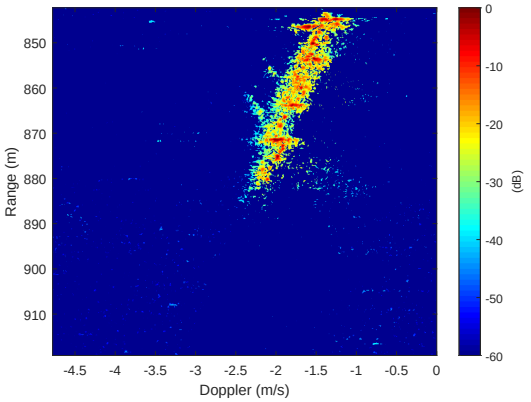

(f) Final range Doppler image of target D

Figure 8.17: Resulting ODPCA image, phase variance map and final range Doppler image of target C and D

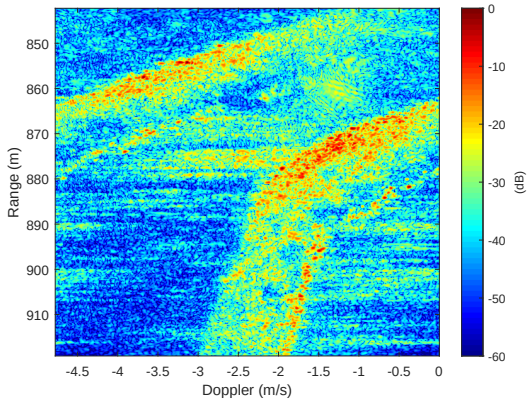

(a) IC maximization in ODPCA for target E

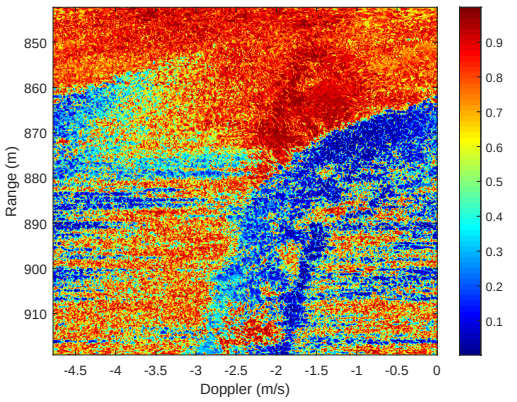

(b) Phase variance map for target E

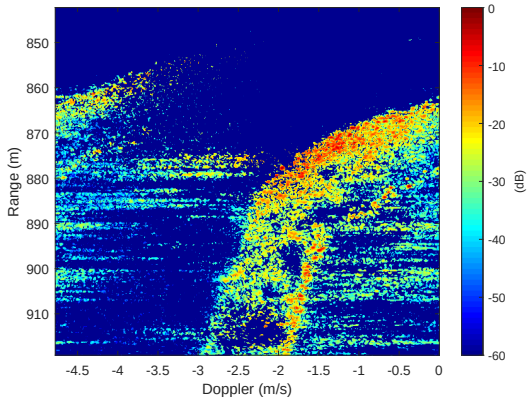

(c) Final range Doppler image of target E

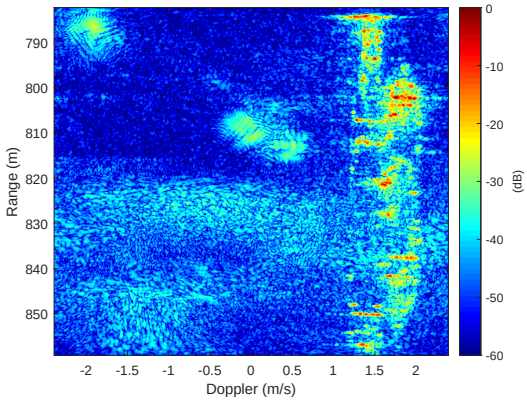

(d) IC maximization in ODPCA for target F

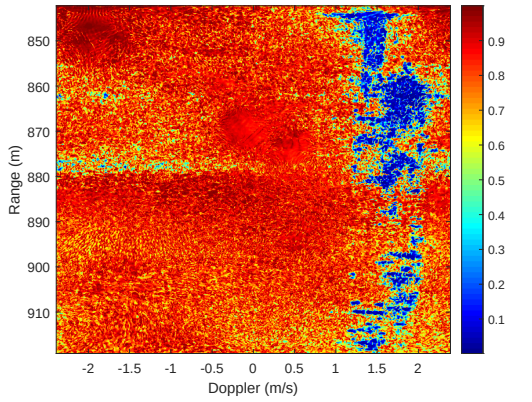

(e) Phase variance map for target F

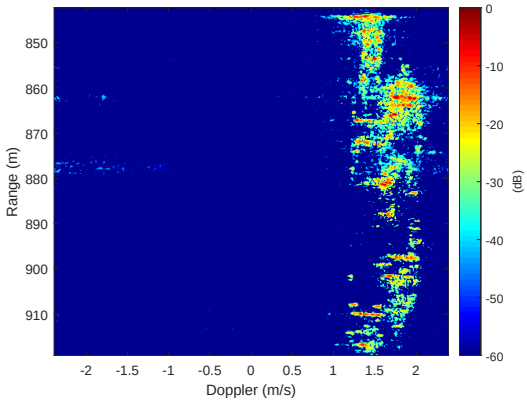

(f) Final range Doppler image of target F

Figure 8.18: Resulting ODPCA image, phase variance map and final range Doppler image of target E and F

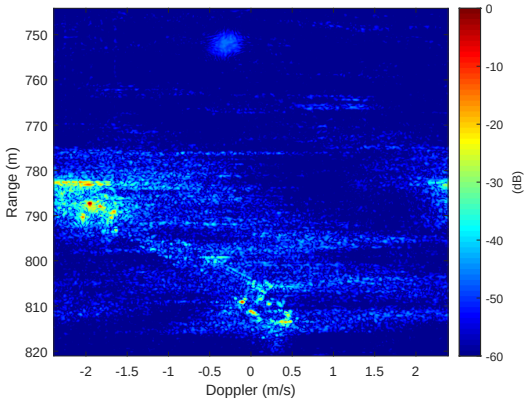

(a) IC maximization in ODPCA for target G

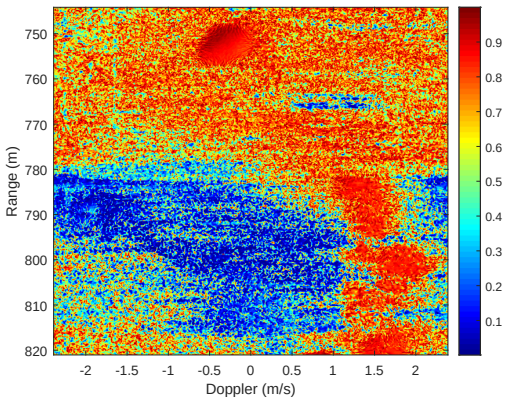

(b) Phase variance map for target G

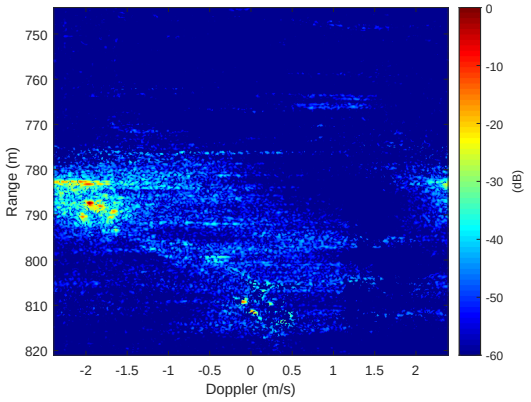

(c) Final range Doppler image of target G

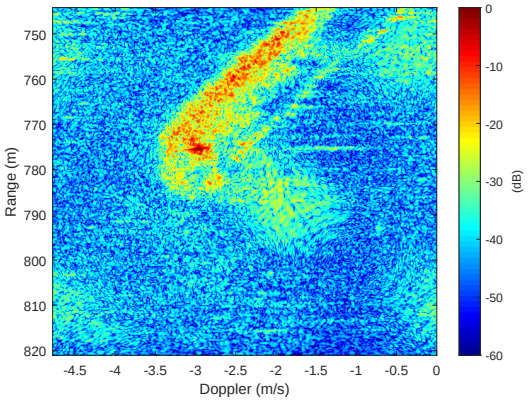

(d) IC maximization in ODPCA for target H

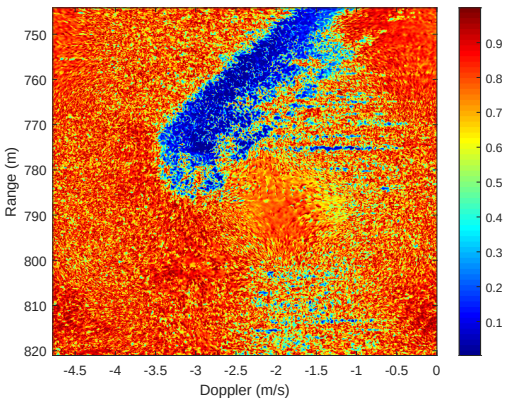

(e) Phase variance map for target H

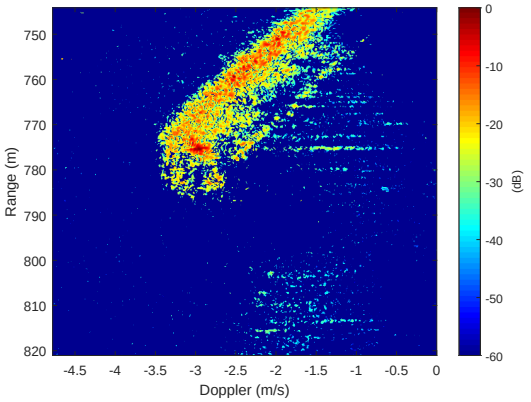

(f) Final range Doppler image of target H

Figure 8.19: Resulting ODPCA image, phase variance map and final range Doppler image of target G and H

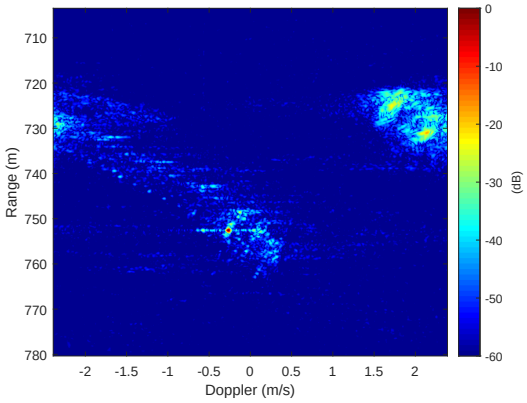

(a) IC maximization in ODPCA for target I

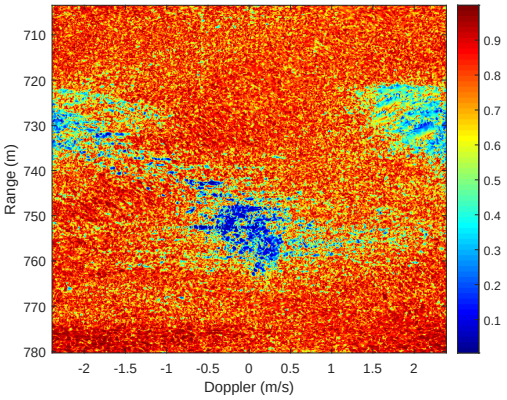

(b) Phase variance map for target I

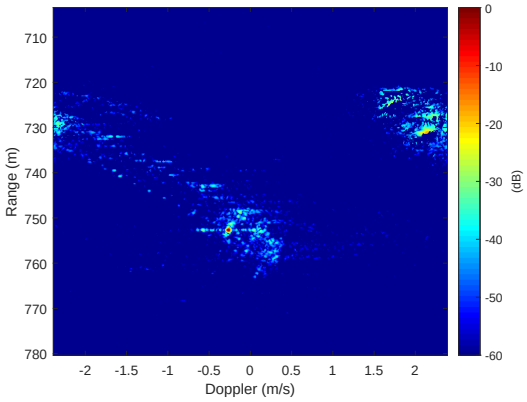

(c) Final range Doppler image of target I

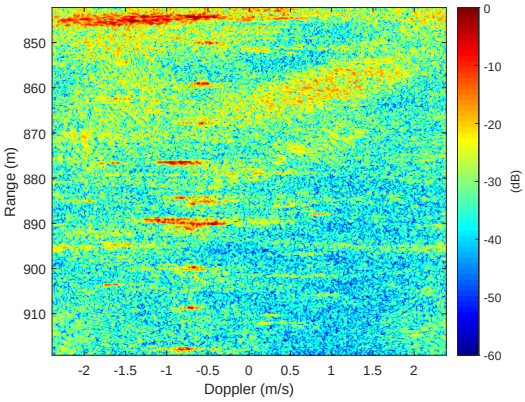

(d) IC maximization in ODPCA for target J

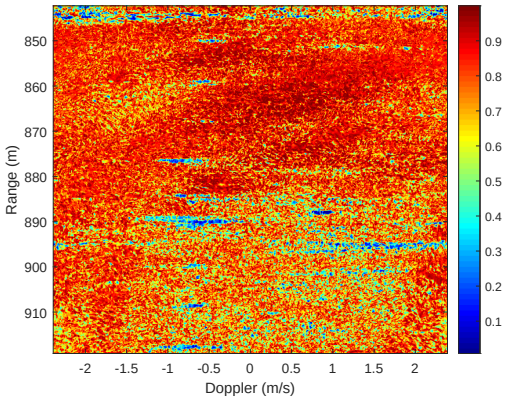

(e) Phase variance map for target J

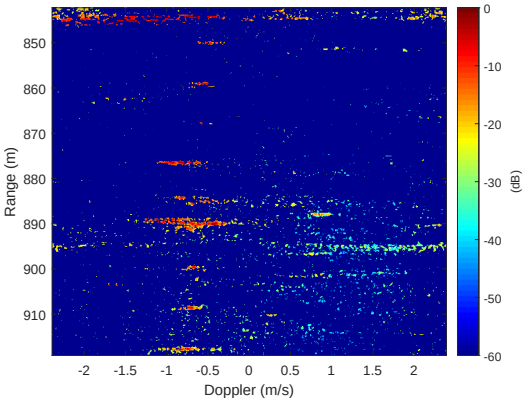

(f) Final range Doppler image of target J

Figure 8.20: Resulting ODPCA image, phase variance map and final range Doppler image of target I and J

9

Sytem Overview

In the previous chapters, all the different subcomponents of the final algorithm have been researched and evaluated. Based on evaluations and literature, a choice has been made for the best implementation for ISAR imaging with AMBER. This chapter is aimed to give a clear overview of the complete system.

A flow-diagram of the algorithm can be seen in figure 9.1. The algorithm can be cut up in roughly three different parts, motion estimation indicated in green, ODPCA in blue and the variance filter in yellow. How each of these functions operate will be discussed in the following sections.

9.1. Input Data

The data used as input for this algorithm, indicated as 24 receiver raw data is not the complete raw data received from the radar. As it is considered that the location of the targets is known beforehand the data indicated in figure 9.1 has already been cropped.

9.2. Motion Estimation

The green part in figure 9.1 has the purpose of estimating the considered target. This is done separately, since estimating the motion parameters is quite error-sensitive when there are other targets nearby. When using the complete 24 receive array, the main lobe beam-width is smallest and the contribution from different angles is minimized. This gives the best conditions to apply image contrast maximization to estimate the motion parameters.
As the keystone algorithm solves RCM of the targets scatterers within the velocity ambiguity limits, only a foldover estimate needs to be performed for the velocity compensation, as explained in section 4.6. A first crude estimate of the velocity is done based on the position of the target with respect to the radar and on the velocity of the radar.
For the estimation of the acceleration, the same principle is applied. An estimation is first performed based on the location of the target, the velocity of the radar and the estimated foldover factor. The image contrast is calculated for acceleration values close to the estimated value, to find its maximum which should correspond to the actual relative acceleration of the target with respect to the radar.

9.3. ODPCA

The ODPCA is implemented as discussed in section 5.4 and is shown in blue. It was chosen to use two sub arrays as this proved to give a better performance. The two sub arrays are aligned by using spatial interpolation in the same manner as is done with regular DPCA. As the ideal phase multiplication for ODPCA is unknown, a search is done of θ from $-\pi$ to π. Note that the incrementation size can not be to small, as creating the range Doppler image is no simple procedure. The resulting curve of image contrast values is then interpolated to find the best estimate of the phase shift value for ODPCA.

9.4. Variance Filter

The variance filter is displayed in yellow in the figure. As was discussed in section 8.4, 8 sub arrays of 3 receivers was the most ideal setup. This is done without overlapping the sub arrays. For each individual sub array, motion compensation is applied according to the estimated motion parameters. The range Doppler images are created, from which the phase variance of all the pixels within this image is computed. According to the phase variance and the threshold of PFA set on 0.05, a mask in generated which is finally applied on the image generated by the ODPCA method.

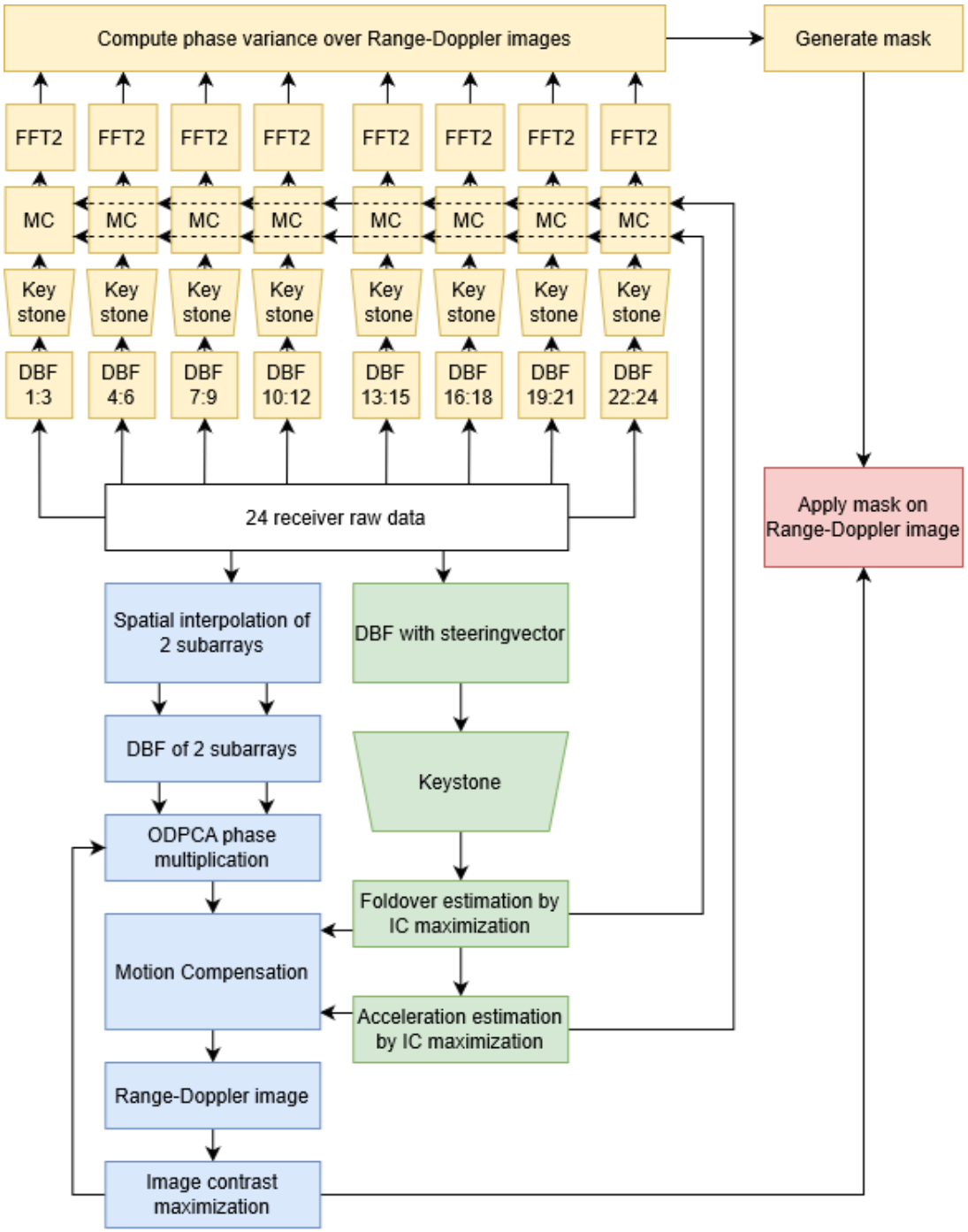

Figure 9.1: System overview of the complete algorithm

10

Conclusion and Recommendations

At the beginning of this thesis, the research questions where stated. Consisting of a main question and several sub-questions. This conclusion aims to give a concise answer to these questions and will also discuss the novelty this thesis brings. The section will be concluded with several recommendations for future work regarding this particular topic.

The main goal of the thesis was to find the best way to exploit DBF with an FMCW multichannel receive radar in airborne ISAR imaging while maintaining processing limitations. This problem was to large to solve at once and was split up in the sub-questions.

The first sub-question revolved around the required background information on existing ISAR algorithms and on how they worked. Chapter 4 discussed the main principles of ISAR and elaborated on existing algorithms. The RDA, Range centroid, cross correlation, minimum entropy, Doppler centroid, phase gradient, minimum variance, IC maximization, PPP, range Doppler backprojection and the first and second order keystone transform where discussed.

Based on the findings of the first sub-question, research on the second sub-question could be performed. The second-sub-question was about the performance of the different ISAR algorithms. A performance analysis on the fundamental motion compensation techniques was performed and is discussed in chapter 6. Based on simulations several ISAR algorithms as well as combinations were tested for their performance. Based on the findings it was decided that the Keystone algorithm was most effective due to its independence of noise and high quality point spread functions, as well as its ability to align scatterers in range which showed different motion from each other. However, due to the high velocity of targets and low PRF of the system, targets could appear outside the Doppler ambiguity limits. The keystone transform itself was not sufficient. To solve these motions, an additional parametric approach was required. Which meant that an estimation of the targets motion parameters had to be performed. This estimation was done with IC maximization. The combined methods were ideal for ISAR imaging. With this combination, all the scatterers of a target can be aligned in range even when due to the size of the target, they would show different motion.

The third sub-question asked about the impact of having a moving platform instead of the regular ISAR setup with a stationary platform. As explained in chapter 4, the addition of having a moving platform does only change the relative location of the radar with respect to the target. And does not have an impact on how the ISAR imaging algorithms are applied.

As all issues regarding motion compensation have been solved, the fourth sub-question revolved around beam forming. In particular, it questions what the added value of the multichannel receiver array is. Although part of this question is answered with the next and final sub-question, a study on the effects of having a larger receiver array can be found in appendix E. It was shown that having more receivers improved the image quality, since the image can be focussed better as more clutter from different AOA is suppressed.

The final sub-question concerns about the options of digital beam forming in ISAR. First, the theory about several methods of using the multichannel receiver array is discussed in chapter 5. In this chapter, regular beam forming, MVDR, DPCA and ODPCA are considered. These techniques are applied on real measured data and evaluated in chapter 7. The applied techniques improved the results, but more improvements were sought. Coming to a point were the newly applied techniques exceeded literature and novelty was presented.

The first proposed technique was aimed to combine ODPCA with MVDR to reach results which would trump both. This new technique, IDPCA, used multiple sub arrays over multiple measurements to filter a target based on its individual motion. Section 7.2.2 explained the technique in more detail. In chapter 8 the methods SSC, VAS, SAS and TDIC were proposed to find the optimal approach for combining sub arrays in IDPCA. Based on the theory behind the approach as well as on measurements the following conclusions on IDPCA were drawn;

- IDPCA shows improvement on the using the individual methods separately.
- The benefits gained from IDPCA are limited due to coherent summation. Due to the difference in amplitudes of clutter, even scatterers with destructive interference can only be suppressed a limited amount.
- Although some of the sub array combination techniques were time-independent, they still appeared to improve the results. This was theoretically unexpected as IDPCA filtered based on motion and without time difference, motion should not have any impact on the results.

The interesting phenomenon was researched and it was found that the improvements even with time-independent sub arrays were caused by the AOA of clutter. Based on these findings a new approach was sought which emphasised the phases of pixels in the range Doppler image. As was shown in section 8.3, the phases of pixels could be used to identify whether this pixel belonged to the considered target or not. A variance map was created which showed in which pixels the target was contained. This variance map formed into a mask which was able to filter out clutter effectively. Several observations and conclusions can be drawn from this new approach;

- If the beams of the sub arrays are steered towards the target, the target will show a theoretical circular variance of zero. But this is only true if the steeringvector is applied to each individual receiver as if it is part of the complete 24-channel receiver size array.
- There is a defined relation between the AOA of clutter, the number of sub arrays and the circular variance this clutter cell shows.
- The relation between AOA of clutter and circular variance show grating lobes of a circular variance of zero. With more receivers per sub array, more grating lobes appear. However, with more receivers per sub array, the beam is focussed more. Due to this effect, the grating lobes have little to no impact on the results.
- As long as strong clutter is not located in the same pixels in the range Doppler image as the target, the target can always be classified.
- The technique proved to be extremely effective to filter out strong clutter components which could not be filtered with ODPCA or MVDR.

In engineering, achieving the ideal solution to a problem is close to impossible and although the solution presented in this thesis is very effective, it is by no means perfect. Several recommendations on how the algorithm could be altered to possibly improve the results are as follows;

- The amount of possibilities on how to combine sub arrays, be it overlapping or not overlapping, same size or different size, is vast. From the tested possibilities the solution given in this thesis was the best. However, there may be improvements by combining the sub arrays in different manners.
- The ideal ODPCA phase shift is found by searching the maximum IC. As was also the case for MVDR, IC maximization may not be the ideal approach to reach the best image quality, as it works better for focussing than for clutter suppression.

- Since the rotation rate of the targets is very small for the scenario presented in this thesis, apart from acceleration compensation, no further rotational motion compensation techniques are applied. It could be worthwhile to find out if applying polar formatting at some stage in the algorithm can improve the image quality more.

Publications

Conference proceedings

P1 N.J. de Jong, M.P.G. Otten, M. Caro Cuenca, F. Uysal, J.J.M. de Wit, "ISAR imaging with FMCW multi-channel airborne SAR", accepted, in Proceedings of EUSAR 2020: 13th European Conference on Synthetic Aperture Radar, June 2020

P2 N.J. de Jong, M.P.G. Otten, M. Caro Cuenca, F. Uysal, J.J.M. de Wit, "An ISAR imaging mask by phase variance of sub arrays in the RD domain", in preparation

A

SAR Processing Techniques

When speaking of SAR processing techniques a distinction can be made between 2 classes. Algorithms based on the use of frequency domain techniques and algorithms that use time domain techniques. There is an abundance of frequency based methods such as the Range Doppler Algorithm (RDA), Chirp Scaling Algorithm (CSA), Omega-k Algorithm, Polar formatting and more. The frequency domain based techniques make a lot of assumptions based on squint, range curve migration, platform motion and more. It is needles to say that this degrades the performance. On the other side there is Backprojection (BP) in the time-domain. This method does not make many assumptions and shows some advantages against the frequency domain algorithms [33]. Although Backprojection has a lot of advantages, it is also relatively computational expensive and requires precise knowledge of the imaging geometry. The different processing techniques will be discussed in the following sections.

A.1. Range Doppler Algorithm

The Range Doppler Algorithm is the most basic and most used frequency based technique. The algorithm can be described in several steps [7, 34, 35]. As mentioned above, all types of SAR processing start with the demodulated base-band signal as given in equation 3.18. The processing steps for the Range Doppler Algorithm are as follows.

1 Range Compression

2 Azimuth FFT

3 Range cell migration correction (RCMC)

4 Azimuth Compression

5 Azimuth inverse FFT

Each of these processing steps will be discussed briefly. An important note is that this procedure follows the stop-and-go protocol. This means that the position of the radar is considered stationary during the transmission and reception of a single pulse.

Range Compression (RC) In this first step, pulse compression is applied. This increases the range resolution. First, the FFT in the range domain is taken, followed by a matched filter multiply in the azimuth-time domain. Then the IFFT is taken to get back to the range-azimuth domain. This procedure is also known as a fast convolution as it uses the Fourier domain to avoid the processing time it costs to perform a convolution without changing the outcome. The term range compression comes from the fact that pulse compression is applied in the range direction. Performing range compression yields the following equation.

$$s(\tau,\eta) = A_0\, p_r[\tau - \frac{2R(\eta)}{c}]\, w_a[\eta-\eta_c] \exp(-j4\pi f_0 \frac{R(\eta)}{c}). \tag{A.1}$$

Azimuth FFT The azimuth FFT transforms the domain to Range-Doppler. Resulting in equation A.2.

$$S(\tau, f_\eta) = A_0 p_r \left[\tau - \frac{2R_{rd}(f_\eta)}{c}\right] W_a(f_\eta - f_{\eta_c}) \exp\left[-j\frac{4\pi f_0 R_0}{c}\right] \exp\left[j\pi \frac{f_\eta^2}{K_a}\right]. \tag{A.2}$$

RCMC Since the range between radar and a single target changes over time due to the squint angle, targets appear to be moving in the range direction after each pulse. This is called range cell migration. Range Cell Migration Correction, corrects this offset such that the trajectory of target detection becomes parallel to the azimuth axis. After applying RCMC, the signal becomes;

$$S(\tau, f_\eta) = A_0 p_r \left[\tau - \frac{2R_0}{c}\right] W_a(f_\eta - f_{\eta_c}) \exp\left[-j\frac{2\pi f_0 R_0}{c}\right] \exp\left[j\pi \frac{f_\eta^2}{K_a}\right]. \tag{A.3}$$

Azimuth Compression In the azimuth direction, a second matched filter is applied for better focusing. This filter is given in equation A.4, it removes the second exponential term. After the filter equation A.3 becomes equation A.5.

$$H_{az}(f_\eta) = \exp\left(-j\pi \frac{f_\eta^2}{K_a}\right). \tag{A.4}$$

$$S(\tau, f_\eta) = A_0 p_r \left[\tau - \frac{2R_0}{c}\right] W_a(f_\eta - f_{\eta_c}) \exp\left[-j\frac{4\pi f_0 R_0}{c}\right]. \tag{A.5}$$

Azimuth IFFT Finally an IFFT is applied. This yields the final result in the time domain given in equation A.6.

$$s(\tau, \eta) = A_0 p_r \left[\tau - \frac{2R_0}{c}\right] \exp\left[-j\frac{4\pi f_0 R_0}{c}\right] \exp\left[j2\pi f_{\eta_c}\eta\right]. \tag{A.6}$$

The steps given above are the general approach to the RDA. There are a few different implementations of the algorithm. The steps remain the same but in some cases a Secundary Range Compression (SRC) is applied. This SRC is necessary for processing SAR images which were created with a larger squint angle.

A.2. Chirp Scaling Algorithm

The Chirp Scaling Algorithm (CSA) was mainly developed to bypass the long computational times needed for interpolation during RCMC in RDA [36]. Still RCMC is performed in a different manner to yield proper results. The processing steps for CSA are as follows.

1 Azimuth FFT

2 Chirp scaling for differential RCMC

3 Range FFT

4 Reference function multiply for bulk RCMC, RC and SRC

5 Range IFFT

6 Azimuth compression and phase correction

7 Azimuth IFFT

In the chirp scaling algorithm, the RCMC is split up in 2 different parts. The bulk RCMC takes the average correction necessary and applies this to all the cells. Although not all cells require the same correction. The difference between the bulk and the correction that each individual cell requires, is determined with chirp scaling. With this technique the differential RCMC is applied. Applying chirp scaling will avoid the need for interpolation as with RDA.

A.3. Omega-k Algorithm

The Omega-k Algorithm (ωkA) was developed since both RDA and CSA ignore range time dependence, which is negligible for small beam-widths, but not over large ones. Some more typical characteristics are;

- Able to process data over wide azimuth apertures
- Able to process data with high squint angles
- Assumes that the radar velocity is range invariant
- Unable to process data in large range swaths

Which has its advantages and disadvantages against RDA and CSA. There are 2 different versions of the ωKA, an accurate and approximate implementation. The approximate implementation replaces Stolt mapping with a phase multiply. An overview of the steps needed to perform accurate ωKA are;

1 Two-dimensional FFT

2 Reference function multiply (bulk compression)

3 Stolt mapping

4 Two-dimensional IFFT

The ωKA performs operations in the two-dimensional frequency domain, and starts with a two-dimensional FFT. The second step in the algorithm focuses on a selected range, usually midswath for convenience. A reference function multiply (RFM) is created which counters the phase at the corresponding reference range. This function takes frequency modulation and range cell migration into account. After the application of this reference function, the reference range is correctly focused. The rest of the image needs to be refined. This is done by the interpolation procedure called Stolt mapping. It performs the differential RCMC, SRC and azimuth compression

A.4. Backprojection

Backprojection requires a known location of the antennas with respect to the grid, also called a digital elevation map (DEM), unlike the frequency domain techniques. Frequency domain techniques do require information of the antenna location for motion compensation, but this is retreived from the radar information such that no other sources are required [33].

Among the different processing techniques in frequency and time domain, backprojection is the most straightforward solution to create an image. Backprojection can be described in a few global steps.

1 Determine grid and range to each resolution cell

2 Create a matched filter for each resolution cell

3 Apply the matched filter for each cell corresponding to the time delay in the received signal

4 Iterate steps 1 to 3 for each transmission

5 Sum each resolution cell

As can be derived from these steps, backprojection does not take Doppler into account in processing. To get a more in depth explanation of backprojection, lets first consider the transmitted signal.

$$s_t(t) = w(t)\exp\left(j2\pi f_0 t + j\pi K_r t^2 + j\phi_0\right). \tag{A.7}$$

Which corresponds to the transmitted signal in equation 3.6, but now complex and with the initial phase, ϕ_0. The time domain received signal for a single transmission can then be described as;

$$s_r(t) = A_c[t-t_c]G_c[t-t_c]w[t-t_c]\exp\left(j2\pi f_0(t-t_c) + j\pi K_r(t-t_c)^2 + j\phi_0\right). \tag{A.8}$$

Where t_c is the time delay corresponding to each resolution cell in the grid, A_c the corresponding amplitude term dependent on the area and G_c is the amplitude term dependent on antenna gains and propagation losses. The corresponding matched filter for each cell then becomes;

$$h_c(t) = G_c(t - t_c)\, w(t - t_c) \exp\left(-j2\pi f_0 t_c + j\pi K_r (t - t_c)^2\right). \tag{A.9}$$

The matched filter is applied on the demodulated received signal. Then the contribution of each pulse is taken as long as the cell is illuminated by the radar. The value that describes a single cell during the creation of the SAR image is,

$$I = \exp(j\phi_0) \sum_{c \in \mathcal{N}} \int A_n(\tau - t_c) G_c^2(\tau - t_c)\, w_c^2(\tau - t_c)\, d\tau. \tag{A.10}$$

This procedure is done for each cell in the grid, providing the complete image.

B

ISAR Backprojection

Backprojection is one of the most used algorithms in SAR due to its simplicity and performance. In ISAR, the backprojection algorithm can only be applied when the rotational characteristics of a target are known. When they are known, ISAR time domain backprojection can be applied by following these steps:

- Create a grid
- Determine rotation rate of the target
- Rotate the grid at the same rotation rate as the target
- Apply the FFT over received signal
- Add the magnitude of the beat frequencies to the corresponding range bins
- Sum over all the measurements

Simulation To demonstrate the behavior of the backprojection algorithm, a simple simulation is created. The simulation is done in the 2D plane using a few point scatterers. The simulation parameters are shown in table B.1. A target consisting of 2 point scatterers rotates around the origin while the radar measures the rotation on a distance of 10 meters. This does not uphold the far-field criteria, but for the sake of simplicity in the simulation this is ignored.

Radar Parameters		Target Parameters		
Fc	9 GHz	Rotation speed	1800 degrees/s	
B	500 MHz	x	-0.5 m	0.8 m
T	1 ms	y	-0.3 m	0.8 m
Fs	40 MHz			
Npulses	200			
x	5 m			
y	0			

Table B.1: Simulation parameters

In this simulation a comparison will be shown between 2 cases. In the first case, Doppler will not be taken into account. Assuming that the scatterers 'teleport' to their new location at each pulse. In the second case Doppler will be considered to show the impact. The number of pulses and the rotation speed are set such that both scatterers will complete one rotation around the center point.

Target The measured signal caused by the 2 moving point scatterers is directly computed with the demodulated signal as given in equation 2.7. After this calculation the retrieved signals of the scatterers are summed.

Grid A square grid is created around the origin from -1x,-1y to 1x,1y. The grid contains 100000 grid cells. It is important to note that the resolution of the image is limited by equation 3.10. However, a higher number of grid cells improves the smoothness of the image.

Result The result of the simulation with no Doppler added is shown in figure B.1. The first subfigure shows the demodulated time signal for a single chirp. In this chirp, the 2 targets are at a different distance from the radar, causing 2 different beat-frequencies as can clearly be seen in the figure.

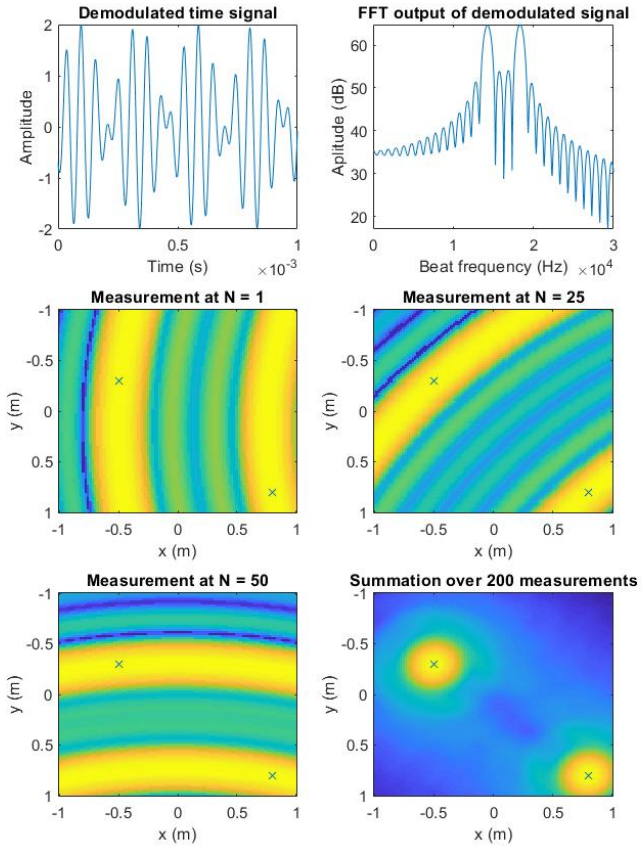

Figure B.1: ISAR backprojection simulation result

The second subfigure shows the FFT of the demodulated time signal. Zero padding and a hamming window have been applied to improve the quality of the frequency domain output.

In the following 3 subfigures, the imaging grid is shown for different time indices. Consider the imaging grid of N = 1. Keep in mind that the radar is located at x = 5 m, to the right of the image. The target locations are indicated as small crosses. In a single measurement, the radar is unable to determine the angle of arrival of both the targets. Thus, the targets are mapped as a circle around the radar, corresponding to the distance between the radar and target. As the targets rotate, their distance to the radar changes. But since the grid is rotating along, the targets do not leave their position in the grid, although the grid turns with respect to the radar. This is clearly shown in the images of measurements N = 25 and N = 50.

The last subfigure shows the summation over all the 200 measurements. Showing the locations of both targets in the imaging grid.

Doppler When velocity is taken into account, the delay to the target becomes time-dependent.

$$\tau = \frac{2(R + v(t)t)}{c}. \tag{B.1}$$

This dependence has an impact on the demodulated signal.

$$s_m(t) = \frac{1}{2}\cos\left(2\pi(f_c\tau + k\tau t - \frac{k\tau^2}{2})\right). \tag{B.2}$$

This equation shows that when τ becomes time-dependent, the factors that were phase changes before become frequencies. Apart from that, the beat frequency changes over time.

Since backprojection is based on knowledge of the target, the rotational speed must be known to perform it. And when the rotational speed is known, these Doppler offsets can also be cancelled by computing the matching beat-frequency for each grid cell.

To determine the new beat-frequency, equation B.1 is filled in B.2. This gives the following equation.

$$s_m(t) = \cos\left(2\pi\left(\left(f_c\frac{2v(t)}{c} + \frac{2kR}{c} + \frac{2kv(t)t}{c} - \frac{2kv^2(t)t}{c^2} + \frac{2kRv(t)}{c^2}\right)t + f_c\frac{2R}{c} - \frac{k2R^2}{c^2}\right)\right). \tag{B.3}$$

Equation B.3 shows 4 new frequency terms that are added to the original beat-frequency. The final 2 time dependent terms include a division of the light speed squared and are negligibly small. The Doppler frequency is commonly defined as;

$$f_d = \frac{2vf_c}{c}. \tag{B.4}$$

When the signal is processed without compensating the Doppler in the imaging grid, large errors occur. In figure B.2 it is shown that without Doppler compensations the target locations can not be retrieved.

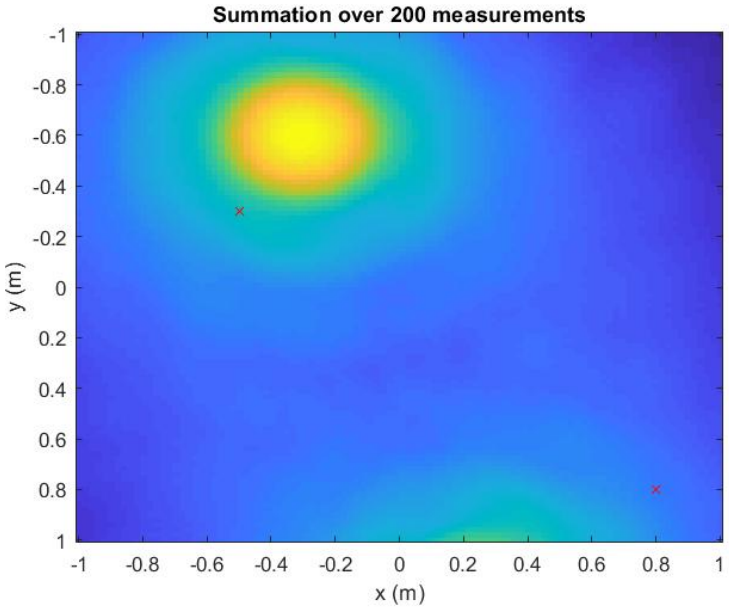

Figure B.2: ISAR backprojection with uncompensated Doppler

To compensate for the Doppler mismatch, the time dependent range bins of the imaging grid need to take into account shifting due to Doppler. This can be done by considering the new beat-frequency, where the terms including $\frac{1}{c^2}$ have been discarded.

$$\omega_b = \frac{f_c 2v(t) + 2kR + 2kv(t)t}{c}. \tag{B.5}$$

Since both the beat-frequency and velocity are known, the range can be expressed in terms of these;

$$R = f_b \frac{c}{2k} - f_c \frac{v}{k} - vT. \tag{B.6}$$

Since the velocity does not change rapidly over time, the mean value can be taken of the velocity to make R independent of fast time. This compensation is applied to each grid cell, which yields a better result as shown in figure B.3.

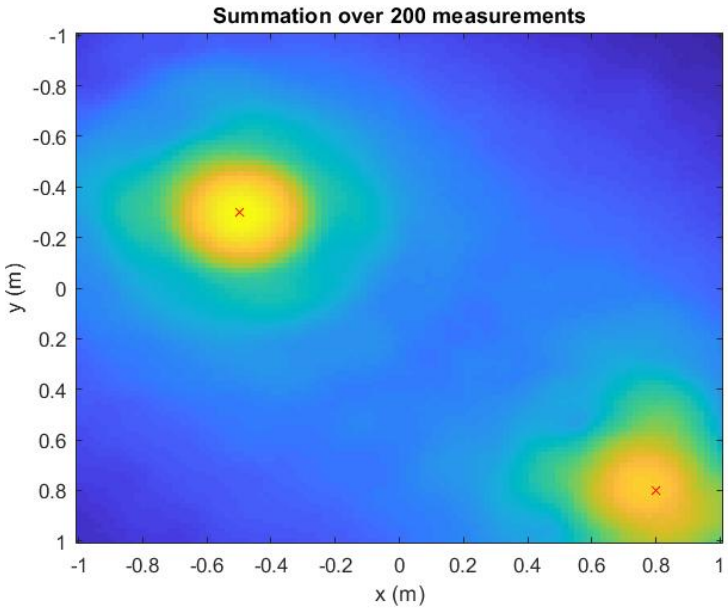

Figure B.3: ISAR backprojection with compensated Doppler

C

Pre-Processing

Target detection is done based on reflected power from certain AOA. The procedure is as follows.
When a target occupies a certain position at an angle θ with respect to the normal of the radar, while measuring in the far-field, the range offset of the target to the different receivers is described as;

$$r_d = \frac{\lambda}{2}\sin\theta. \tag{C.1}$$

As long as the distance between the receivers is;

$$r_r = \frac{\lambda}{2}. \tag{C.2}$$

Then the phase offset for receiver n is given as;

$$\phi_{dn} = 2\pi f_c \frac{r_d}{c} n = \pi \sin(\theta)(n-1). \tag{C.3}$$

And the demodulated signal perceived by receiver n is described as;

$$S_n(f,t) = \exp\left(i\frac{4\pi}{c}(f+fc)\left(r_n + \dot{r}_n t + \frac{\ddot{r}_n}{2}t^2\right) - i\phi_{dn}\right). \tag{C.4}$$

The data-set, now containing real valued data in 3 dimensions (slow time, fast time, sensors) is converted to the slow-time-angle domain. This is done by taking an FFT in the sensor direction, while considering a single pulse.

$$S_{at}(r,\theta) = \mathfrak{F}(S_n(f,t)). \tag{C.5}$$

It is important to taken into account that the received angles are not linearly spaced. The actual AOA can be found as;

$$\theta_{AOA} = \arcsin(\theta). \tag{C.6}$$

Just using the Fourier transform is not enough to clearly distinguish the targets from the background and each other. A moving average filter is used to smooth the targets in the slow-time dimension, making each one more coherent.

$$c_m = \frac{(c_{m-n/2} + c_{m-n/2+1} \ldots + c_{m+n/2})}{n}. \tag{C.7}$$

Where c_m is the considered cell and n is the number of cells taken into account. After the moving average filter the complete data-set is normalized. Since targets closer to the radar can contain more power than the targets far from the radar have in their main lobe, CFAR windowing is applied to clearly distinguish targets from the background noise.

Figure C.1 shows the evolution from the raw FFT signal to after the CFAR detection. As long as it is unknown how many ships are present, it is difficult to tell which reflections are from ships and which are from

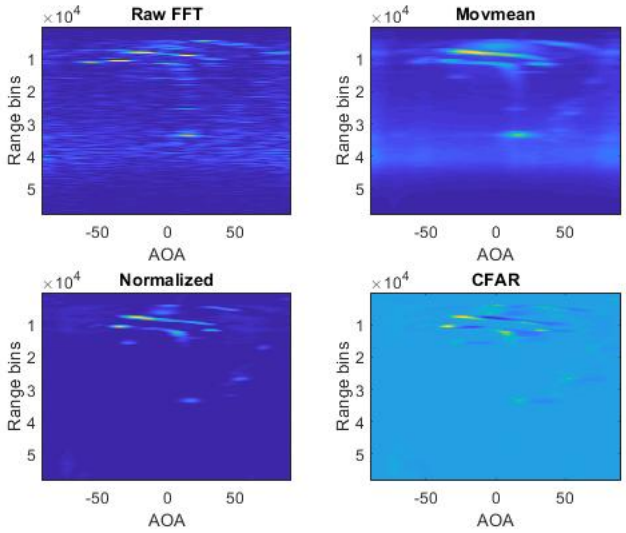

Figure C.1: Data pre-processing results to effectively detect targets and estimate their AOA

waves. In this case in particular, there are a lot of ships contained in the same range bins, making the probability of missed detection higher.

To detect the locations of the different targets a variation on the CLEAN algorithm is used [37]. The algorithm is performed in the following steps.

- A threshold is set which equals the minimum power a target may reflect.
- The maximum value of the complete image is located, if it is above the threshold, the location is stored as a target.
- The neighbouring cells are checked if they exceed the threshold.
- This procedure is repeated for neighbours until all edges of the 'target' are below the threshold.
- This form containing values above the threshold is removed from the image.
- The procedure is repeated until there are no more values which exceed the threshold.

Figure C.2 shows the located targets in the image with their maximum reflection point indicated as a red cross. It is important to note that some targets are extended quite far in the AOA dimension (also azimuth). It should be considered that the accuracy of AOA estimation may not be good enough, causing the sharp beam to miss the target.

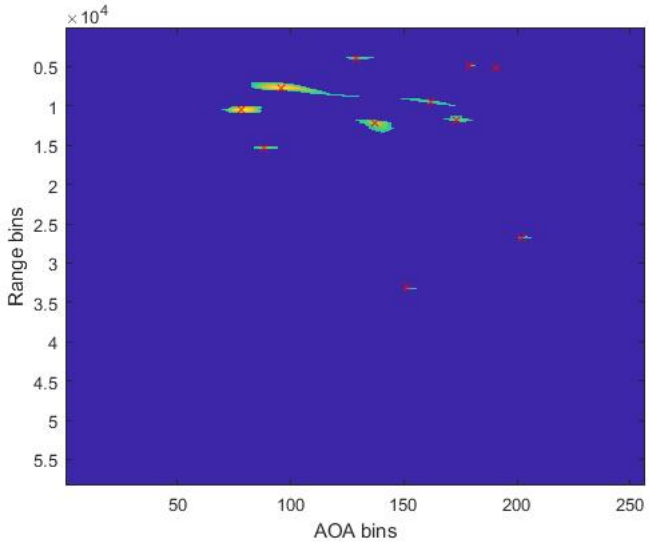

Figure C.2: Targets found in the raw dataset by applying CFAR detection and adjusted CLEAN

D

Design Methods

Generating the image can be done in many different ways. To give an idea of which trade-offs are important, 6 different methods are proposed. These methods are shown in figure D.1 and will be discussed individually. It should be noted that these methods do not contain all possible options and that it is possible to combine some of the methods.

Method 1 This is the most straightforward and brute-force method of all the methods which are mentioned. The idea is to 'try' all possible angles by steering the beam over the data-set. In this manner, the targets can be detected relatively easily since they are at some point illuminated at their exact location, giving a strong reflection. The acceleration of the target can be compensated by an iterative procedure which tries different accelerations and checks the image quality. Although this method is probably the least error-sensitive, it is also extremely computationally expensive given the large data-set.

Method 2 To avoid the scanning procedure as performed on the angles in Method 1, this method uses angle of arrival estimation to determine at which angles targets are located. Hereafter the beam can be steered to the relevant angles and beam forming only needs to be performed for each individual target. This method will be faster, but may also suffer from errors in the AOA estimation.

Method 3 To speed up the algorithm some more, the acceleration parameter for each individual target can be estimated in an earlier stage. And can later on be compensated directly without the need for an iterative solution.

Method 4 An alternative way to suppress clutter is to apply the displaced phase centre antenna (DPCA) technique. It involves steering multiple beams on the target from different locations in the same time instance. Subtracting both measurements from each other will remove stationary targets. Whether this will be applicable at sea is uncertain since the surroundings of the targets will be moving as well.

Method 5 To evade the need to use beam forming on the entire data-set, an adaptive beam forming technique is proposed. Beam forming can be done only on the relevant range bins which contain the corresponding target. Here the keystone algorithm will be applied on a cropped dataset

Method 6 The keystone transform can also be applied in an earlier stage. Although this procedure avoids the use of keystone on a cropped image, the transform will now have to be performed on each individual receiver.

Method selection

Determining the most effective algorithm structure is done based on several important conditions.

- First and most important, the algorithm should create an ISAR image which clearly distinguishes features of the target.

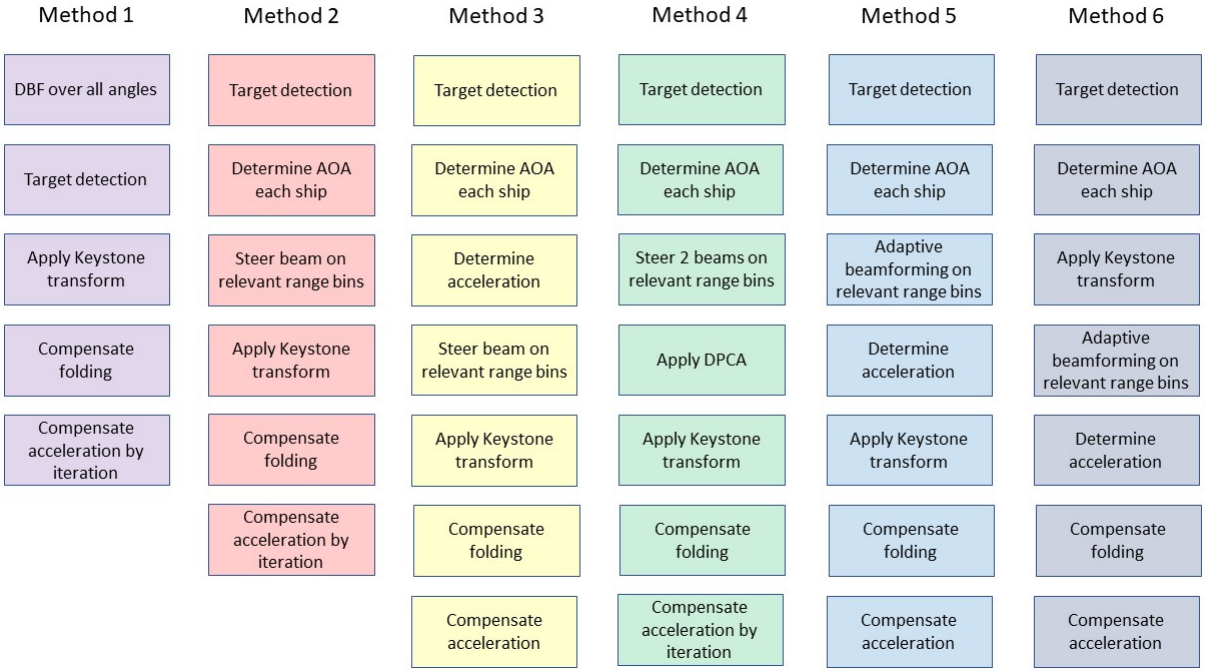

Figure D.1: Different methods on how the ISAR image can be generated given a data set which contains raw data

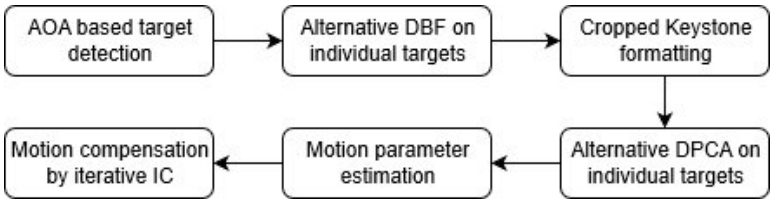

Figure D.2: Flow chart of the algorithm application method which will be evaluated in practice

- This first point is constrained by the limited processing capabilities of the system.
- The final product should be a genuine algorithm which does not solely depend on methods which are already known. There is room for improvements to increase the performance in terms of image-quality.

Based on these confinements, a new combined method is found which will be applied in practice. A flow chart of the chosen method is shown in figure D.2. Each subcomponent of this scheme will be discussed individually.

AOA based target detection

This block contains a function that both detects targets and estimates their location. Detecting moving targets at sea is different than on land. Standard techniques as CFAR detection or STAP have issues due to the moving and varying sea surface. Especially with small, slow moving targets, which show similar Doppler spectra as the waves which carry them [38–40]. In order to circumvent this problem, many techniques have been developed to estimate and/or suppress the sea clutter [41–44].
The target detection itself is not exactly aligned with the end goal of this thesis. A target detection algorithm is set up as a preprocessing step. The target detection is performed in the range-angle domain. Such that with the detection, an estimation of the target's location can immediately be performed.

DBF on individual targets

Although in some literature a scanning procedure of the digital receive array, such as in *Method 1*, is used [45], this comes at the cost of computational resources. Especially in a dense sea environment [46]. To image dif-

ferent ships from different AOA, DBF has to be applied on the complete data-set repeatedly, which is a heavy operation on such a large data set.
To limit the computational load, DBF can be applied to a small part of the data-set in range direction. Considering only the range-bins which cover the target. By aiming the digital-beam towards a target, a lot of clutter from other directions is already suppressed. On top of this, standard techniques such as windowing can be applied to improve the SNR even more. Furthermore, techniques which steer nulls in the direction of unwanted strong clutter (secondary targets or interference) can be used to increase the image quality [47].

Cropped Keystone formatting

As mentioned in [48], motion compensation is usually applied for a single target and generally the keystone algorithm is applied to the complete image. But since an individual beam is aimed at each target separately, applying the Keystone algorithm will need to be done differently. Two different solutions to the problem exist. Either first apply the Keystone algorithm to each individual receiver and then do beam forming, or first apply beam forming and apply Keystone to each individual target.
As mentioned before the received data is cut in smaller segments each containing a limited amount of range-bins which hold information on the target. As the keystone is an interpolation filter, it can also be applied on these range cropped data-pieces. Even without the use of the fast keystone transform [30], the computational load of the algorithm drops significantly by this cropped keystone procedure.

DPCA on individual targets

DPCA is a well known technique which uses two or more antenna sub arrays to simulate a stationary radar on a moving platform. The first sub array measures from location x at t_0 and as the platform moves, the second sub array reaches location x, measuring at t_1. Subtracting two sub arrays from each other will remove all the stationary components in the image, as their reflection did not change over time.
Although this algorithm is quite useful to image moving targets on the ground, the difficulty for this project lies with the moving ocean surface. As there are no stationary targets, they can not be filtered. Therefore an alternative technique was created considering the motion of the ocean. An additional phase shift was estimated and added to compensate for moving waves in the ocean. The technique is called the Oceanic Displaced Phase Center Antenna (ODPCA) technique [27].
As an alternative to the ODPCA, a new method is proposed which forces the target to be stationary and then filters all non-stationary targets. In chapter 7 the performance of the different DPCA approaches are discussed. The choice of approach for DPCA will be done dependent on the performance results.

Motion parameter estimation

When applying the first order Keystone transform, velocity is compensated within the ambiguous limits. An estimation still needs to be made to determine the correct folding factor. Apart from this, an estimation and compensation for the acceleration needs to be done as well.
A first crude estimation of the velocity and acceleration can be done solely on the motion characteristics of the areal vehicle carrying the radar. Consecutive estimation can be done based on sparse measurement target tracking.

Motion compensation by IC minimization

Applying the motion compensation is simply done by using the equations for the Keystone algorithm. However the estimation on acceleration does only depend on the radar motion and will thus not be very accurate. To determine the correct acceleration component a simplified version of the image contrast maximisation technique used in [19] is used. Although the image contrast function is a good performance indicator for the general filtering procedures, it is not as effective when evaluating the performance of clutter suppression techniques.

E

Subcomponent Contribution

To verify the contributions of the individual subcomponents a performance evaluation is performed on the subcomponents which are crucial for the algorithm. This will be done based on real-measured data. The radar settings during the measurement are given in table E.1. Two targets are considered, having different clutter characteristics:

- Target 1 has medium range and medium clutter
- Target 2 has medium range and low clutter

Single receiver

To evaluate the impact of each individual processing step, first consider the most simple imaging scheme. With this a single receiver with no motion compensation, windowing or other processing techniques is assessed. Figure E.1 shows the range Doppler image for the 2 given targets. Evidently, the targets are unrecognisable due to clutter and motion distortion. Note that for all figures given in this section, normalization is applied on the range Doppler images according to the strongest back-scatterer.

Multiple receivers

In the second stage of this evaluation process, the impact of adding more receivers and velocity compensation is assessed. Figure E.2 shows the different range Doppler images for 1, 8, 16 and 24 receivers where only the foldover correction for Keystone is applied and no acceleration compensation.

Motion compensation

The effect of applying the acceleration compensation is shown in figure E.3. This final step in the motion compensation procedure greatly increases the image quality, making the ships distinguishable from their surroundings. The acceleration compensation is performed by image contrast maximization. For the two different targets, the image contrast is plotted versus a parameter sweep on acceleration. The results are

Parameter	Value
Carrier Frequency	9.45 GHz
Bandwidth	1 GHz
PRF	301.2 Hz
Number of sweeps	304
Sampling Frequency	19.44 MHz
Array Size	24
Element Distance	$\frac{\lambda}{2}$

Table E.1: AMBER parameters

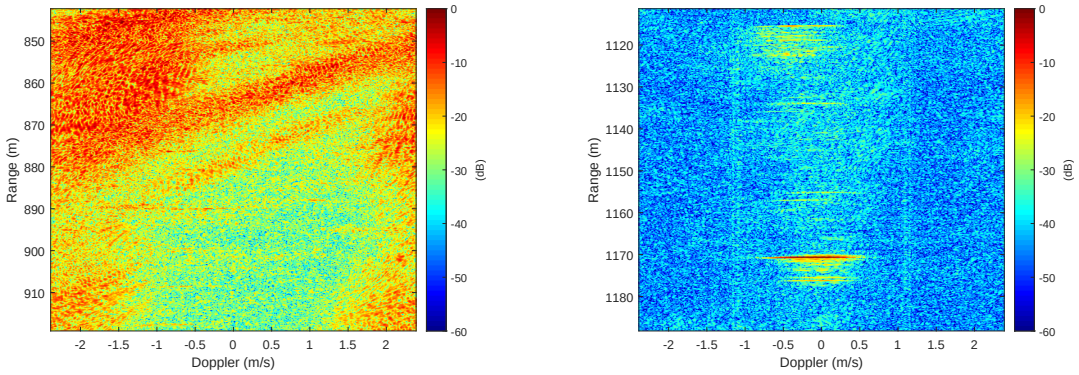

(a) Target 1

(b) Target 2

Figure E.1: Range Doppler image of 2 different targets without any further processing

	Target 1	Target 2
1 receiver VC	0.8935	1.8695
8 receivers VC	1.3556	3.1487
16 receivers VC	1.5972	3.7476
24 receivers VC	1.7523	3.9537
AC	2.4472	5.1700
Windowing	3.1305	6.6934
Without Keystone	3.0774	6.4213

Table E.2: IC values for both targets at different stages in the basic processing chain

shown in figure E.4. This shows that there is a clear optimum for the acceleration estimation, that is, the actual acceleration of the target relative to the radar position.

Windowing

After motion compensation is applied, a Blackman window in slow time and a hamming window in fast time are tested on the image. The result of these windowing functions is shown in figure E.5.
To get a different idea of how the images have improved, the IC has been computed for all cases in this section and is given in table E.2. Where VC stands for Velocity Compensation and AC for Acceleration Compensation The table also indicates what the IC is when the Keystone transform is not applied.

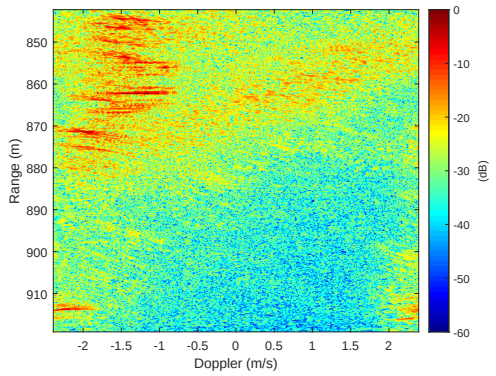

(a) Target 1 - 1 receiver

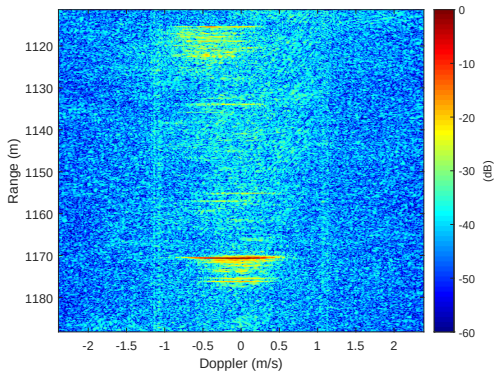

(b) Target 2 - 1 receiver

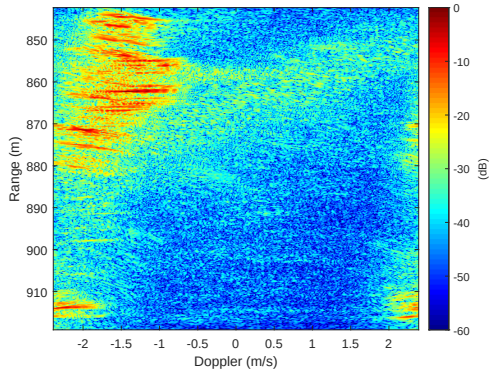

(c) Target 1 - 8 receivers

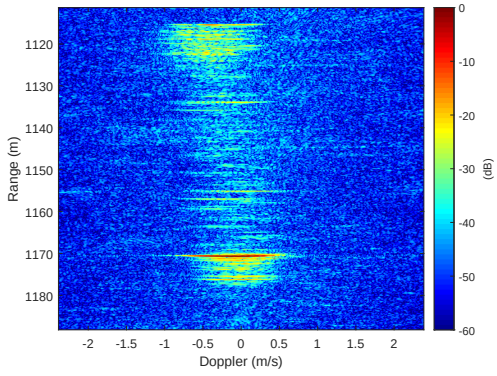

(d) Target 2 - 8 receivers

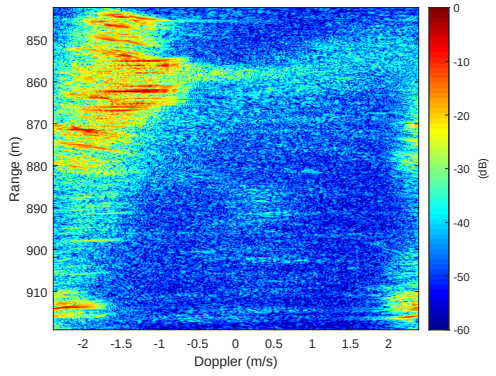

(e) Target 1 - 16 receivers

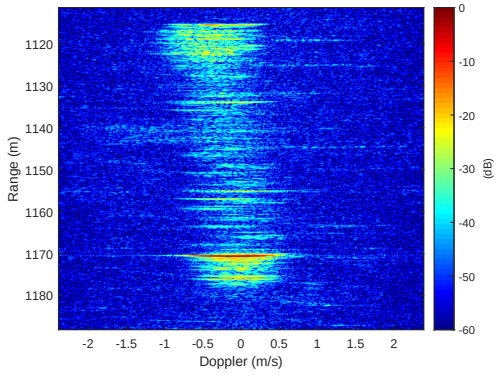

(f) Target 2 - 16 receivers

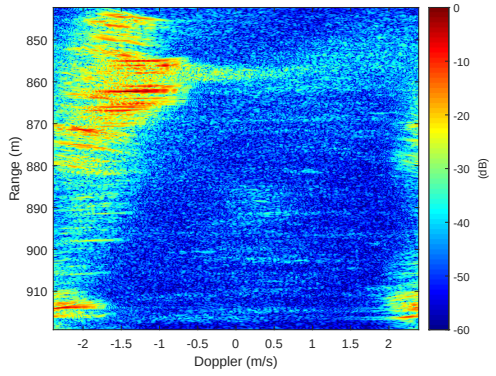

(g) Target 1 - 24 receivers

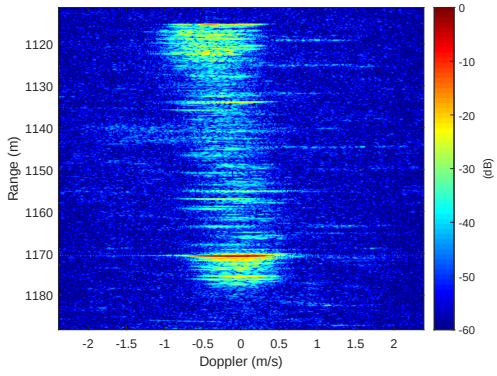

(h) Target 2 - 24 receivers

Figure E.2: Range Doppler image of 2 different targets with varying array sizes after velocity compensation

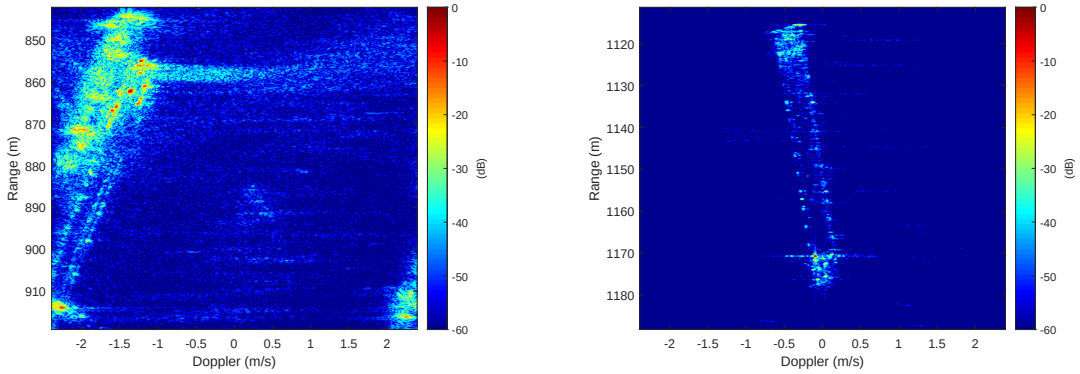

(a) Target 1 (b) Target 2

Figure E.3: Range Doppler image of 2 different targets after motion compensation

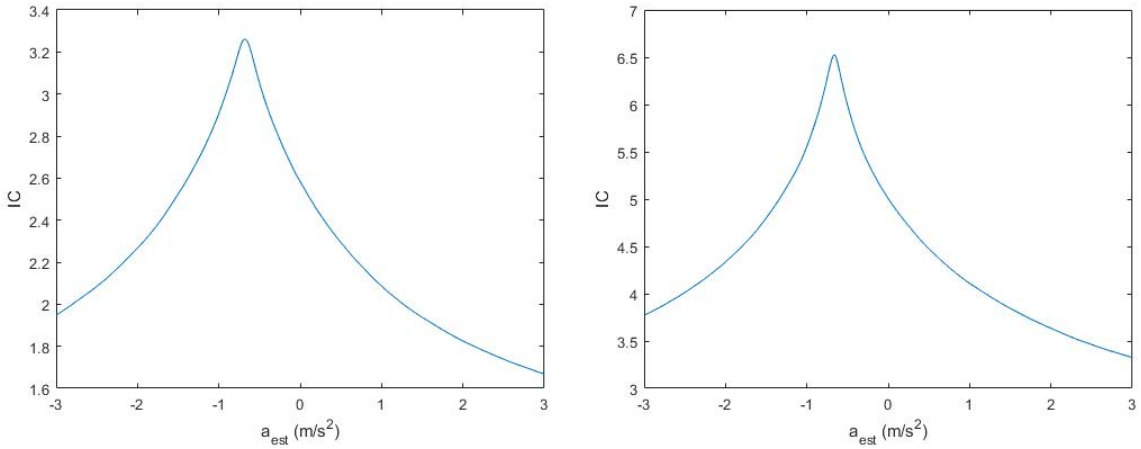

(a) Target 1 (b) Target 2

Figure E.4: Image contrast function versus acceleration estimation

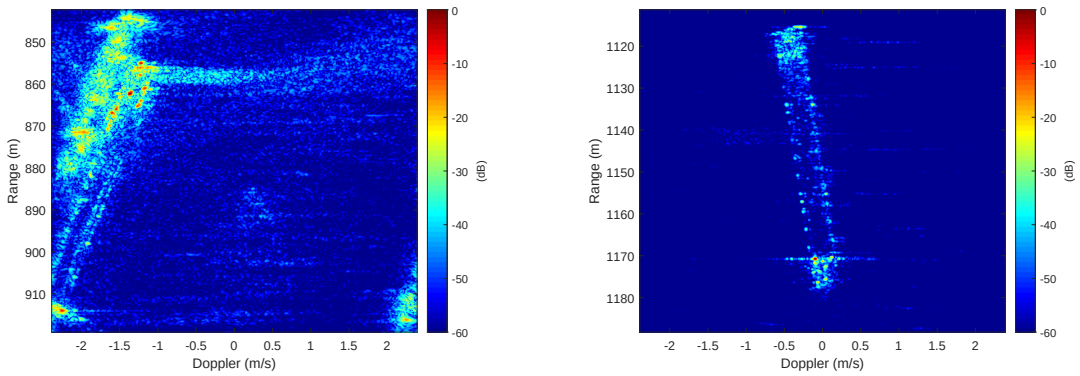

(a) Target 1 (b) Target 2

Figure E.5: Range Doppler image of 2 different targets after motion compensation and windowing

F

AOA Estimation by Phase Variance

As the AOA is related to the phase variance, there could be a possibility to exploit this to estimate the AOA. This chapter discusses the limitations and possibilities of this approach for non overlapping sub arrays.

The relation between AOA and phase variance is different for non overlapping sub arrays than for overlapping sub arrays. This is shown for 3 different sub array sizes in figure F.1. This figure also shows an important artefact which should be discussed. When there are less sub arrays, there appear more grating lobes. Such that the value of the circular variance becomes ambiguous. Meaning, that a value for the circular variance of zero will not necessarily mean that this object is at the considered AOA.

However, this phenomenon is greatly cancelled out by beam forming. When there are less sub arrays, there are more ambiguities, but the beam is focussed more as well. Due to this effect, the clutter from ambiguities is attenuated and does not dominate the variance in its pixels. Very strong clutter could theoretically still trump this and be mistaken as the target. Due to this effect, the choice to use 8 sub arrays of 3 receivers is substantiated even more due to the small amount of grating lobes.

Nevertheless, figure F.1 shows that with non overlapping sub arrays AOA estimation only based on the phase variance of clutter is very difficult. Clutter may have a very clearly defined phase variance, but this value is ambiguous for a lot of different angles.

A solution to this problem is to sweep the beam over θ and measure at each angle how many pixels have a circular variance lower than the threshold, in other words, a target. When applying this technique, consider the following points;

- When a target is located in the beam, the number of pixels that are below the threshold relate to the size of the target.
- If motion compensation is not applied on a target, it is focussed less and more susceptible to get lost in noise above the phase variance threshold level. However, if the target trumps the noise while being unfocussed, it will appear larger than it is.
- If motion compensation is applied to a target, the chance that the target is below the threshold is higher. But the number of pixels that correspond to the target will also be less.
- Applying motion compensation to every angle corresponds to imaging and focussing at each angle. This results in a very high computational load.
- Even when no motion compensation is applied at all, a target could still become focussed if it shows a foldover factor, relative velocity and relative acceleration of zero.

This approach is applied for several different ranges while considering all the possible combinations of sub arrays. The considered range gates are: 740 m - 820 m, 840 m - 920 m, 1110 m - 1190 m. The results of the sweep on theta for these range gates are shown in figure F.2. From the figures the AOA of different targets can be distinguished. In figure F.2b, motion compensation has been applied to focus on the target at 18 degrees.

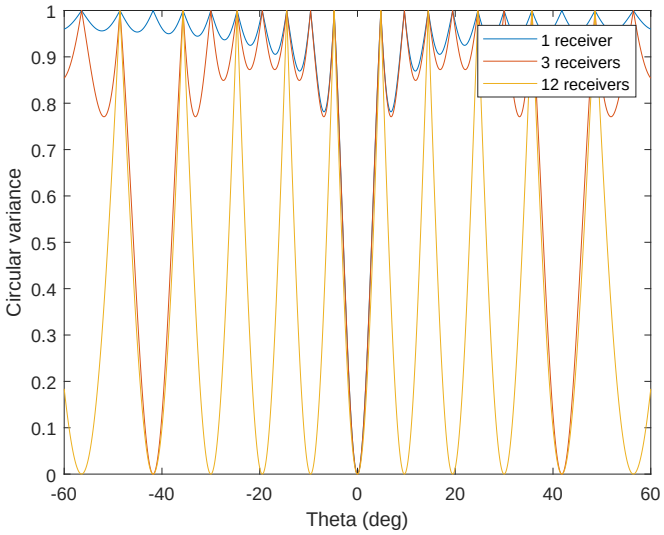

Figure F.1: Relation between circular variance and AOA for non overlapping sub arrays

On the contrary, figure F.2c shows the targets while no motion compensation is applied. As was expected, the unfocussed figure gives a higher peak as the target is more spread in the image. However, it is not possible to distinguish the two targets at 18 and 23 degrees from each other when motion compensation is not applied.

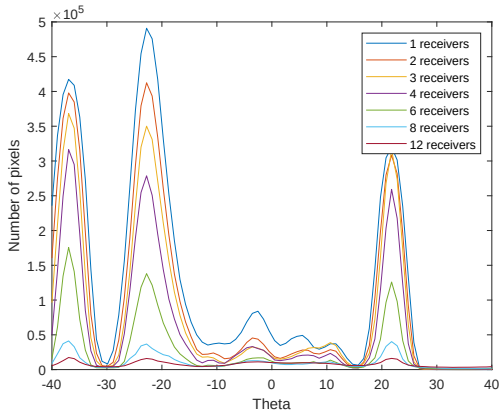

(a) Unfocussed range gate 740-820 m

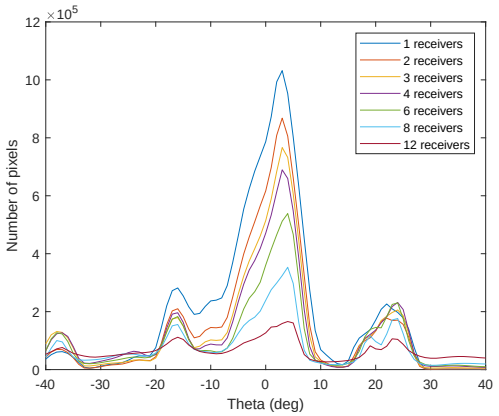

(b) Focussed range gate 840-920 m

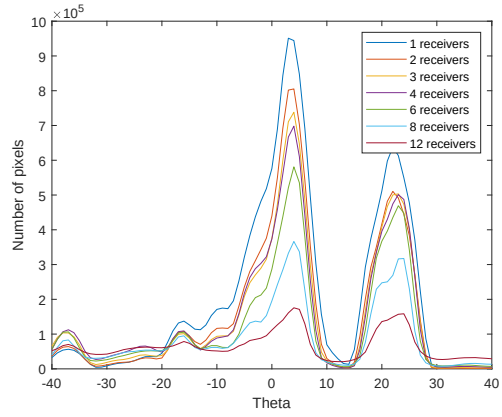

(c) Unfocussed range gate 840-920 m

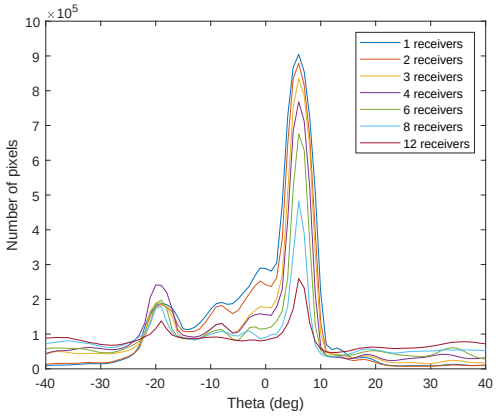

(d) Focussed range gate 1110-1190 m

Figure F.2: Number of pixels below phase variance threshold for angle sweep of θ

G

Measurement Layout

Figure G.1: Locations of different targets

Bibliography

[1] Y. K. Chan and V. C. Koo, "An introduction to synthetic aperture radar (sar)," *Progress In Electromagnetics Research B*, vol. 2, pp. 27–60, 2008.

[2] M. Grissa, R. Abdelfattah, G. Mercier, M. Zribi, A. Chahbi, and Z. Lili-Chabaane, "Empirical model for soil salinity mapping from sar data," in *2011 IEEE International Geoscience and Remote Sensing Symposium*, July 2011, pp. 1099–1102.

[3] M. Otten, W. v. Rossum, M. v. d. Graaf, W. Vlothuizen, and R. Tan, "Multichannel imaging with the amber fmcw sar," in *EUSAR 2014; 10th European Conference on Synthetic Aperture Radar*, June 2014, pp. 1–4.

[4] T. Yang, L. Yang, G. Bi, and Y. Wang, "A novel wide area multiple azimuth beam isar imaging system," *IEEE Access*, vol. 7, pp. 65 277–65 287, 2019.

[5] G. M. Herbert, "Modelling of phase noise from frequency references in bistatic radar," *IMA Conference on Mathematics in Defence*, 2015.

[6] S. Suleymanov, "Design and implementation of an fmcw radar signal processing module for automotive applications," Master's thesis, Univerity of Twente, 8 2016.

[7] F. H. W. Ian G. Cumming, *Digital processing of synthetic aperture radar data algorithms and implementation*. Artech House, 2005.

[8] A. Meta, P. Hoogeboom, and L. P. Ligthart, "Signal processing for fmcw sar," *IEEE Transactions on Geoscience and Remote Sensing*, vol. 45, no. 11, pp. 3519–3532, Nov 2007.

[9] M. M. Chen, Victor C., *Inverse Synthetic Aperture Radar Imaging: Principles, Algorithms and Applications*. Institution of Engineering and Technology, 2014. [Online]. Available: https://app.knovel.com/hotlink/toc/id:kpISARIPA1/inverse-synthetic-aperture/inverse-synthetic-aperture

[10] J.-I. Park and K.-T. Kim, "A comparative study on isar imaging algorithms for radar target identification," *Progress In Electromagnetics Research*, vol. 108, pp. 155–175, 01 2010.

[11] F. Su, Y. Su, and J. Gao, "Range doppler imaging for lfmcw isar based on azimuth interpolation," in *2012 IEEE 11th International Conference on Signal Processing*, vol. 3, Oct 2012, pp. 2048–2052.

[12] L. Mingjing, G. Meiguo, and F. Xiongjun, "A novel range alignment algorithm for real time isar imaging," in *2006 8th international Conference on Signal Processing*, vol. 4, Nov 2006.

[13] J. Xue and L. Huang, "An improved cross-correlation approach to parameter estimation based on fractional fourier transform for isar motion compensation," in *2015 IEEE International Conference on Acoustics, Speech and Signal Processing (ICASSP)*, April 2015, pp. 1538–1542.

[14] J. Xue, X. Han, and Q. Zhang, "A symmetric accumulated cross-correlation method of parameter estimation based on fractional fourier transform for isar motion compensation," in *2017 9th International Conference on Wireless Communications and Signal Processing (WCSP)*, Oct 2017, pp. 1–6.

[15] Xi Li, Hongbo Sun, Hong Gu, Weimin Su, and Guosui Liu, "A new kind of isar autofocusing technique based on entropy criteria," in *WCC 2000 - ICSP 2000. 2000 5th International Conference on Signal Processing Proceedings. 16th World Computer Congress 2000*, vol. 3, Aug 2000, pp. 1806–1809 vol.3.

[16] Q. Zhang, Y. Chen, Y. Wu, and D. Wang, "A seaborne isarautofocusing method under minimum entropy criterion," in *IGARSS 2018 - 2018 IEEE International Geoscience and Remote Sensing Symposium*, July 2018, pp. 3543–3546.

[17] Daiyin Zhu, Ling Wang, Qingnian Tao, and Zhaoda Zhu, "Isar range alignment by minimizing the entropy of the average range profile," in *2006 IEEE Conference on Radar*, April 2006, pp. 6 pp.–.

[18] C. E. Shannon, "A mathematical theory of communication," *The Bell System Technical Journal*, vol. 27, no. 3, pp. 379–423, 7 1948. [Online]. Available: https://ieeexplore.ieee.org/document/6773024/

[19] M. Martorella, F. Berizzi, and B. Haywood, "Contrast maximisation based technique for 2-d isar autofocusing," *IEE Proceedings - Radar, Sonar and Navigation*, vol. 152, no. 4, pp. 253–262, Aug 2005.

[20] D. Xiong, J. Wang, H. Zhao, and M. Gao, "Modified polar format algorithm for isar imaging," in *IET International Radar Conference 2015*, 2015, pp. 1–7.

[21] F. Uysal and N. Goodman, "The effect of moving target on range-doppler map and backprojection algorithm for focusing," in *2016 IEEE Radar Conference (RadarConf)*, May 2016, pp. 1–5.

[22] R. P. Perry, R. C. DiPietro, and R. L. Fante, "Coherent integration with range migration using keystone formatting," in *2007 IEEE Radar Conference*, April 2007, pp. 863–868.

[23] D. Kirkland, "Imaging moving targets using the second-order keystone transform," *IET Radar, Sonar Navigation*, vol. 5, no. 8, pp. 902–910, Oct 2011.

[24] D. Zhu, Y. Li, and Z. Zhu, "A keystone transform without interpolation for sar ground moving-target imaging," *IEEE Geoscience and Remote Sensing Letters*, vol. 4, no. 1, pp. 18–22, Jan 2007.

[25] C. A. Balanis, *Antenna Theory: Analysis and Design*. USA: Wiley-Interscience, 2005.

[26] T. S. Kiong, S. B. Salem, J. K. S. Paw, K. P. Sankar, and S. Darzi, "Minimum variance distortionless response beamformer with enhanced nulling level control via dynamic mutated artificial immune system," *The Scientific World Journal*, vol. 2014, pp. 1–9, 2014. [Online]. Available: https://doi.org/10.1155/2014/164053

[27] G. Gao, K. Huang, S. Gao, J. He, and X. Zhang, "Ship detection based on oceanic displaced phase center antenna technique in along-track interferometric sar," *IEEE Journal of Selected Topics in Applied Earth Observations and Remote Sensing*, vol. 12, no. 3, pp. 788–802, March 2019.

[28] H. Liu, S. Shah, and W. Jiang, "On-line outlier detection and data cleaning," *Computers and Chemical Engineering*, vol. 28, pp. 1635–1647, 08 2004.

[29] T. Samajdar and M. I. Quraishi, "Analysis and evaluation of image quality metrics," in *Information Systems Design and Intelligent Applications*, J. K. Mandal, S. C. Satapathy, M. Kumar Sanyal, P. P. Sarkar, and A. Mukhopadhyay, Eds. New Delhi: Springer India, 2015, pp. 369–378.

[30] D. Zhu, Y. Li, and Z. Zhu, "A keystone transform without interpolation for sar ground moving-target imaging," *IEEE Geoscience and Remote Sensing Letters*, vol. 4, no. 1, pp. 18–22, Jan 2007.

[31] C. L. Dolph, "A current distribution for broadside arrays which optimizes the relationship between beam width and side-lobe level," *Proceedings of the IRE*, vol. 34, no. 6, pp. 335–348, June 1946.

[32] F. H. Allen and O. Johnson, "Automated conformational analysis from crystallographic data. 4. Statistical descriptors for a distribution of torsion angles," *Acta Crystallographica Section B*, vol. 47, no. 1, pp. 62–67, Feb 1991. [Online]. Available: https://doi.org/10.1107/S0108768190010382

[33] M. I. Duersch, "Backprojection for synthetic aperture radar," *All Theses and Dissertation*, vol. 4060, 2013.

[34] J. J. M. de Wit, "Development of an airborne ka-band fm-cw synthetic aperture radar," Ph.D. dissertation, TU Delft, 9 2005.

[35] Y. L. Neo, F. H. Wong, and I. G. Cumming, "Processing of azimuth-invariant bistatic sar data using the range doppler algorithm," *IEEE Transactions on Geoscience and Remote Sensing*, vol. 46, no. 1, pp. 14–21, Jan 2008.

[36] R. K. Raney, H. Runge, R. Bamler, I. G. Cumming, and F. H. Wong, "Precision sar processing using chirp scaling," *IEEE Transactions on Geoscience and Remote Sensing*, vol. 32, no. 4, pp. 786–799, July 1994.

[37] J. A. Högbom, "Aperture Synthesis with a Non-Regular Distribution of Interferometer Baselines," *aaps*, vol. 15, p. 417, Jun 1974.

[38] Jian Wang, R. L. Kirlin, Xiaoli Lu, and R. Dizaji, "Small ship detection with high frequency radar using an adaptive ocean clutter pre-whitened subspace method," in *Sensor Array and Multichannel Signal Processing Workshop Proceedings, 2002*, Aug 2002, pp. 92–95.

[39] S. D. Blunt, K. Gerlach, and J. Heyer, "Non-coherent detection of slow-moving targets in high-resolution sea clutter," in *Proceedings of the 2004 IEEE Radar Conference (IEEE Cat. No.04CH37509)*, April 2004, pp. 345–348.

[40] T. Gorski, J. Le Caillec, L. Lecornu, A. Kawalec, W. Czarnecki, J. Pietrasinski, and B. Solaiman, "Space-time adaptive processing analysis for the moving target on the sea surface indication purpose," in *2006 International Conference on Microwaves, Radar Wireless Communications*, May 2006, pp. 199–202.

[41] M. Farshchian, "Target extraction and imaging of maritime targets in the sea clutter spectrum using sparse separation," *IEEE Geoscience and Remote Sensing Letters*, vol. 14, no. 2, pp. 232–236, Feb 2017.

[42] V. Gracheva and J. Ender, "Multichannel analysis and suppression of sea clutter for airborne microwave radar systems," *IEEE Transactions on Geoscience and Remote Sensing*, vol. 54, no. 4, pp. 2385–2399, April 2016.

[43] Jingyao Liu, Huadong Meng, and Xiqin Wang, "Radar sea clutter suppression and target detection with alpha-beta-gamma filter," in *2008 9th International Conference on Signal Processing*, Oct 2008, pp. 2376–2379.

[44] S. P. Sira, D. Cochran, A. Papandreou-Suppappola, D. Morrell, W. Moran, and S. Howard, "A subspace-based approach to sea clutter suppression for improved target detection," in *2006 Fortieth Asilomar Conference on Signals, Systems and Computers*, Oct 2006, pp. 752–756.

[45] T. Yang, L. Yang, G. Bi, and Y. Wang, "A novel wide area multiple azimuth beam isar imaging system," *IEEE Access*, vol. 7, pp. 65 277–65 287, 2019.

[46] Y. Yuhan and Q. Taifan, "Fast multi-channel digital stretching technique in shore-based isar for ship imaging," in *2011 First International Conference on Instrumentation, Measurement, Computer, Communication and Control*, Oct 2011, pp. 796–799.

[47] Emadi, K. Sadeghi, A. Jafargholi, and F. Marvasti, "Co channel interference cancellation by the use of iterative digital beam forming method," *Progress In Electromagnetic Research, PIER*, vol. 87, pp. 89–103, 01 2008.

[48] Jie Chen, Huaitie Xiao, Hongqi Fan, and Zhiyong Song, "Isar imaging of multiple moving targets using signals separation," in *Proceedings 2013 International Conference on Mechatronic Sciences, Electric Engineering and Computer (MEC)*, Dec 2013, pp. 1156–1159.